NUCLEAR-RECOIL/ELECTRON-RECOIL DISCRIMINATION IN CRYOGENIC SILICON DETECTORS FOR USE IN DARK MATTER SEARCHES

A DISSERTATION
SUBMITTED TO THE DEPARTMENT OF PHYSICS
AND THE COMMITTEE ON GRADUATE STUDIES
OF STANFORD UNIVERSITY
IN PARTIAL FULFILLMENT OF THE REQUIREMENTS
FOR THE DEGREE OF
DOCTOR OF PHILOSOPHY

Michael James Penn
September 1995

I certify that I have read this dissertation and that in my opinion it is fully adequate, in scope and quality, as a dissertation for the degree of Doctor of Philosophy.

Blas Cabrera (Principal Advisor)

I certify that I have read this dissertation and that in my opinion it is fully adequate, in scope and quality, as a dissertation for the degree of Doctor of Philosophy.

Robert B. Laughlin

I certify that I have read this dissertation and that in my opinion it is fully adequate, in scope and quality, as a dissertation for the degree of Doctor of Philosophy.

Douglas D. Osheroff

Approved for the University Committee on Graduate Studies:

For Elizabeth

ABSTRACT

There is abundant evidence which suggests that the majority (> 90%) of the mass in the universe is in a dark, unknown form. Weakly Interacting Massive Particles (WIMPs) are a particularly well motivated class of candidate dark matter particles. It may be possible to detect WIMPs via elastic scattering from the nuclei in laboratory detectors. Such an experiment would provide a very low signal event rate (~ 1 nuclear-recoil event kg^{-1} day^{-1}) and one of the main challenges of the experiment would be the reduction of contaminating background events (mostly electron-recoils) due to radioactivity in the laboratory or the detector itself. In addition to sophisticated shielding schemes, the detector will need an active background rejection capability. One attractive background rejection technique is the discrimination of nuclear-recoils (signal) from electron-recoils (backgrounds) based on the simultaneous measurement of both phonons and ionization. A nuclear-recoil event partitions more of its energy into phonons, and less into ionization, than does an equal energy electron-recoil event.

We have configured a double-sided Silicon Crystal Acoustic Detector (SiCAD) for simultaneous measurement of both phonons and ionization. This detector operates at ~ 370 mK and consists of a Ti Transition Edge Sensor (TES), which is the phonon detector, on one side, and a similar pattern of metal, acting as an electrode for the ionization measurement, on the other side of a 300 μm thick high-purity, monocrystalline Si wafer. The phonon sensor is also position sensitive: it measures the distance between the event location and the detecting surface and can be used to reject background events occurring near the surface. In addition, a coupling between the phonon sensor and the ionization sensor allows the determination of event position in one dimension in the plane of the detecting surface. We present the results of experiments which demonstrate the discrimination capability and position sensitivity of the detector for energy depositions above ~ 3 keV.

The physics of charge measurement, necessary for the background rejection technique, in silicon at low temperature ($T < 0.5$ K) and low applied electric field ($E = 0.1$ - 100 V/cm) has been examined in a variety of high purity, p-type silicon samples with room temperature resistivity in the range 2 - 40 kΩ-cm. The samples varied in thickness from 300 μm to nearly 5 mm. Charge loss at low electric field due to trapping during charge drift is present but the data suggest that another charge-loss mechanism is also important. We present results which indicate that a significant fraction of the total charge loss (compared to full collection) occurs in the initial charge cloud near the event location. A simple model of charge trapping both in the initial cloud and

along the electric field induced drift to the electrodes is developed and satisfactory comparison to the data is found. In addition, measurements of the lateral size, transverse to the applied electric field, of the initial electron-hole cloud indicate large transverse diffusion lengths. At the lowest fields a lateral diameter on the order of 1 mm is found in samples ~ 5 mm thick.

ACKNOWLEDGMENTS

It is with great pleasure that I thank my advisor, Blas Cabrera, for all his tutelage and advice over the last five years. Blas always brought a calm and understanding attitude to the laboratory and his off-the-cuff remarks about five-minute-old data always turned out to be right on the mark. I feel very fortunate to have had an advisor whose temperament so closely fits my own. I like nothing better than to work an interesting technical problem out for myself (I find this is the best way to learn). Blas was never heavy-handed about when the results would be ready and he was always willing to stop what he was doing if I needed help or had some specific questions. Most importantly, Blas always gave me the impression that he was here to help his students and not that we (the students) were here to further his research.

I would like to thank Adrian Lee for the apprenticeship in cryogenics and electronics that I did under his supervision my first couple of years in graduate school. Adrian's attitude toward teaching me how to run the ^{3}He cryostat was very effective. He just had me get my hands dirty and do it, even when he had his own delicate experiments mounted! This method was very effective at getting me involved in the group's activities and at giving me the research momentum to jump into my own projects. Adrian also taught me the workings of the phonon sensors and just about everything I know about discrete FET amplifiers. Adrian is, in addition, a valued friend and scientific collaborator.

I would also like to thank Brian Dougherty for his contributions to the charge collection experiments over the last couple of years. Even though we did not always agree on interpretation of data or on how to proceed in the next experiment, Brian's point of view provided useful insight into many of the details of the experiments.

Betty Young taught me the hands on processing of the transition edge sensors, for which I am grateful. She worked several marathon processing sessions with me at CIS to fabricate some TES's on special substrates. In addition, her help was essential in the fabrication of the small (1 cm x 1 cm) samples made for the charge collection experiments. I would also like to thank Betty for her helpful and heartening assistance during my (ongoing) job search.

Kent Irwin and Barron Chugg were entertaining, if not eccentric, labmates. I would like to thank them for all the lighthearted and bizarre humor they brought to lab every day. I have great friendship and respect for them both.

I would like to thank Sae Woo Nam for his amazing ability to solve problems with the GPIB instruments and with computers in general. There have been many times when he saved me from much frustration when the computers weren't working properly.

I would like especially to thank Roland Clarke for his assistance in the lab over the last several months. Roland's timely arrival in our group allowed me to pass on some works-in-progress and actually graduate! Thanks Roland.

The machine shop staff also deserve much thanks. Wolfgang Jung, Karlheinz Merkle, and especially Dan Semides (a fellow frequent visitor to the Fresno-Clovis area) would always interrupt their work to help a novice machinist, either with sound practical advice or by loaning some special machine tools.

I am also grateful for the friendly disposition of everyone on the Physics Department main office staff. In particular, Marcia Keating was always available for help and she always took a personal interest in the students' progress. Also, Lore Jung would always help me, with a smile, figure out how to work the mail meter (I actually needed help several times!).

The positron-trap group at UCSD deserves thanks for giving me my first taste of experimental physics. Cliff Surko, Tom Murphy, Mark Tinkle, and Gene Jerzewski took me under their collective wing and showed me the excitement of laboratory research.

I would also like to thank all the members of my family for their encouragement and love. George and Jan Penn, and Lisbeth Penn and Joe Guzaitis always gave me the feeling that what I was doing was just perfect, for the simple reason that it was what I wanted to do. They always encouraged me in my interests and I never felt steered in any particular direction. Brian Penn was always willing to provide me with a political opinion which, to say the least, was a bit to the right of my own. Nevertheless, Brian has an open mind and would often wish to think through an issue again after our discussion. Mary Kate and Kenny Legaspi (my Fresno-Clovis connection) were always an attentive audience when I would attempt to explain to non-scientists what my research was all about (this is not as easy as it sounds!). Gary, Joan, and Jon Brammer provided many a much needed break from work. Vacation time spent in Los Angeles was always loads of fun. Highlights included exchange of goods and services, rest and relaxation, extraordinarily good food, and good company. I simply cannot imagine more wonderful in-laws.

Finally I would like to thank my beautiful wife Elizabeth, who is my true love, and to whom this thesis is dedicated. She has provided me with more love, encouragement, and comfort than I presume to deserve. She has also helped me determine what is really important to me in life, for which I am eternally grateful.

TABLE OF CONTENTS

LIST OF FIGURES

LIST OF TABLES

CHAPTER 1: INTRODUCTION

There has been growing interest in recent years in the development and use of particle detectors which operate at very low temperatures. This field has its own conference (International Workshop on Low Temperature Detectors) which meets biannually and over the last ten years it has grown to about two hundred participants from around the world [1]. The field is divided into several sub-groups depending on the specific application of the detectors being developed. Our group at Stanford, and a few others, have as a goal the detection and identification of dark matter and, as a future offshoot, the development of neutrino physics experiments. This application requires a fairly large (~ kg) detector which can handle very low, background-limited event rates. In addition, good energy resolution and low threshold are needed. Other applications are high-resolution x-ray and beta spectroscopy which require small detectors where imaging and the possibility of high event rates is desirable. Both types of detectors are being developed for low temperature operation because the excitations which are used to detect the particle interactions are intrinsically very low energy (phonons in semiconductors and superconductors, quasi-particles in superconductors). It is the low energy of these excitations which, in part, can give these detectors such good energy resolution.

In the dark matter search or neutrino physics experiment that we envision low event rates are expected (~ 1 event kg^{-1} day^{-1}). This expected event rate is well below the best achieved raw background rates. It is therefore critical, in addition to using sophisticated shielding schemes to reduce the raw background rate, for the detector itself to be able to distinguish background events (mostly electron-recoils) from the events of interest (nuclear-recoils). One technique for achieving this background rejection is the simultaneous measurement of both the phonons and the ionization produced by a particle interaction in a cold semiconductor. Electron-recoils can be distinguished from nuclear-recoils because low-energy nuclear-recoils are less ionizing than equal energy electron-recoils. The simultaneous measurement of phonons and ionization can therefore provide the required discrimination on an event by event basis. The demonstration of this technique in a silicon detector with a fast phonon sensor is one of the main subjects of this thesis. Background rejection can be further improved by measuring event location within the detector since background events will occur predominantly near the surfaces of the detector and because ionization collection is typically worse for near surface events.

The phonon sensor is a Ti Transition-Edge Sensor (TES). It senses a particle interaction in the silicon substrate by absorbing, in a thin titanium film on the surface, the prompt, athermal phonons generated in the event. This type of sensor is capable of

measuring event location in one dimension (distance from the surface) in addition to the deposited energy. The ionization sensor operates by drifting the electrons and holes excited by the event through the cold semiconductor crystal in a low electric field ($E < 100$ V/cm). A coupling between these two measurements allows the determination of event location in one dimension parallel to the crystal surface. The detector then measures the nature of the recoil (through the ratio of phonons to ionization), the deposited energy, and the event location in two dimensions.

This thesis will describe the operation of a cryogenic particle detector which is based on a thin-film superconductor on the surface of a high-purity silicon crystal. This detector technology is intended for use in a dark matter search. In particular, we will focus on the nuclear-recoil/electron-recoil discrimination capability which is a crucial aspect of this type of detector. We will first offer a brief summary of the evidence for the existence of dark matter and the detector capability requirements needed to mount a dark matter search. We will then describe the detector technology including the operation of the phonon sensor and the ionization sensor. Next we will demonstrate the nuclear-recoil/electron-recoil discrimination capability. We will then report on some interesting charge-collection and trapping effects which were studied in the course of understanding the physics of the ionization measurement. Finally, some recent developments and future prospects will be discussed.

1.1 Motivation - Evidence for Dark Matter

There is an abundance of observational evidence which implies the existence of dark matter in the universe. In fact, more than 90% of the total mass in the universe may be dark such that it neither emits nor absorbs electromagnetic radiation. The exact nature of this matter is entirely unknown, although certain candidate particles are better motivated than others. An important parameter in discussions of the mass of the universe is the cosmological density $\Omega = \rho/\rho_c$ in units of the critical density. The critical density, $\rho_c \equiv 3H_0^2 / 8\pi G = 1.9 \times 10^{-29} h^2$ g cm^{-3}, is the density of matter required to critically close the universe, where $h \approx 0.5 - 1$ is the current value of the Hubble parameter H_0 in units of 100 km s^{-1} Mpc^{-1} and G is the gravitational constant (1 Mpc = 3.1 x 10^{19} km). (Note that ρ_c has an implicit time dependence because H depends on time.) This means that for $\Omega = 1$ the expansion of the universe will slow and asymptotically halt . For $\Omega > 1$ the universe will eventually recollapse and for $\Omega < 1$ the universe will expand forever. The cosmological density is measured on various length scales by gravitational effects and $\Omega \leq 1$ is found with the largest values of Ω (and large uncertainty) coming from

measurements on the greatest length scales (~ 30 Mpc) [2]. On the smallest length scales where observations have been made (~ 0.1 Mpc) the internal dynamics of galaxies suggest $\Omega \approx 0.1$.

There is theoretical prejudice for $\Omega = 1$ exactly. Since $\Omega = 1$ is an unstable equilibrium, any small deviation from $\Omega = 1$ will grow exponentially with time. The fact that Ω is known to be within an order of magnitude of 1 now suggests strongly that $\Omega = 1$ exactly. In other words, Ω must have been extraordinarily close to 1 in the very early universe for it to be still within an order of magnitude of 1 now, i.e. billions of years later (this requires, at the time of nucleosynthesis, $1 - \Omega \approx 10^{-15}$). Thus it is plausible to postulate $\Omega = 1$. Also, the theory of cosmic inflation [3] in the early universe predicts $\Omega = 1$.

One of the main problems confronting cosmology today is the fact that the amount of luminous mass in the universe (stars, galaxies, clusters of galaxies) gives $\Omega_{luminous} << 1$. If we believe $\Omega = 1$ then dark matter dominates the mass of the universe. The search for dark matter is then not just dotting the i in a theory of cosmology; dark matter is in this sense the most fundamental aspect of the universe!

The most powerful argument for the existence of dark matter comes from the study of the internal dynamics of spiral galaxies. The strength of this argument is enhanced by the fact that it does not rely on detailed cosmology at all. If one believes the standard gravitational theory then the mass of a spiral galaxy must be dominated by a dark, roughly spherical halo in which the galaxy is embedded. As a concrete example, consider the rotation curve of a spiral galaxy like our own Milky Way. The rotation curve measures the velocity of test particles in the galactic disk by the Doppler shift of stellar emission lines (typically hydrogen, ionized oxygen, and ionized sulfur) and 21 cm radiation from neutral hydrogen (hyperfine transition) as a function of distance from the core of the galaxy [4] (see figure 1.1.1). Measurements of this type have been performed on more than a hundred spiral galaxies and they all share the same qualitative features [5]. In general, the velocity increases rapidly with radial distance away from the core (much like a rigid body) and then a region of constant (or even rising) velocity with distance is seen. The flat region of the rotation curve is in contrast to the predicted curve based on the observed luminosity of the galaxy. The luminosity of the galaxy is found to decrease roughly exponentially with distance from the core. The stellar mass-luminosity relation [6] allows a calculation of the amount of mass in the galaxy which is shining in stars (luminous mass). A comparison between the measured rotation curve ($\Omega_{halo} \geq 0.03 - 0.1$) and the curve based on the luminous mass only ($\Omega_{luminous} \leq 0.01$) [7] indicates that a large fraction of the total mass in the galaxy does not emit or absorb

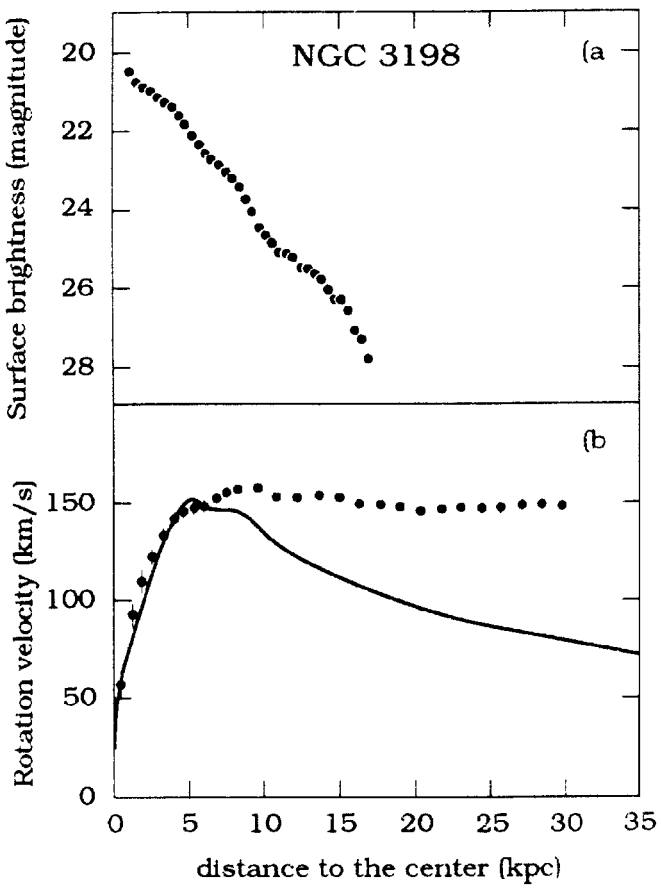

Figure 1.1.1 Distributions of surface brightness and rotation velocity as functions of the distance to the center of NGC 3198. Measurements are given by the data points. The solid curve in (b) is the predicted rotation velocity distribution assuming the mass distribution is the same as the bightness distribution. From [Ref. 4].

electromagnetic radiation. This is strong evidence for the existence of a cloud of dark matter surrounding galaxies.

For a flat rotation curve, the total mass determining the motion of test particles must increase with distance from the core according to $M(r) \propto r$ where M(r) is the total amount of mass contained within radius r. This follows from the simple balance, assuming a spherical mass distribution, between centrifugal force and gravitational force for a test particle of mass m at radial distance r:

$$\frac{mv^2(r)}{r} = \frac{GmM(r)}{r^2}. \qquad (1.1)$$

For v(r) constant (flat rotation curve) we must have a mass density which depends on r beyond the core as $\rho(r) \propto r^{-2}$, since $M(r) \propto \int_0^r \rho(r')r'^2 dr'$, while the luminous mass density falls much more rapidly with r. Flat rotation curves have been measured in some galaxies out to three times the luminous radius using the 21 cm radiation. In a few galaxies, the velocity of satellite rings of gas which are orthogonal to the plane of the galaxy indicates that the dark matter halo is distributed roughly spherically [2].

Thus, without invoking any cosmological arguments at all, we see that dark matter is necessary to explain the high rotational velocities found outside the core of spiral galaxies. The strong implication is that galaxies are surrounded by a spherical halo of non-luminous matter.

1.2 Dark Matter Candidates

1.2.1 Baryonic dark matter

There are two general classes of dark matter candidate. The first class is called baryonic dark matter. In this class the dark matter is thought to be normal matter (neutrons, protons, etc.) which is in a state that does not emit light. Examples are Jupiter size objects (not massive enough to ignite nuclear reactions), interstellar dust or gas, and black holes. The plausibility of these candidates suffers, however, due to the limits imposed on Ω_B, the density of baryonic matter, by big-bang nucleosynthesis calculations [8,9] which predict the abundance of the light elements ^{4}He, ^{3}He, ^{2}H, and ^{7}Li. In addition, dust and gas can be immediately eliminated as candidates since they would be conspicuous by scattering and absorbing light.

The standard big-bang model pictures the early universe as a very hot ($T \geq 10^{10}$ K) and very dense gas of particles (neutrons, protons, electrons, neutrinos, photons, and other particles) in thermal equilibrium and calculates the time evolution of this gas using the Hubble expansion and the physics of known nuclear reactions. The temperature is initially high enough that the weak reactions governing the interconversion of neutrons and protons are in equilibrium. As the universe expands and cools, the weak reactions fall out of equilibrium. The neutrinos (and any other weakly interacting particles) then thermally decouple from the rest of the matter and they expand freely. After further expansion and cooling, photodisintegration of light nuclei is no longer efficient and

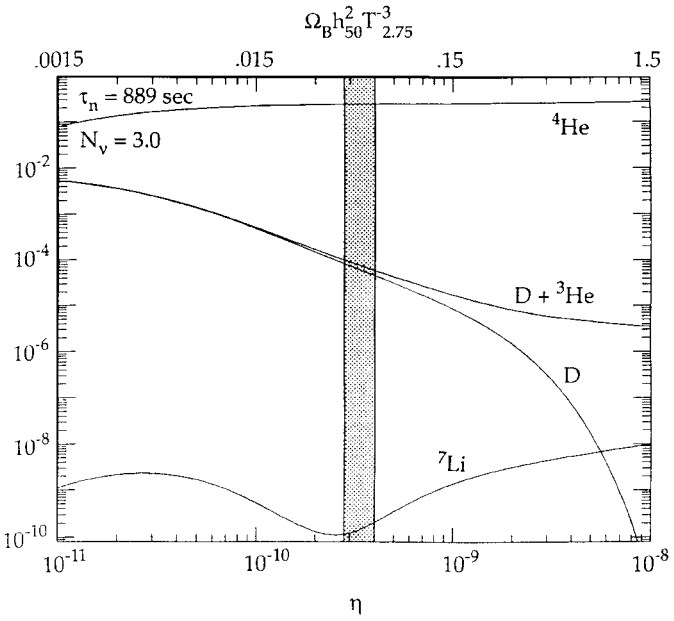

Figure 1.2.1 Predicted abundances (by number) of D, D + ^{3}He, and ^{7}Li, and the ^{4}He mass fraction as a function of a single baryon density parameter. The vertical band shows the range which is consistent with observations. The implications for Ω_B are discussed in the text. From [Ref. 9].

reactions such as $p + n \leftrightarrow {}^2H + \gamma$ swing to the right and the light nuclei are rapidly formed.

Figure 1.2.1 shows the calculated abundances as a function of the parameter $\Omega_B h_{50}^2 T_{2.75}^{-3}$ where Ω_B is the density of baryonic matter, h_{50} is the Hubble parameter in units of 50 km s^{-1} Mpc^{-1} (h_{50} = 1 corresponds to h = 0.5), and $T_{2.75}$ is the temperature of the cosmic microwave background radiation in units of 2.75 K. Also shown is the range of $\Omega_B h_{50}^2 T_{2.75}^{-3}$ which is in agreement with current measurements of these abundances. The measurements of the abundances and the uncertainties in h_{50} and $T_{2.75}$ restrict the likely values of Ω_B to the range $0.01 \le \Omega_B \le 0.1$ [9]. Obviously, if Ω = 1 then the majority of the dark matter must be non-baryonic. In other words, baryonic matter (Jupiters and black holes) fails to "close" the universe by at least a factor of 10.

An additional strength of the standard big-bang model is the fact that other proposed methods of producing the light elements (spallation from heavy elements, supernova shock waves, and other galactic sources) cannot match the measured ^{4}He abundance without overproducing all the other light elements [8].

Finally, recent searches for Massive Compact Halo Objects (MACHOs), which are thought to be Jupiter type objects, surrounding our galaxy have had some success [10]. These experiments observe the time-symmetric brightening and dimming of stars in the Large Magellanic Cloud due to the gravitational lensing of these stars by nearby, massive, and dark objects. However, the results of these observations have determined that less than 20% of the dark matter halo in our own galaxy could be made up of MACHOs. Thus, there is a need for non-baryonic dark matter.

1.2.2 Non-baryonic dark matter

The possible candidates for non-baryonic dark matter range from particles which are known to exist, such as neutrinos ($m_\upsilon \leq 30$ eV), to completely hypothetical particles. A list of possible candidates and their expected properties is given in Ref. [2]. One particularly well motivated class of candidates is the weakly interacting massive particle (WIMP) with mass in the range m_{DM} = 1-100 GeV (We will adopt the shorthand notation of specifying particle mass in units of energy; the factor $1/c^2$ is implied).

There are three reasons why the WIMP is a good dark matter candidate. First, particles in this mass range would help explain structure formation in the universe. Neutrinos, unless they were very massive (several GeV, which is not well motivated by particle physics), would tend to wipe out rather than enhance the density fluctuations in the early universe which led to the formation of galaxies and other large-scale objects. WIMPs would be a more natural seed for galaxy formation [7]. (The existence of a so called fourth generation neutrino, which could be quite massive, has recently been ruled out by experiments at SLAC and CERN which confirmed the limit of only three neutrino generations.)

Second, WIMP dark matter can fairly naturally provide $\Omega = 1$. If we assume that there is no WIMP-antiWIMP asymmetry, then the amount of WIMP dark matter today is set by the annihilation cross section, $< \sigma v >_A^F$, for WIMPs at the time of weak scale interaction decoupling (also called freezeout) . Ref. [2] gives

$$< \sigma v >_A^F \approx 1 \times 10^{-26} (4\Omega_{DM} h^2)^{-1} cm^3 s^{-1}. \qquad (1.2)$$

For σ given by weak strength interactions ($\sigma \approx 10^{-38}$ cm^2) and $m_{DM} \approx$ few GeV, eqn. 1.2 implies $\Omega_{DM} \approx 1$.

Third, supersymmetry theories predict the existence of a weakly-interacting lightest superpartner with a mass in the few GeV to tens of GeV range. So from several

points of view the WIMP is a good dark matter candidate. It should be emphasized, however, that only a range of mass and interaction strengths is postulated. The detectors being developed at Stanford are designed with the WIMP in mind as the most likely dark matter candidate.

1.3 Interaction of WIMP Dark Matter with Ordinary Matter

The evidence strongly suggests that dark matter is in the form of weakly interacting elementary particles (WIMPs). The possibility exists to detect these particles directly in the laboratory through their interactions with ordinary matter. In order to examine the feasibility of this scheme we must estimate the local flux of WIMPs and the relevant cross sections for WIMP interactions with ordinary matter of which, obviously, detectors are made. By far the most likely WIMP-detector interaction (largest cross section) is elastic scattering from a target nucleus. This is due to the target mass dependence in the cross section

$$\sigma_{DM,N} \propto \frac{m_{DM}^2 m_N{}^2}{(m_{DM} + m_N)^2}. \tag{1.3}$$

Thus, the probability of elastic scattering from, say, a target electron is smaller by nearly the ratio $(m_e / m_N)^2$ (assuming the WIMP coupling to leptons and quarks is the same). In addition to the dependence shown in eqn. 1.3, $\sigma_{DM,N}$ is also expected to scale as the square of the number of nucleons in the target nucleus. This scaling is predicted for low-momentum transfer events because the nucleus can recoil coherently. Following Ref. [11], which assumes a simple model of the dark matter halo density to estimate the local flux, we can write the event rate for elastic WIMP-nucleus scattering as

$$R \approx 4.3 \frac{X_N}{m_{DM} m_N} \sigma_{DM,N} \rho < v > \ kg^{-1} day^{-1} \tag{1.4}$$

where X_N is the fraction of the detector mass which is active as a target, ρ is the local WIMP density in units of 0.3 GeV/cm^3, <v> is the mean speed of WIMPs in the detector's reference frame in units of 300 km/s, and $\sigma_{DM,N}$ is in units of 10^{-38} cm^2. For a target of germanium or silicon, low but detectable rates on the order of 1 event kg^{-1} day^{-1} is implied by eqn. 1.4. Ref. [2] compares the expected event rates for different target nuclei as a function of m_{DM}.

In addition to the raw event rate expected, we must also estimate what size signal might be seen in a detector due to a nucleus recoiling from an incoming WIMP. In the non-relativistic limit, the nucleus recoils with energy

$$\Delta E = \frac{m_N m_{DM}^{\ 2}}{(m_N + m_{DM})^2} v^2 (1 - \cos\theta) \qquad (1.5)$$

where v is the speed of the incoming WIMP and θ is the center-of-mass scattering angle. Given the expected range of m_{DM}, Eqn. 1.5 indicates that the maximum deposited energy ($\theta = \pi$) is on the order of 10 keV. For example, if $m_{DM} \approx 10$ GeV, $m_N \approx 30$ GeV (silicon nucleus), and $< v > \approx 300$ km/s, then $< \Delta E_{max} > \approx 3.8$ keV. WIMPs with higher than the mean velocity can deposit more energy than this but the number of particles in the high velocity tail of the distribution diminishes rapidly with increasing velocity. We can therefore establish that the events of interest in a WIMP dark matter search are low energy (~ 10 keV) nuclear-recoils.

Another very important consideration in the design of a low event rate experiment is an understanding of likely backgrounds. The detector will be exposed to a variety of background radioactivity, all of which can reduce the detector's sensitivity: cosmic rays (hadrons and muons), cosmic ray induced neutrons and γ–rays, and natural radioactivity in the laboratory and the detector itself (x–rays, β–particles, and α–particles). The detector can be shielded from cosmic ray hadrons and natural radioactivity occurring outside the detector assembly by operation underground and by containment within a sufficiently thick lead shield. Cosmic ray muons can be actively vetoed using a system of plastic scintillators which surround the detector. Muon induced neutrons can be moderated until they are too in low energy to contaminate the experiment.

Even under these conditions, however, Ref. [11] points out that the natural radioactivity in the detector itself and its support equipment (best achieved raw background rate of ~ 0.1 event/kg/keV/day at 10 keV) will contaminate the sought for dark matter events. However, these background events (x–rays, β–particles, and α–particles) are all electron-recoils (except for rare Rutherford back-scattering events where an α–particle scatters from a nucleus). There are two ways that the effects of these background events can be minimized. First, the radiation is not very penetrating. X–rays, β–particles, and α–particles are all absorbed in a solid-state detector close to the surface. If a fiducial volume can be defined to exclude the regions near the surface then these events can be ignored. Thus it is desirable for the detector to be capable of measuring the position of an event within the detector. Second, the events of interest

(WIMP scatterings) are nuclear-recoils. A detector which can discriminate nuclear-recoils from electron-recoils can give a very useful background suppression. Using such a discrimination technique, it is estimated that a background rate of ~ 0.2 event/kg/day can be achieved [12].

1.4 Detector Capability Requirements for a Dark Matter Search

As a summary of the above discussion we will describe the capabilities required of a detector intended to search for weakly-interacting, particulate dark matter. Each of the capabilities has been achieved by our group at Stanford or is nearing demonstration. Further detail on the current state of each of these capabilities is given in chapter 6.

First, because the expected dark matter signals are low-energy (~ 10 keV) nuclear-recoils we need a detector with a low threshold for deposited energy and reasonably good energy resolution. As a rule of thumb, both a threshold and resolution $\leq$ 1 keV is required. The thesis work of K.D. Irwin [13] has demonstrated a phonon sensor which has no intrinsic threshold and achieved a resolution of ~ 400 eV FWHM at 6 keV (see section 6.1).

Second, to achieve a useful event rate it is necessary to instrument ~ 1 kg of detector mass. The Stanford group [14] is designing a detector made of 6 1 cm thick wafers (4 silicon, 2 germanium) for a total mass of ~ 900 g (see section 6.3).

Third, to reduce the background rate below the WIMP scattering event rate a sophisticated shielding scheme is needed. In addition, detector position sensitivity and nuclear-recoil/electron-recoil discrimination ability is required. Fast phonon sensors which allow sub-μs timing is very important for a muon veto system and for event position imaging. A shield with veto has been constructed and characterized (see section 6.4). The fast response phonon sensor with position sensitivity is a common aspect of all the detectors the Stanford group has developed. The discrimination technique has been demonstrated [15] and a detailed discussion of it is the subject of most of this thesis.

CHAPTER 2: EXPERIMENTAL APPARATUS

2.1 Pumped ^{3}He Cryostat

All of the experiments reported here were conducted with the detector mounted in a custom-built pumped ^{3}He refrigerator. This cryostat was designed by B. Neuhauser [16] and was completed and wired by A.T. Lee (see figure 2.1.1). The final stage of cooling is achieved in a single-shot mode with an activated charcoal "sorb" pump which is located within the cryostat. The entire base of the cryostat is located within a 1.6 K pumped ^{4}He bath in a 2" neck glass dewar. The ^{3}He pot at the bottom of the cryostat contains ~ 3 cm^3 of liquid ^{3}He which is pumped by the charcoal. At room temperature, the ^{3}He gas expands into a cylindrical reservoir located at the top of the cryostat. The gas pressure in the reservoir is 60 psi at room temperature. The cryostat is small and easy to handle: a typical cooldown from room temperature to base temperature takes only ~ 5 hours.

The base temperature with no heat load is 260 mK. Cryogenic pre-amplifiers are mounted in the space above the ^{3}He pot and are thermally heat sunk to the pumped ^{4}He bath. The amplifiers are connected to the detector at the bottom of the cryostat through thin manganin wires stretched on short sapphire rods to minimize stray capacitance. The ^{4}He bath can handle a total power dissipation of ~ 30 mW from the amplifiers without disturbing the base temperature of the cryostat. There is sufficient wiring in place for eight detector channels including dc bias wires (thin manganin) and signal wires (stainless steel coaxial cables). There is room in the amplifier space for four separate pre-amplifier boards (two amplifier channels per board). Below the ^{3}He pot is an experimental space where the detector is mounted. There is enough room in the current setup to operate detectors as large as 1 cm x 1 cm x 5 mm.

To initiate a cooldown to base temperature from 1.6 K the sorb is heated to ~ few tens K to drive off the adsorbed ^{3}He. This ^{3}He recondenses on the walls of the sorb line and drips into the pot at the bottom. The sorb heater is turned off and the charcoal quickly cools down and begins pumping the ^{3}He again. Base temperature is reached in less than one hour. After ~ 8 hours of data taking, the ^{3}He will run out and another regeneration cycle is necessary.

Temperature regulation of the ^{3}He stage is achieved through feedback between a thermometer (germanium resistance thermometer) and a heater (metal film resistor). The thermometer is monitored by a Linear Research LR400 ac resistance bridge and an LR130 temperature controller compares the GRT reading to a setpoint and feeds back to

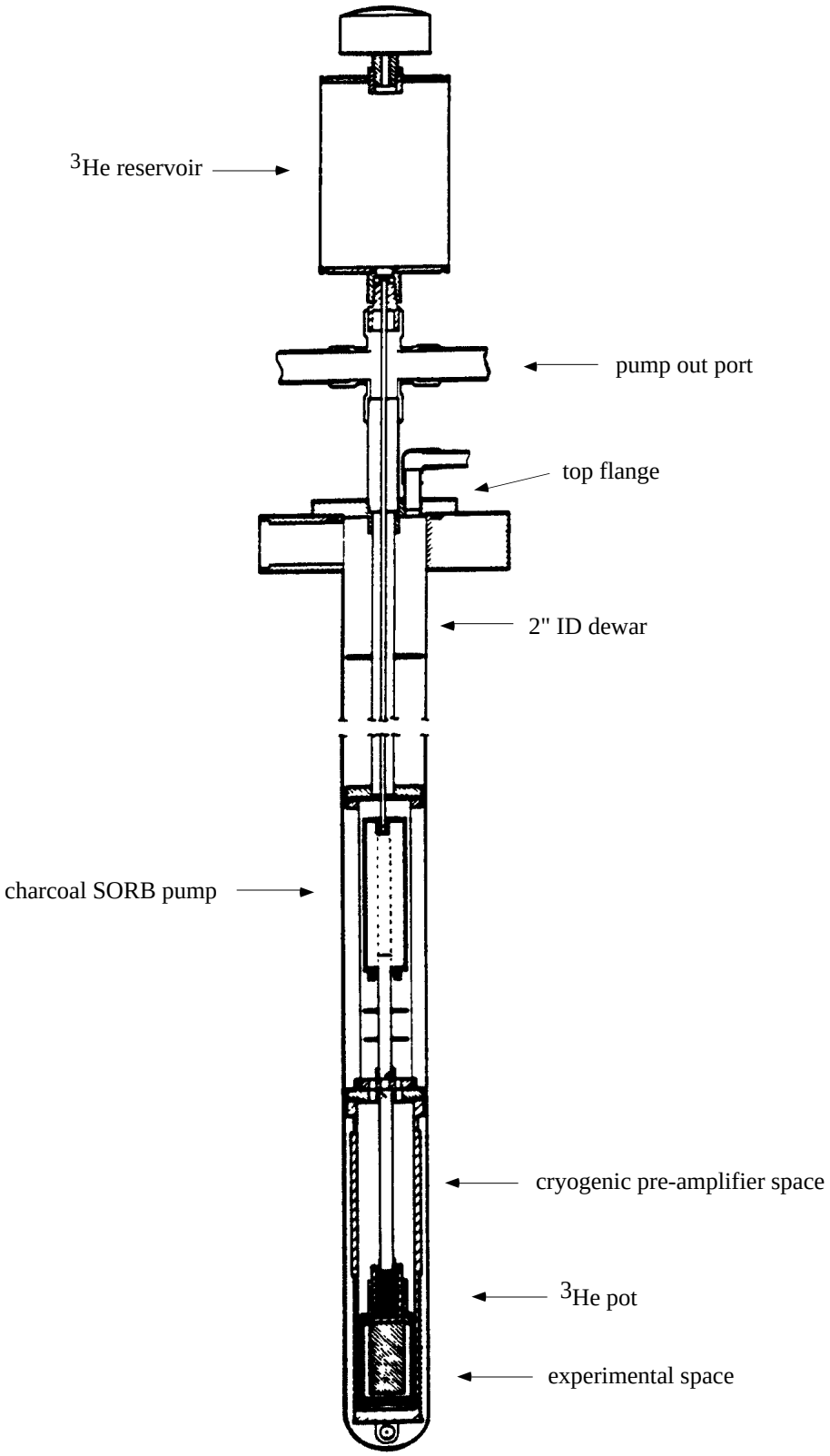

Figure 2.1.1 Diagram of pumped ^{3}He cryostat.

the heater. The cryostat delivers ~ 50 μW of cooling power at 370 mK. This temperature can be maintained for ~ 8 hours after which a ~ 1 hour sorb regeneration is needed.

2.2 Cryogenic Pre-amplifiers

When particle detectors are operated at very low temperature one is faced with the difficulty of reading out the signals. The detectors themselves can have a fast response (< μs) and it is obviously undesirable to have the signal bandwidth seriously limited by the readout electronics. The main problem is the amplifier input capacitance. The signal risetime will be RC limited (where R is the input signal impedance and C is the total capacitance at the input of the amplifier) so C must be kept as small as possible. If the amplifiers are located outside the cryostat then the input of the amplifier consists of long wires with ~ 200 pF capacitance to ground. For typical signal impedance R ~ 10 kΩ we have a risetime of ~ 2 μs. This situation has the disadvantage that for a signal pulse which is only ~ 5 μs long the amplifier response will truncate the peak pulse height. It is also desirable to see the fast leading edge of the detector pulse for timing purposes.

These difficulties were surmounted by A.T. Lee [17,18] who designed and built an amplifier which has very low input capacitance (~ 15 pF). This design has the first gain stage located in the cryostat close to the detector, thus minimizing the stray capacitance due to the wires connecting the detector to the amplifier. It is necessary to use an active device (FET) which will operate at low temperature. In this section we will briefly describe this amplifier, which is based on a GaAs MESFET, and a variant based on a Si JFET. All of the experimental work described in this thesis used the GaAs MESFET amplifier design to instrument the various detectors.

2.2.1 GaAs MESFET amplifier

The amplifier design is given in figure 2.2.1. The active device is the Sony 3SK164 GaAs dual-gate MESFET. The GaAs FET operates at low temperature because the activation energy of the majority dopant is very small (0.003 eV). Four MESFETs Q1-Q4 are connected in parallel (acting like one large FET with transconductance ~ 15 mS) to minimize the voltage noise at the input. The FETs themselves are heat sunk to the 1.6 K stage of the cryostat but their dc power dissipation heats them to ~ 30 K. Under typical operating conditions each amplifier dissipates ~ 2 mW into the 1.6 K pumped ^{4}He bath.

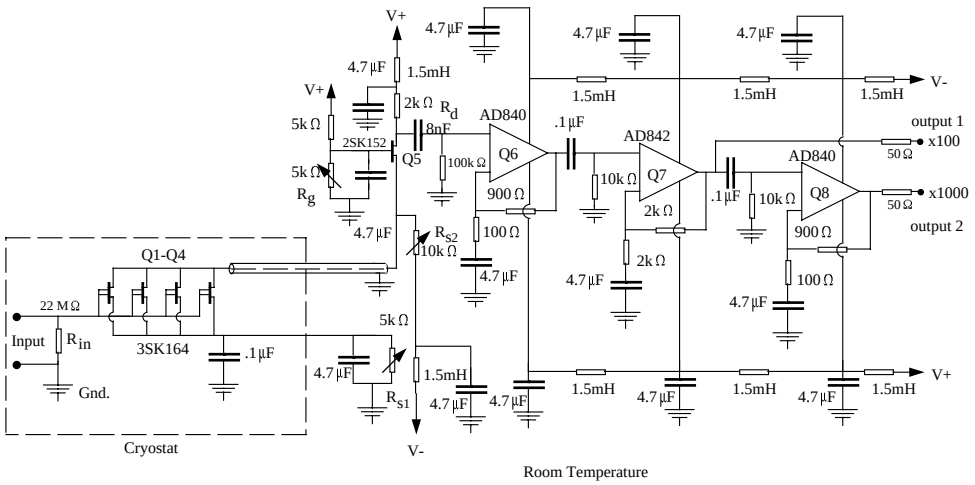

Figure 2.2.1 Schematic diagram of the high bandwidth pre-amplifier. The front-end (Q1-Q4) is mounted in the cryostat at the 1.6 K stage. Q6-Q8 are Analog Devices operational amplifiers. The voltage supplies are ± 15 V. From [Ref. 17].

The front end of the amplifier consists of two FETs in the cascode connection. The bottom half of the cascode is the cryogenic GaAs FET (Q1-Q4) and the upper half is a Si JFET which is at room temperature (Q5). This arrangement eliminates the "Miller effect" which causes a loss of gain at high frequencies in a FET amplifier through feedback across the parasitic drain-to-gate capacitance. Also, the line to room temperature is fairly well matched (in a transmission line sense) at the source of the room temperature JFET.

The cascode section is followed by non-inverting op-amp gain stages (Q6-Q8). These op-amp stages provide two outputs for total gains of ~ 100 and ~ 1000 (the exact value depends on the dc bias of the cryogenic FETs). The output impedance of these stages is explicitly set to 50 Ω in order to efficiently drive 50 Ω coaxial cable (the intrinsic output impedance of the op-amps is < 1 Ω). The middle gain stage has a gain of 2 to compensate for the voltage-divider effect of properly terminating a 50 Ω cable. The pre-amplifier can be connected to, depending on the experiment, a timing amplifier, a spectroscopy amplifier, a multi-channel analyzer, or a digitizing oscilloscope. The overall bandwidth of the design is ~ 10 MHz.

The noise of a cascode amplifier is dominated by the bottom FET as long as the transconductance of the bottom FET is large enough, ~ 15 mS [19]. This condition is

satisfied and a white noise level of ≈ 1 nV/√Hz (referred to the input) is found for typical dc bias conditions of the lower FET ($V_{DS} \approx 1$ V, $I_D \approx 2$ mA). GaAs FETs are known to have considerable low-frequency noise below a few hundred kHz. The devices used here are the best known with a 1/f knee (the frequency where white noise and 1/f noise contribute equally) at ~ 50 kHz when operated at very low temperature. Unfortunately, these devices are no longer available from Sony and their replacement has much worse 1/f noise.

The total capacitance at the input of the amplifier is ~ 15 pF. This includes ~ 8 pF which is intrinsic to the FETs and their packaging (1 pF per gate), and ~ 7 pF which is the stray capacitance from the connecting wires and connectors. The RC limit on the risetime is ~ 150 ns. This risetime is fast enough not to distort the peak pulse height and to allow the measurement of timing differences between detector channels.

There is ac coupling between the gain stages of the amplifier. Each stage is coupled to the next through a CR network like that shown in figure 2.2.2(a). Such a network is a high-pass filter with a -3 dB point at $2\pi f_c = 1/RC$. If the signal pulse contains frequencies near or below f_c then this high-pass filter will distort the pulse, usually resulting in an undershoot of the pulse's tail. Figure 2.2.2(b) and (c) give a qualitative example of this type of shaping. For understanding the detector's response we wish to recover the shape of the input pulse $v_i(t)$ from the output pulse $v_o(t)$ before any pulse analysis is done so that the results are not affected by the amplifier's low-frequency response. For the amplifiers used here $f_c \sim 1$ kHz.

It is possible to undo the shaping of the filters in software after the digitized pulse data have been taken. The input and output voltages result from a current I(t) flowing in the network. Referring to figure 2.2.2 we can write

$$v_i(t) = \frac{1}{C}\int_0^t I(t')dt' + I(t)R \qquad (2.1)$$

and

$$v_o(t) = I(t)R. \qquad (2.2)$$

We can combine these two equations to obtain a simple relation between $v_i(t)$ and $v_o(t)$:

$$v_i(t) = \frac{1}{RC}\int_0^t I(t')Rdt' + v_o(t). \qquad (2.3)$$

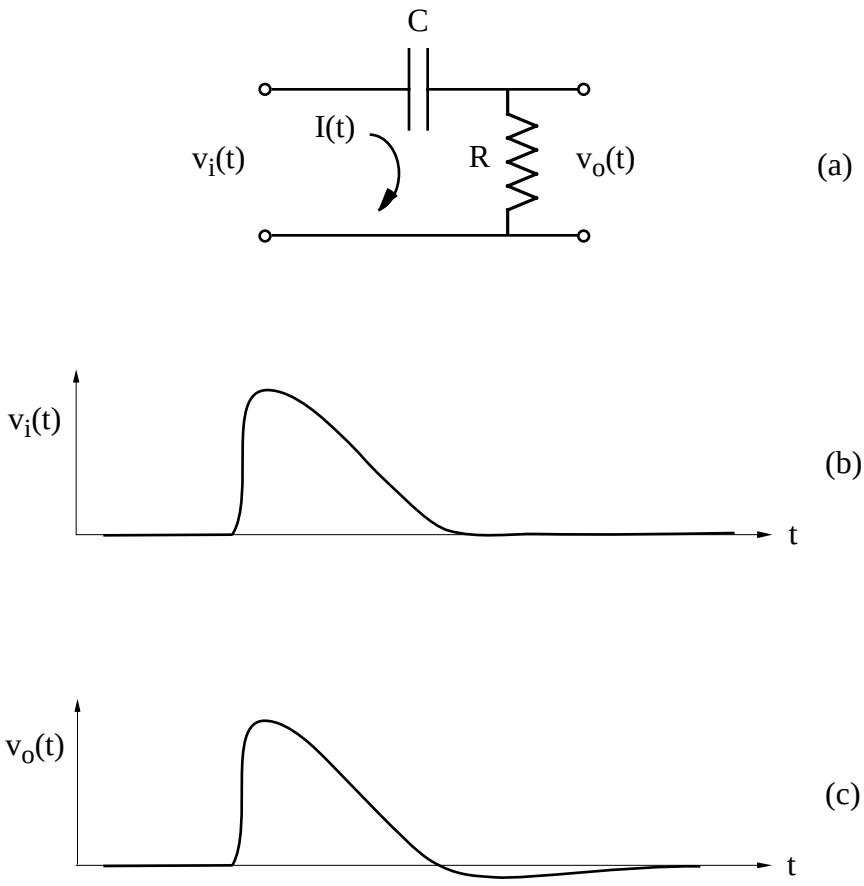

Figure 2.2.2 (a) Schematic diagram of ac filtering between gain stages in the amplifier. (b) Sample pulse shape for input to filter network. (c) The output of the network showing the undershoot due to the high-pass filter.

But, using eqn. 2.2 we can rewrite this as

$$v_i(t) = \frac{1}{RC}\int_0^t v_o(t')dt' + v_o(t). \qquad (2.4)$$

Since $v_o(t)$ is what is measured and stored, it is simple to numerically perform the integral in eqn. 2.4 once R and C are known. Thus all the analysis programs used to analyze the pulse trace data first execute this un-shaping routine to restore the correct pulse shape.

2.2.2 Si JFET amplifier

Due to the unavailability of the 3SK164 GaAs MESFET, and in order to improve the amplifier's noise performance below 50 kHz, we have begun using a Si JFET (replacing Q1-Q4 with a single JFET) as the first stage of the cascode connection. The Si JFET typically has much better low-frequency noise with a white noise level of $\sim 1\ nV/\sqrt{Hz}$ down to $f < 100$ Hz. The single JFET used is the Sony 2SK152. This FET has low input capacitance (8 pF) and high transconductance (~ 30 mS).

A Si JFET, however, must be kept at an elevated temperature relative to the stage of the cryostat where it is mounted. This is because the dopant impurities are frozen out at a temperature below ~ 100 K (the activation energy is ≈ 0.03 eV, about 10 times that of GaAs). In fact, the best noise performance for Si FETs is found at T ~ 120 K where carrier scattering from thermal phonons is reduced compared to room temperature but the impurities are not yet frozen out. The FET is mounted on a holder which itself is heat sunk to 1.6 K. The FET is thermally isolated from the holder with thin (1 mil) manganin wire such that its dc power dissipation (few mW) heats it up to ~ 120 K. A resistor is mounted with the FET which acts as a heater to initially warm up the FET so that it will begin operation.

This arrangement with the Si JFET improves the noise performance of the amplifier substantially. For example, the energy resolution in the ionization pulse height spectra described in section 3.4 was improved by a factor of two. Unfortunately, the fairly large thermal impedance between the FET and the 1.6 K stage of the cryostat leads to very long time constants for thermal equilibrium so there can be slow drifts in gain. If the dc bias of the FET is altered it can take more than two hours for it to reach a stable temperature.

This behavior can be avoided if a more complicated amplifier design is implemented where feedback is used to set the gain regardless of the FET transconductance (as long as it is not too small) but then the bandwidth is necessarily smaller. This type of amplifier has recently been installed by R. Clarke and the energy resolution of the ionization spectra were further improved (see section 6.2).

2.3 Data Acquisition and Analysis

The data were taken using either of two data acquisition sub-systems. Most of the experiments rely on detailed pulse processing techniques to measure several pulse

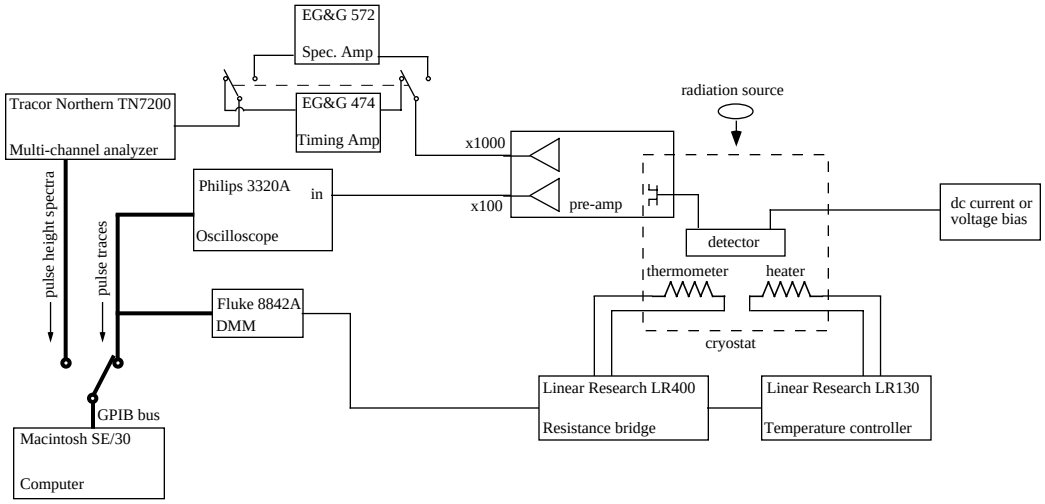

Figure 2.3.1 Diagram of data acquisition system. Data are taken through the oscilloscope to store complete traces. The multi-channel analyzer is used to save pulse height spectra only. The cryostat temperature is regulated by the LR400/LR130 combination and is monitored by the DMM.

parameters such as height, length, falltime, etc. For these experiments the data were taken and stored as digitized time traces from a Philips 3320A 2-channel digitizing oscilloscope. Computer control of the instrumentation was accomplished through the IEEE488 GPIB bus and Microsoft QuickBASIC. The data transfer rate was ~ 0.5 traces per second. Samples of the programs used for data acquisition and off-line analysis are given in the appendix. A schematic diagram of the data acquisition system is shown in figure 2.3.1. The computer was also interfaced to a digital multimeter in order to monitor the resistance of the cryostat germanium resistance thermometer (GRT). A current or voltage bias is applied to the detector depending on the type of experiment being done.

In some experiments it was not necessary to store the entire pulse trace. Pulse height spectra are useful in many cases and the data can be taken much more quickly because a typical pulse height sensitive multi-channel analyzer can handle high event rates. In this case, a Tracor Northern TN7200 multi-channel analyzer was used. This analyzer could handle data rates as high as 1000 events per second. Also, all the events could be captured for making event rate calculations. Here the output of the pre-amplifier was sent into either a fast timing-filter amplifier (for phonon experiments) or a spectroscopy amplifier (for ionization experiments) as shown in figure 2.3.1. The different post-amplifiers are used because of the different pulse time constants involved in the two types of experiment. In these experiments we were able to study a variety of

detector responses through their influence on the pulse height spectra. For storing pulse height spectra it was necessary to have only the TN7200 connected to the GPIB bus. The TN7200 is not a "true" GPIB instrument and it will place data on the data bus even when it is not being addressed. It thus interferes with data transfer from other instruments. This problem can be avoided by taking the TN7200 off the GPIB bus when it is not being used.

Off-line data analysis was done using QuickBASIC. Routines for finding pulse height and length, fitting to expected shapes, plotting spectra, and so on are listed in the appendix.

CHAPTER 3: DETECTOR TECHNOLOGIES

In this chapter we will discuss why it is desirable to develop low-temperature detectors. We will briefly survey the types of detectors being made and their intended applications. Next, since the Stanford detectors are based on semiconductor crystals, we will review the semiconductor physics relevant at low temperature. Finally, we will focus on the Stanford detector technology with detailed discussions on the phonon and charge measurements. These sections will lead naturally into the next chapter where the two types of measurement are combined to identify a particle interaction as either an electron-recoil event or a nuclear-recoil event.

3.1 Cryogenic Detectors - Brief Survey

It is convenient to view a detector system as a quiescent state which is disturbed by the production of excitations by the particle being detected. These excitations are collected and counted in some way and then the detector returns to its quiescent state to await the next event. A particle of energy E spends some average amount of energy $\bar{\varepsilon}$ creating each excitation. Thus the mean number of excitations produced is $\bar{n} = E / \bar{\varepsilon}$. Assuming the collection efficiency to be high and the measurement electronics noise to be small, the resolution of a detector is limited by the statistics of the excitation production, $\Delta n_{rms} / \bar{n} \propto \sqrt{F / \bar{n}}$ where F is the Fano factor which accounts for correlations in the production of excitations (F ~ 0.2 for silicon ionization detectors). It is therefore desirable, given these assumptions, to have $\bar{n}$ as large as possible. A detector which is based on an intrinsically lower $\bar{\varepsilon}$ can therefore have a larger $\bar{n}$. This is one technique currently being used in cryogenic detectors to achieve higher resolutions. For example, a detector based on phonon excitations in a crystal can have $\bar{n}$ orders of magnitude larger than a detector based on ionization production in a gas or semiconductor, with the corresponding improvement in resolution. Table 3.1 lists some typical detector excitations and their corresponding $\bar{\varepsilon}$. Because $\bar{\varepsilon}$ is so low for phonon and quasi-particle excitations, detectors based on them must be operated at very low temperatures so that these excitations are not spontaneously generated. Thus, the gain in energy resolution comes at the price of low temperature operation.

There are several detector applications where very good energy resolution and low threshold are desirable [1]. Dark matter searches or neutrino physics experiments expect to see a very low rate of low-energy nuclear-recoil events. Thus a low threshold and reasonably good energy resolution is crucial. This application is being pursued by

Type of Excitation	Mean excitation energy, ε
scintillation	~ 100 eV
ionization in a gas	~ 10 eV
electron-hole pair in semiconductor	~ 3 eV
phonon in a crystal	~ 10^{-3} eV
quasi-particle in superconductor	≤ 10^{-3} eV

Table 3.1 Typical excitations used in particle detectors and the mean energy spent to create them. Detectors based on phonons or quasi-particles must be operated at very low temperature because ε is so small.

several groups and the detectors are based on either superconducting thin-film transition edge sensors (Stanford), superconducting phase transition thermometers (Munich), or NTD-Ge thermistors (Berkeley). As discussed in chapter 1, in order to achieve useful event rates these detectors must be rather large, with ~ 1 kg of instrumented mass.

Low-energy x-ray spectroscopy (materials analysis, x-ray astronomy) would benefit greatly from detectors with enhanced resolution. X-ray astronomers would like to resolve the many low-energy x-ray lines which are smoothed into a broad peak in conventional, slow, and relatively poor-resolution detectors [20]. Several cryogenic detectors for low-energy x-rays are being developed: tunnel-junction based detectors (Lawrence Livermore National Laboratory and Munich), and semiconductor microcalorimeters (NASA Goddard). It also appears feasible to achieve resolutions good enough to see chemical shifts in x-ray lines from atoms in materials analysis using the electro-thermal feedback (ETF) technique briefly described in chapter 6 [21, 22]. Such a detector could measure material properties including molecular structure. The ETF type detector using tungsten thin films is also being pursued for possible use as an infra-red bolometer for measuring the cosmic microwave background radiation.

There is also interest in using cryogenic detectors for low-energy beta spectroscopy. High-resolution beta end point experiments can provide better limits on the mass of the electron-neutrino [23].

3.2 Semiconductors at Low Temperature

3.2.1 Phonon physics

A particle interaction event in a semiconductor like silicon excites both electron–hole pairs and phonons. At first, the phonon system is composed of high energy (near Debye energy, ~ 60 meV) optical phonons: for electron-recoils these are created as the electrons and holes cool to their respective band edges; some of the phonons are primeval for nuclear-recoils. These high-energy phonons rapidly decay (lifetime < 10^{-10} sec, [24]) to the three acoustic phonon modes (longitudinal (L), fast transverse (FT), and slow transverse (ST)). The detector is operated at sufficiently low temperature such that the evolution of the phonon system is not influenced by thermal phonons. At these temperatures, the evolution of the phonon system is dominated by the physics of elastic (isotope) scattering, where phonon mode conversion can occur, and inelastic (anharmonic decay) scattering, where one phonon decays into two phonons of lower frequency. The time constants for these types of scattering are strongly dependent on phonon frequency and, for Si in the dispersionless limit, are given by

$$\tau_I = 0.4097\left(\frac{\nu_0}{\nu}\right)^4 \text{ μs} \tag{3.1}$$

for isotope scattering [25] and

$$\tau_{AD} = \tau_{AD}^0\left(\frac{\nu_0}{\nu}\right)^5 \tag{3.2}$$

for anharmonic decay where ν_0 = 1 Thz and τ_{AD}^0 depends on the phonon mode and is given after averaging over all directions in the crystal as: $\tau_{AD}^0 \approx$ 6 μs for L, $\tau_{AD}^0 \approx$ 25 μs for FT, $\tau_{AD}^0 \sim$ infinity for ST [26]. The ST phonons are able to down convert by first mode converting by isotope scattering to L or FT followed by the anharmonic decay of the L or FT phonon. The isotope scattering time constant is always shorter than the anharmonic decay time constant for all phonon frequencies. As the phonons decay to lower frequency (few THz) the isotope scattering time constant lengthens and the phonons can propagate significant distances without further scattering (mean free paths increase). After about 1 μs (independent of the details of the initial phonon frequency spectrum) the phonon system consists of a roughly symmetrical distribution in frequency-space centered near 1 THz of acoustic phonons propagating mostly diffusively away from the

interaction location. It is these phonons (energy ~ 4 meV) which will be sensed by a detector on the surface of the silicon crystal. Since the detector described in section 3.3 is sensitive only to the first wavefront of phonons, the subsequent reflection from surfaces and accompanying down-conversion is not directly relevant.

A small fraction of the phonon energy has low enough frequency that the mean free path is as large as the crystal. Such phonons are termed "ballistic" because they can propagate from the event location to the crystal surface without scattering. Due to the anisotropy of the elastic constants in silicon these phonons are "focused" along certain symmetry axes of the crystal [27]. The focusing of the phonon energy has a detectable effect on the response of the phonon detector described in section 3.3 [28].

3.2.2 Equilibrium conditions in a semiconductor crystal at low temperature

The equilibrium state of a semiconductor is given by the condition of charge neutrality. In all the experiments described in this thesis p-type silicon was used and we will refer in what follows to that type of crystal. For p-type silicon we must have $N_A > N_D$ where N_A is the density of acceptor impurities and N_D is the density of compensating donor impurities. At low temperature ($T < 1$ K), there will be no thermally generated free carriers since $E_A - E_V$, $E_C - E_D$ (~ 30 meV) >> k_BT (< 100 μeV) and we can visualize the state of the crystal easily in two different ways. (There is certainly not any free charge excited across the gap since $E_{gap} = E_C - E_V =$ 1.1 eV is even larger than the energy required to ionize a dopant impurity.) Figure 3.2.1 shows a schematic band diagram for p-type silicon and defines the various symbols.

The first, qualitative way to determine the state of the crystal relies on the observation that it is energetically favorable for an electron which is located on a donor impurity to transfer to a nearby acceptor. This electron then loses nearly the full gap worth of energy and both impurities are left ionized; in other words, the donor is empty (D^+) and the acceptor is occupied (A^-). This process occurs for all the donor impurities and we then must have all the donors ionized. Since each donor is transferring its electron to an acceptor, there will be an equal number of ionized acceptors. At low temperature, these ionized impurities form dipole pairs between a donor and the nearest acceptor. Thus, the equilibrium state of the crystal consists of N_D ionized donors and N_D ionized acceptors per cm^3 and essentially no free charge carriers. This is a useful qualitative description of the crystal.

A somewhat more detailed understanding of the state of the crystal can be seen by considering the behavior of the fermi level in the semiconductor as a function of

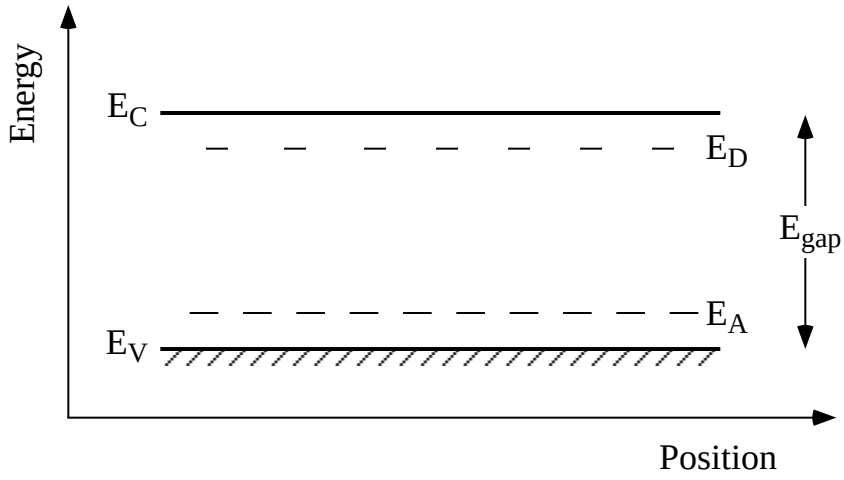

Figure 3.2.1 Schematic band diagram for silicon. E_C and E_V are the energies of the conduction band and the valence band respectively. E_A and E_D give the energies of the acceptor and donor impurities. $E_{gap} = E_C - E_V =$ 1.1 eV and the energy required to ionize an acceptor (donor) is $E_A - E_V$ ($E_C - E_D$) $\approx$ 30 meV.

temperature. The fermi level, ε_f, tells us the probability of occupation at temperature T for an electron state with energy ε through the fermi-dirac function

$$f_e(\varepsilon) = (e^{(\varepsilon-\varepsilon_f)/k_BT} + 1)^{-1} \qquad (3.3)$$

where k_B is the Boltzmann constant. The occupation probability for holes is given by $f_h(\varepsilon) = 1 - f_e(\varepsilon)$. At high temperature the fermi level is near the middle of the gap and the physics is dominated by carriers excited across the gap (intrinsic behavior). The transition from $f \approx 1$ to $f \approx 0$ is broad due to the high temperature. Figure 3.2.2(a) illustrates this situation. As the temperature is lowered, excitation across the gap is no longer possible and the fermi level moves toward the level of the majority dopant. For a p-type crystal at a temperature where thermal ionization of acceptors is still likely we must have $f_e(\varepsilon)$ both sharpened due to the lower temperature and shifted down in energy (lower ε_f). (In order to maintain some free hole excitation from the acceptor level we must lower ε_f as $f_e(\varepsilon)$ sharpens.) This situation is shown in figure 3.2.2(b). Finally, at very low temperature, we have ε_f near the acceptor level and $f_e(\varepsilon)$ is very sharp. Here

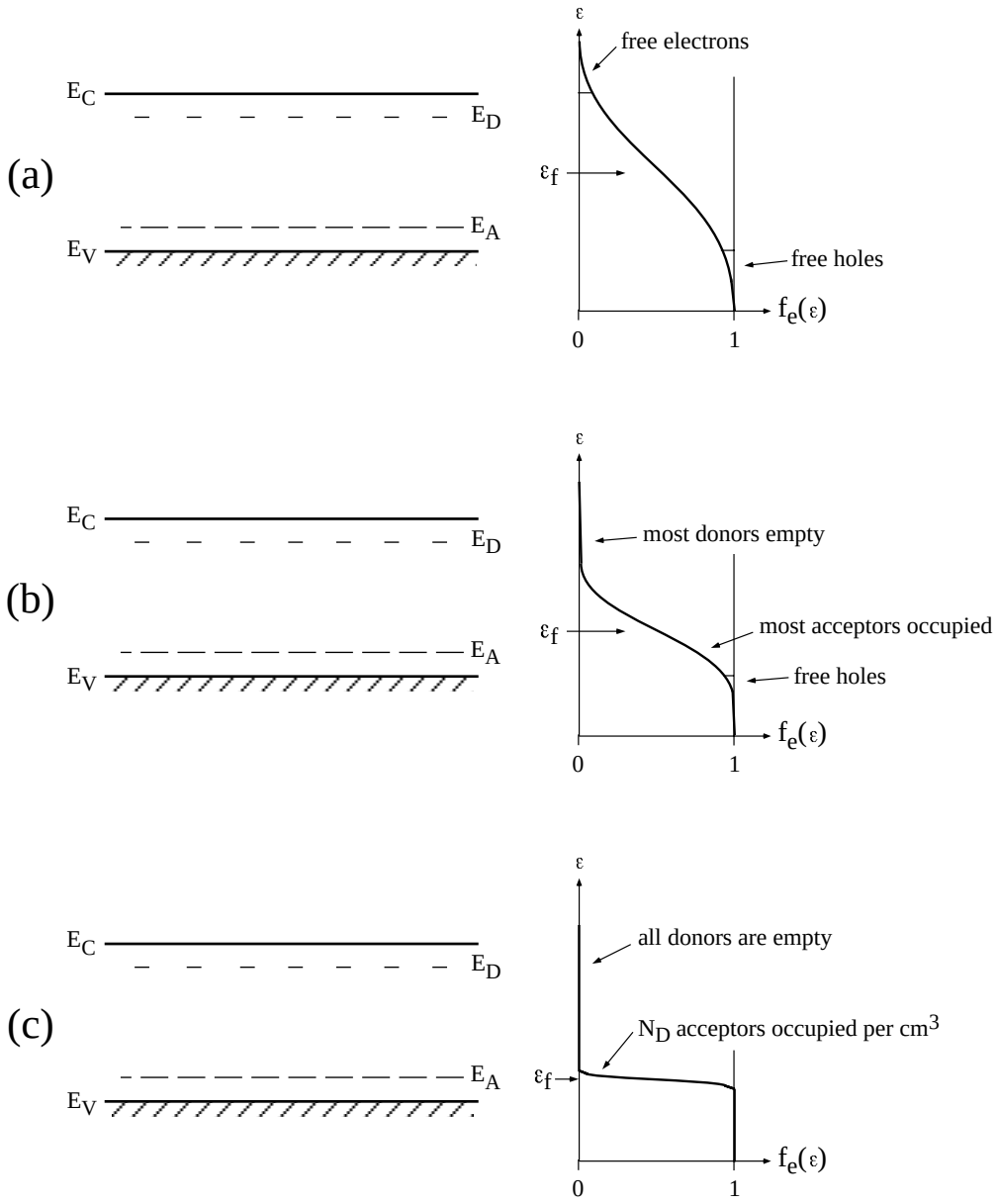

Figure 3.2.2 Band diagram and occupation function $f_e(\varepsilon)$ for different temperatures: (a) T is so large that intrinsic behavior is found, ε_f is located in the middle of the gap and roughly equal numbers of free electrons and holes are present; (b) T is lower, but high enough to excite the majority dopant, ε_f approaches E_A and extrinsic, p-type behavior is seen with more free holes than free electrons; (c) T is quite low (T < 1 K) and there are no free carriers, ε_f is just slightly below E_A.

there is no free carrier excitation at all. The position of ε_f and the sharpness of $f_e(\varepsilon)$ imply that all the donors are ionized (empty) as we deduced above ($f_e(\varepsilon)$ is zero for energies near the donor level). Since there must be as many ionized acceptors as donors (charge neutrality in equilibrium) ε_f will be just marginally different from E_A-E_V (it will be slightly lower) in order to account for the ionized acceptors. Figure 3.2.2(c) describes this condition.

Thus we see that in the thermal equilibrium state of the p-type semiconductor at very low temperature all compensating donors are ionized (empty) as are an equal number of acceptors (occupied). The majority of acceptors, N_A - N_D per cm^3, remain neutral. Of course, the crystal is electrically neutral overall. This picture of the crystal at low temperature will be modified in section 3.2.4 where a very long lived metastable non–thermal equilibrium state is described.

3.2.3 Ti - Si contacts

All the detectors studied here consist of thin Ti films deposited on silicon substrates. These films serve either as a sensor for phonon signals due to particle interactions or as an electrode for applying a voltage bias through the cold silicon. Since we will be concerned later with some charge transport properties of silicon at low temperature we need to specify the electrical properties of the interface.

There is a work function difference between p-type silicon and titanium. In fact, the work function of p-type silicon ($q\Phi_S \approx 4.9$ eV) is greater than that of titanium ($q\Phi_M \approx 4.3$ eV). This means that electrons can have lower energy in the silicon than in the titanium by occupying acceptors near the Ti-Si interface. Such transferred electrons build up a constant density space charge of ionized acceptors near the interface (a Schottky barrier depletion region). A constant density space charge region leads to a quadratic potential profile [29]. As the charge builds up it inhibits further transfer of electrons until the fermi level is equilibrated throughout the interface region. Acceptors which lie below the fermi level are ionized. An equal amount of positive charge builds up in a thin sheet at the surface of the titanium. Figure 3.2.3 shows a cross-section of the interface including the space charge region of ionized acceptors. This space charge region serves to shield the bulk of the crystal from the potential difference at the Ti-Si interface. The space charge region extends into the silicon a distance

$$x_d = \sqrt{2(\Phi_S - \Phi_M)\varepsilon / qN_A} \qquad (3.4)$$

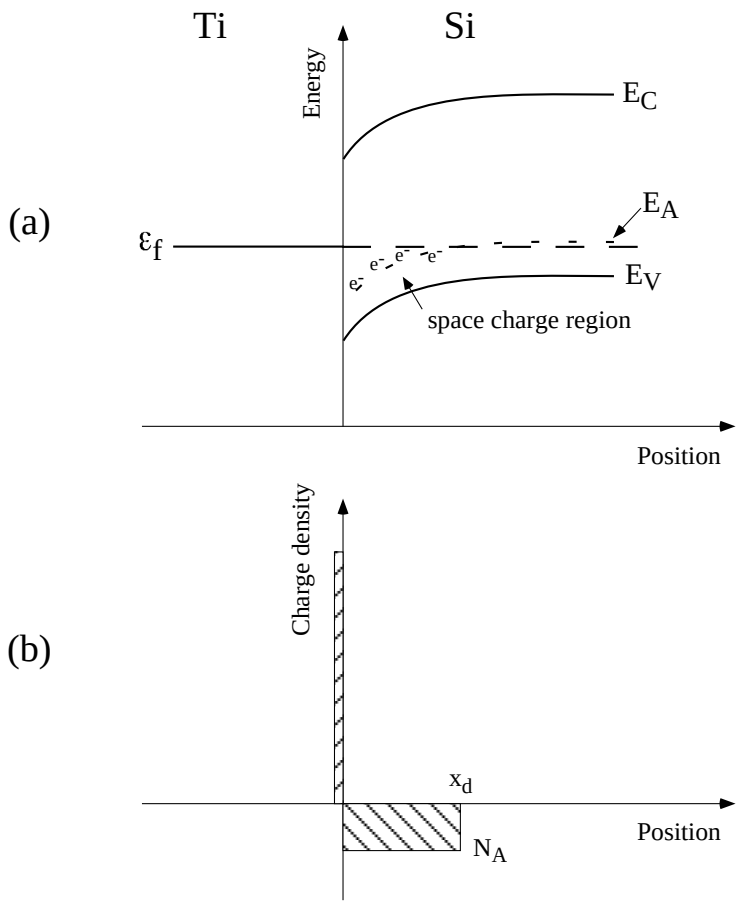

Figure 3.2.3 The Ti-Si Schottky barrier interface. (a) The work function of the silicon is greater than that of the titanium by the barrier height ($q\Phi_S$ - $q\Phi_M \approx 0.6$ eV). (b) A space charge of ionized acceptors exists near the interface and this space charge serves to shield the bulk of the silicon from the interface.

where ε is the dielectric constant of silicon, and q is the charge of the electron [29]. For our fairly high purity samples $N_A \sim 10^{12}$ - 10^{13} cm^{-3} which gives $x_d \sim 10$ - 30 μm.

The Schottky barrier is frozen in as the sample is cooled to T < 1 K. No further depletion effects will occur if an external potential is applied because there is no free charge to add to the space charge region. In other words, the time constant for restoration of equilibrium is very long. The contact region forms a barrier to holes and can freely pass electrons. This type of contact is common to all the films we have used thus far for transition edge detectors. Films of Al, Ti, and W on silicon all form a similar contact

which blocks holes and passes electrons. However, films of Au or Ir form the opposite type contact which forms a (shallower) barrier to electrons.

3.2.4 Mode shifting

It was found that the detectors operate in two distinct modes which differ in the number of ionized impurities which contribute to charge trapping mechanisms. Just after cooldown, the detector is found to operate in Mode 1, which is the thermal equilibrium state described above. Here we have N_D ionized donors and acceptors per cm^3. When particle interactions excite free electron-hole pairs, these carriers can trap on the ionized impurity of opposite sign, leaving the impurity electrically neutral. At our operating temperature these trapped charges are not reemitted. The ionized impurities act as both elastic scattering sites and traps. For $N_D \approx 3 \times 10^{12}$ cm^{-3} (a typical value in the samples used in our experiments), after free charges have cooled to the band edges, the elastic scattering length is ~ 0.3 μm (elastic scattering cross section ~ 10^{-8} cm^2 [30]) and the trapping cross section is ~ 10^{-11} cm^2 [31]. The thermallized free charges are therefore trapped on charged impurities after diffusing an average distance of ~ 5 μm from the location where they thermallized. This trapping is a serious impediment to charge collection at low electric field which is necessary for the background discrimination technique.

As the detector is exposed to ionizing radiation for a prolonged period, the ionized impurities are all gradually neutralized. We no longer have a thermal equilibrium state described by a fermi level. What we have is a long lived metastable state with nearly all donors and acceptors neutral. Scattering and trapping are then dominated by neutral impurity processes for which cross sections are orders of magnitude smaller (~ 10^{-10} cm^2 for elastic scattering [30] and ~ 10^{-13} cm^2 for trapping [32]) and free charges can diffuse through the crystal and reach the surfaces. Since the density of neutral impurities is $N_A \sim 10^{13}$ cm^{-3}, the elastic scattering length is ~ 10 μm and the trapping length is ~ 1 cm. The charges can diffuse ~ 200 μm before trapping. We call this state Mode 2 and it is stable (no reemission of trapped charge) for more than two weeks (our longest run) as long as the detector is kept below T ~ 12 K. Charge loss due to trapping is much reduced and, in general, detector performance is greatly improved.

How both of these modes affect the phonon measurement will be discussed in section 3.3 on the phonon sensor. Similarly, the mode dependence of the ionization measurement, which is inherently more sensitive to charge trapping effects, is discussed

in section 3.4. Also, a more detailed analysis of the charge trapping mechanisms will be given in chapter 5.

3.3 The Ti Transition-Edge Phonon Sensor

3.3.1 Ti Transition-Edge Sensor (TES) fabrication

The Transition-edge sensor (TES) consists of photolithographically patterned thin films of Ti on the surface of a polished silicon substrate. The patterns are 2 μm wide, 400 Å thick lines of titanium which meander back and forth 400 times in a series connection on a 5 μm pitch across the polished crystal surface. The area instrumented per pattern is 2 mm x 4 mm. The TES is operated just below the metal film's superconducting transition temperature (~ 370 mK) and biased with a constant dc current (~ 100 nA). When a particle interaction occurs in the crystal, prompt, athermal phonons subsequently absorbed at the surface drive sections of the Ti line normal, generating a localized resistive region which results in a voltage pulse. Typical TES pulses have rise times of < μsec, while fall times are determined by the rate at which the metal film cools by reemission of phonons back into the Si substrate. Figure 3.3.1 gives a schematic diagram of the detector operation.

Detector fabrication was performed in a class 100 cleanroom at The Center for Integrated Systems (CIS) at Stanford and consists of several steps. The 3" polished silicon wafers are first cleaned using standard CIS chemical baths. First, a thin chemical oxide is grown (5: 1: 1 of H_2O: H_2O_2: H_2SO_4 for 10 min) which is etched off (50: 1 of H_2O: HF for 30 sec) to remove surface contamination which was incorporated into the oxide. This step is sometimes repeated to ensure the cleanliness of the surface. Then a final, clean chemical oxide is grown (5: 1: 1 of H_2O: H_2O_2: HCl for 10 min). After a singe to remove surface moisture of 30 min at 150 ˚C, the wafers are metallized (by Robin King of CIS) in the Gryphon argon ion sputterer with ≈ 400 Å of titanium. The Ti deposition takes only ≈ 100 sec. After the metallization the wafers are coated with photoresist using the MTI spinner and developer (positive resist Shipley #1813). The MTI program COATD is used to spin on a 1.2 μm thick layer of resist. A resist pre-bake is done for 25 min at 90 ˚C followed by the patterning using the Canon 4:1 projection aligner and the MTI developer program PDEV (using developer Shipley MF-319). Then a post-bake is done for 25 min at 110 ˚C. The patterns are etched into the Ti films using a simple wet etch consisting of 5: 1: 1 of H_2O: H_2O_2: NH_4OH with no external heating applied. The etch rate was a convenient ≈ 100 Å per minute. After the etch the

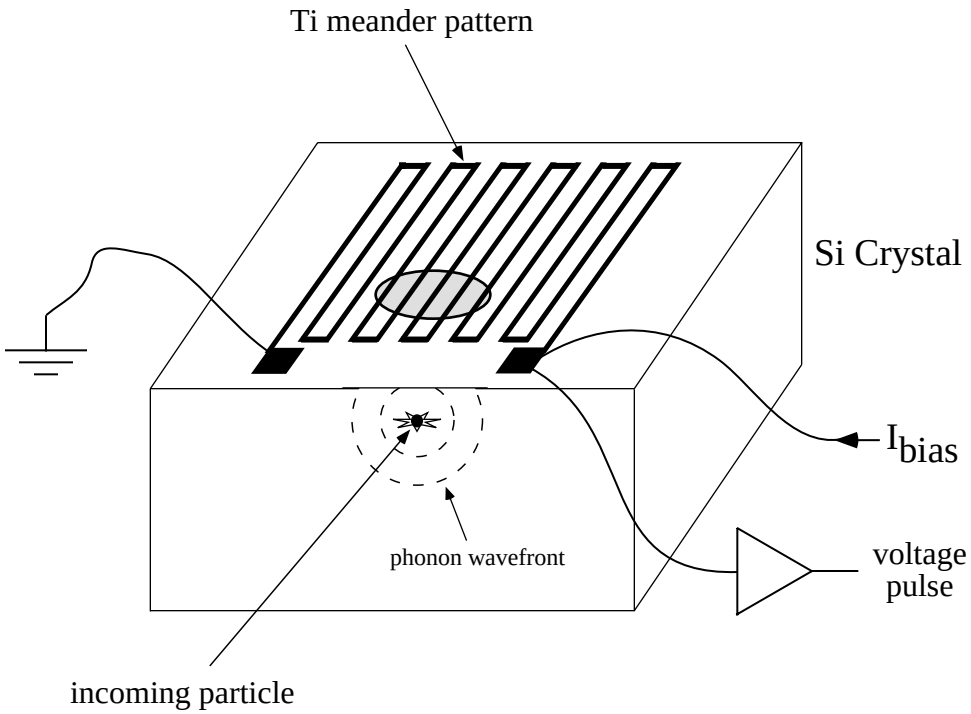

Figure 3.3.1 Schematic diagram of the TES phonon sensor. A particle interaction in the Si substrate excites athermal phonons which propagate to the surface where they drive regions of the Ti film normal. The resistance change is read out as a voltage pulse due to the dc bias current. The shaded area shows the region driven normal.

photoresist is removed in the resist strip baths EMT and PRS1000. The wafers are then diced into individual detectors using the K&S Model 775 wafer saw at CIS while blue sticky tape (0.003" thick, medium-tack, manufactured by Semiconductor Equipment Corp.) is covering the surface to protect the films from the water and silicon grit which is generated during dicing.

Individual detectors are mounted in G-10 holders for operation in the cryostat. Typically, GE 7031 varnish is used to hold the crystal. Electrical connection to the detectors is made using an EMB 1100 ultrasonic wire bonder. This bonder uses a 0.001" Al(2% Si) wire which (with some practice) can bond to Al, Si, Ti, W, Nb, Au, and Cu. The detectors are operated in a pumped ^{3}He refrigerator with a base temperature of 260 mK. This refrigerator delivers ~ 50 μW of cooling power at 370 mK (typical operating temperature). A further ~ 30 mW can be dissipated by the cryogenic pre-amplifiers into the pumped ^{4}He bath without disturbing the base temperature.

3.3.2 Operation of the TES

The TES senses a particle interaction in the silicon substrate via the flux of non-equilibrium phonons (~ 4 meV per phonon) incident on the crystal surface which are created by the recoiling electron or nucleus. The detector is operated at a temperature just below the film's T_c ($T/T_c \approx 0.97$). Portions of the Ti meander pattern which receive more than a threshold amount of phonon energy are warmed up past the film's superconducting transition temperature. The amount of film which is driven normal is read out as a voltage pulse due to the ~ 100 nA dc bias current (see figure 3.3.1). The threshold energy per unit area is given by

$$E_\sigma = \int_{T_{bias}}^{T_C} C_\sigma dT \tag{3.5}$$

where T_{bias} is the operating temperature, T_c is the superconducting transition temperature, and C_σ is the heat capacity per unit area of the Ti film. This expression has been evaluated near T_c for our films using the BCS theory for C_σ [33]:

$$E_\sigma \approx 5N(0)\Delta^2 d(1 - T / T_C) \tag{3.6}$$

where N(0) is the density of states for the normal metal (~ 4×10^{22} cm^{-3} eV^{-1} for Ti), $\Delta \approx 1.7\ k_B T_c$ (~ 50 μeV), and d is the film thickness. For d = 400 Å, eqn 3.6 gives $E_\sigma \approx 0.6$ eV/μm^2 as the nominal sensitivity of the TES.

3.3.3 Details of TES response

The pulse response of the TES can be discussed with reference to Figure 3.3.2 which shows the detector electronics and a sample pulse. The pulse risetime is RC limited at the input of the pre-amplifier to ~ 150 ns (signal resistance ~ 10 kΩ, input capacitance of pre-amp ~ 15 pF). There is further rounding of the front edge of the pulse due to the delayed arrival of some phonon energy and the spreading of the resistive region due to heat flow along the Ti lines. The pulse fall time is determined by the rate at which the film cools by reemission of phonons back into the silicon substrate (~ 2 μs time constant).

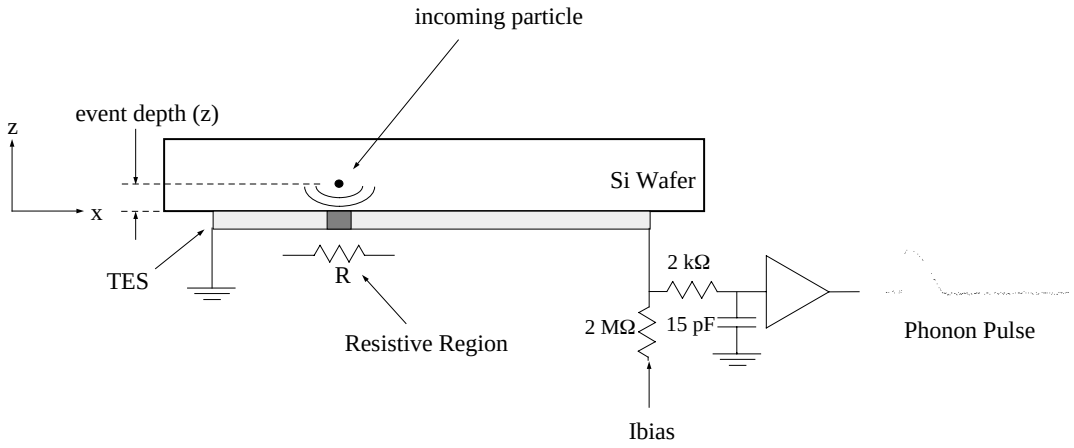

Figure 3.3.2 Diagram of transition-edge sensor (TES) operation showing front end electronics and a sample digitized pulse. Typical phonon pulses are ~ 5 μs long. The phonon pulse length is a monotonic function of event depth (z-direction) and is longer for events which occur closer to the TES film. The vertical scale and size of the resistive region are exaggerated.

In contrast to many conventional particle detectors (such as semiconductor diode detectors), where pulse heights are proportional to the deposited energy and pulse lengths are determined by amplifier electronics, the response of the TES depends on deposited energy and the distance between the interaction location and the crystal surface. For events close to the surface, the energy density of phonons absorbed in the film is greater than for deep events (by inverse square dilution), and hence shallow-event pulses take more time to recover (longer fall time). Phonon pulse length is a monotonic function of event depth and provides a measure of event location in the z-direction shown in figure 3.3.2. It was found empirically that the event depth is approximately proportional to the square of the pulse fall time [34].

Pulse height also depends on event depth, and generally decreases as events occur further from the detecting surface. The pulse height depends on two competing effects. The amount of film driven normal should decrease with larger event depth since the prompt phonon energy is diluted by the inverse square law (think of the phonon density per unit area on the surface of an expanding sphere). On the other hand, the area driven normal also decreases for events very near the surface since in a mostly diffusive process the near surface will absorb a large fraction of the phonon energy before it can expand to a lateral size much larger than the event depth. In other words, the available phonon energy is less efficiently used to heat up the film on the surface since the diffusive process confines the phonon energy. Figure 3.3.3 illustrates this behavior.

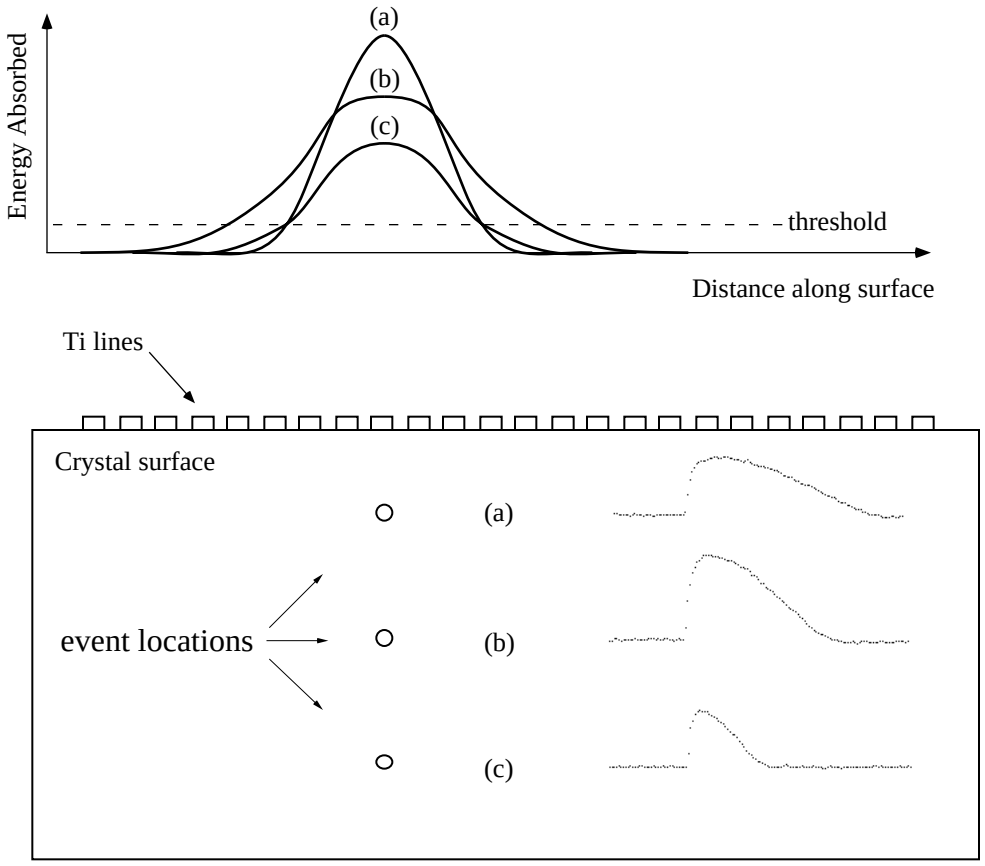

Figure 3.3.3 Depth dependence of the TES response. (a) Event near surface gives peaked curve for energy vs. distance along the surface. The energy is peaked due to the difusive effect discussed in section 3.3.3 and the pulse height is proportional to the area of film which receives more than a threshold amount of energy. The sample pulse has a long falltime. (b) Middle event has more rounded energy vs. distance curve but a larger region of the Ti film is driven past signal threshold. The sample pulse is taller but its length is shorter. (c) Deep event. The sample pulse has about the same height as (a) but its length is much shorter. The pulse height and length continue to decrease monotonically with increasing depth.

The competition between these two effects leads to a double-valuedness in the phonon pulse height. The maximum pulse height for a given energy deposition occurs at a particular depth in the crystal and events either closer to or further from the surface than this event depth give a smaller pulse height. This double-valuedness is explicitly seen

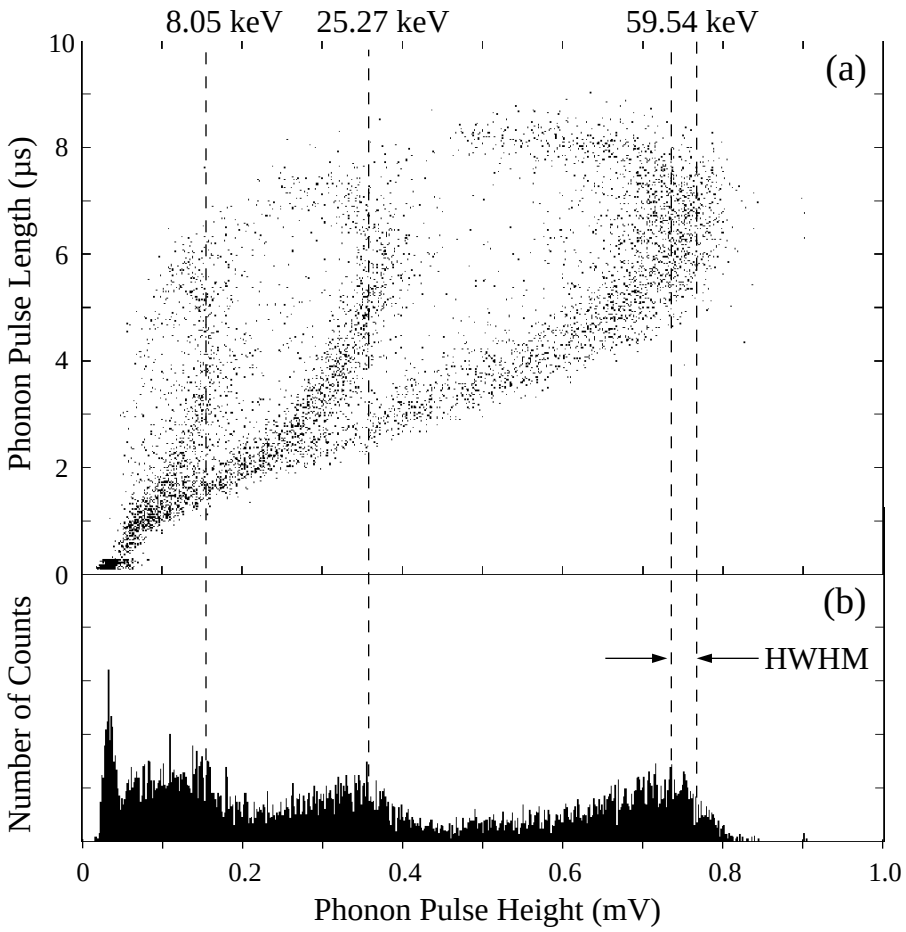

Figure 3.3.4 (a) Phonon pulse height vs. pulse length "ear plot" for energy depositions of 8, 25, and 60 keV. (b) Phonon pulse height spectrum gives HWHM ~ 3 keV at 60 keV.

when a plot is made of phonon pulse length versus phonon pulse height. This type of plot, called an "ear plot," allows the determination of deposited energy and event depth. Figure 3.3.4(a) is an example for energy depositions of 8, 25, and 60 keV (59.54 keV gamma-ray from ^{241}Am and fluorescence x-rays from Sn and Cu). Each energy shows up as a particular curve in the pulse length/pulse height phase space. Thus the phase space can be divided into a set of adjacent curves like those in the figure where each curve is paramatrized by an energy. Along each curve the event depth is read off with large pulse length corresponding to shallow events and small pulse length corresponding to deep events. The shape of the earplot is very well modeled by detailed computer simulations (see figure 3.3.5) which include the relevant phonon physics (anharmonic

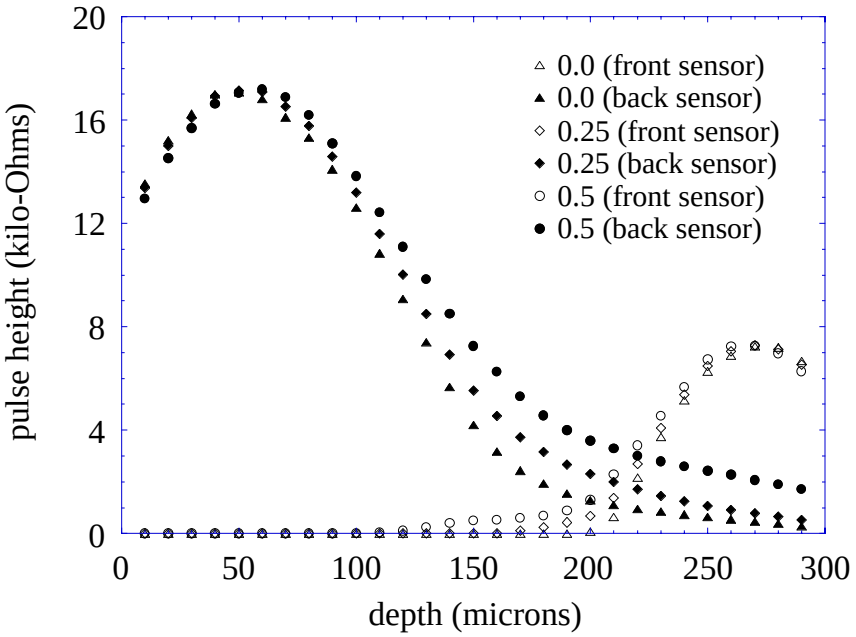

Figure 3.3.5 Computer simulation of TES "ear plot." The detailed phonon physics and sensor response is included in the simulations. The transformation from phonon pulse length to event depth has been done. From Ref. [35].

decay and isotope scattering) which lead to the mostly diffusive propagation of phonons from the event location to the detecting surface [35].

The "ear plot" can be turned into a pulse height spectrum by projecting all the points downward onto the pulse height axis. Such a spectrum is shown in figure 3.3.4(b). The energy resolution is worsened by the projection but the analysis is easier to understand (each energy gives simply a peak and tail in the spectrum and the peaks are spaced nearly proportional to energy [34]).

Under typical operating conditions, the TES is sensitive to 60 keV (25 keV) energy depositions up to ~ 100 μm (70 μm) from the sensor with a resolution in event depth of ~ few μm. The TES has a resolution for deposited phonon energy, which is not electronics limited, of 3 keV HWHM at 60 keV.

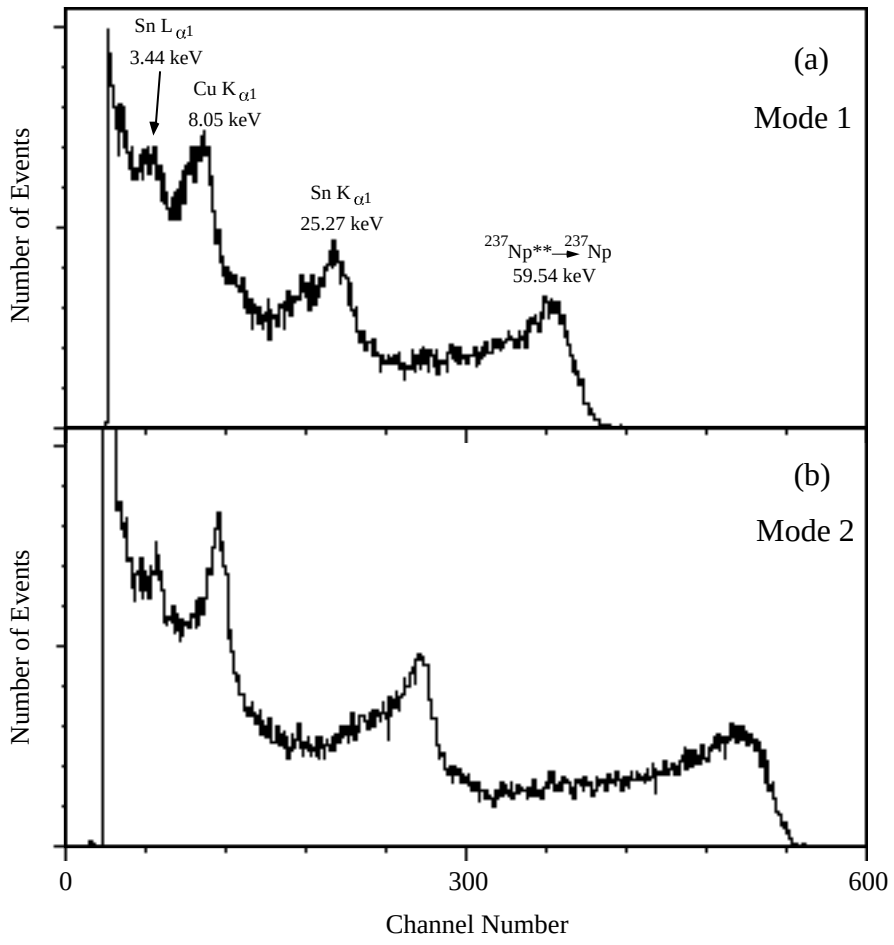

Figure 3.3.6 Calibration phonon pulse height spectra showing the mode dependence of the TES response. (a) Mode 1, and (b) Mode 2.

3.3.4 Mode change effects

The response of the Ti TES changes according to the mode change described in section 3.2.4. In mode 1, just after cooldown, the free electrons and holes excited by particle interactions are trapped after thermallization; they travel an average distance of only ~ 5 μm from the place where they thermallized before they trap. Very little of the gap potential energy is released when the charges trap because the trapping sites are presumably fairly shallow, i.e. close to the band edges. Thus the ~ 1.1 eV per pair stored as the gap potential energy is lost as far as the phonon sensor is concerned.

However, if an electron enters the Schottky barrier region near the surface it will shed ~ 0.5 eV of energy as phonons as it is pulled towards the metal. The further ~ 0.6 eV is shed when the electron enters the metal and relaxes to the fermi level (see figure 3.2.3). An electron, therefore, can deposit energy into the Ti film (contributing to the

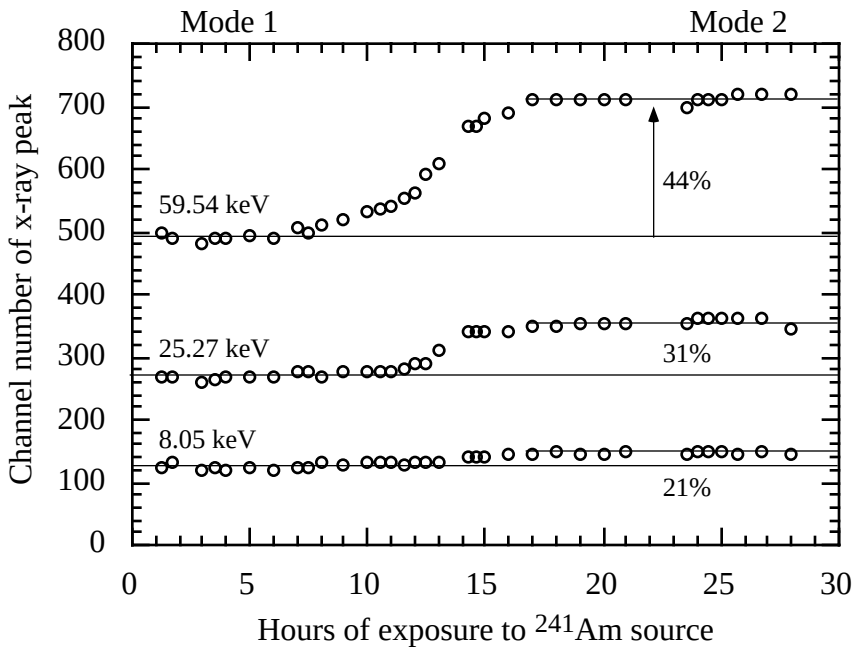

Figure 3.3.7 Typical mode shift time profile. The ^{241}Am source was introduced just after cooldown. Percentages indicate the amount of upward shift seen for each x-ray energy.

TES pulse) if it can reach the metallized surface. Holes are repelled by the Schottky barrier and they possess very little potential energy since the fermi level in the silicon is near the valence band. Thus the holes do not contribute to the TES pulse. In mode 1, only events which occur very near the surface will have a contribution from electrons. 8 keV x-rays have an attenuation length in silicon of only ~ 30 μm so the maximum pulse height events occur close enough to the surface to have some electron contribution to the signal. This is less true of the 25 keV x-rays and even more less true of the 60 keV gamma-rays (signal maximum at depth of ~ 50 μm), so there should be less electron contribution for these events in mode 1 compared to the 8 keV events.

After the shift into mode 2, which was induced by constant exposure to an ^{241}Am source, the position of the peaks in the pulse height spectrum moves up (see figure 3.3.6) [36]. This shift in peak position is attributed to the electron contribution to the TES signal. In mode 2 the electrons can diffuse over large distances (~ 200 μm) and reach the metallized surfaces. The fractional change in peak position depends on the deposited energy: the 8 keV peak moved up 21%, the 25 keV peak moved up 31%, and the 60 keV peak moved up 44% (see figure 3.3.7). The shift in 60 keV peak position is consistent with a change from zero electron contribution in mode 1 to full electron contribution

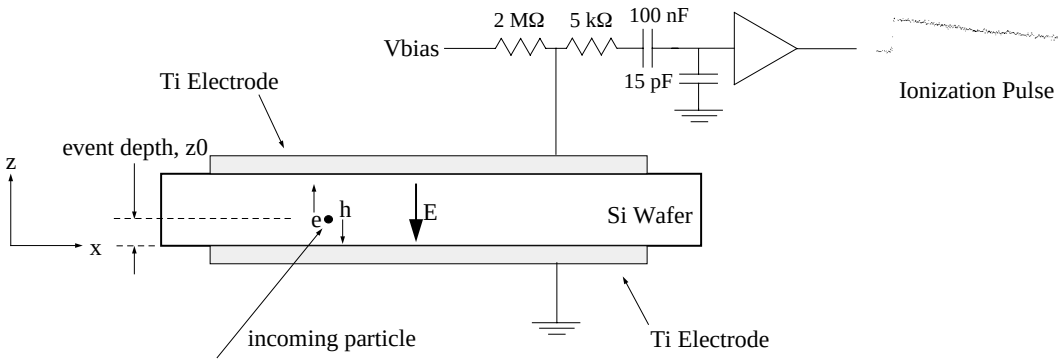

Figure 3.4.1 Schematic diagram of detector for the ionization measurement showing a sample digitized pulse. Electrons and holes excited by a particle interaction in the silicon drift in opposite directions under the influence of the electric field inducing image charge on the electrodes. The ionization pulses have a ~ 30 μs 1/e falltime.

(electrons propagating to the surface just like phonons) to the signal. The expected relative mode 2/mode 1 pulse height increase is 0.31/(1-0.31) ≈ 45%, where 0.31 is the fraction of the deposited energy which is in the electron-hole system and 1-0.31=.69 is the fraction in the phonon system. The relative changes in the 8 keV and 25 keV peak positions are less than ~ 45% because there was some electron contribution in mode 1 for these events. They shift not from zero to full electron contribution but from a non-zero value to full electron contribution. Thus their relative shifts are not as large as that for the 60 keV peak.

3.4 Charge Measurement at Low Temperature

3.4.1 Principles of the charge measurement

In order to measure the amount of free electron-hole pairs produced in an event, we use a detector which has Ti films on both top and bottom surfaces and we disconnect the metal pattern on one side of the wafer from ground in order to apply a dc voltage to it (see figure 3.4.1). This film acts only as an electrode. Since the Si is insulating at our operating temperature, even a small applied voltage creates a reasonably uniform electric field throughout the crystal (except for some fringing near the edges). Electrons and holes generated in an event are separated by this field (they are pulled in opposite directions) and, as they drift through the detector, image charge is induced on both Ti films. The image charge is supplied to the Ti electrode from the ~ 15 pF input

capacitance of the pre-amplifier. (The opposite polarity image charge is supplied to the bottom film through its ground connection.) Alternatively, the drifting charge can be viewed as a transient current which charges the total capacitance at the input of the pre-amplifier. In the present case, a voltage pulse is seen at the pre-amplifier which has a ~ 100 ns rise time, which is the RC time at the pre-amplifier input, and a ~ 30 μs 1/e fall time due to the RC draining of charge through the 2 MΩ resistor.

The voltage pulse height is proportional to the amount of charge excited in the particle interaction and the fractional distance (relative to the detector thickness) that the charge drifts before trapping. The pulse height is inversely proportional to the total capacitance at the input of the pre-amplifier. If an amount of charge ΔQ is induced on the electrodes then a voltage $V = \Delta Q / (C_{det} + C_{in})$ is seen at the input of the pre-amplifier. Ref. [37] shows that a charge moving a distance Δz between two parallel plates, separated by a distance d, in the direction of the electric field induces a charge signal ΔQ on the plates given by

$$\Delta Q = e\frac{\Delta z}{d} \tag{3.7}$$

where e is the electron charge. Thus if a given electron or hole drifts through only half of the detector thickness before trapping then the transient current associated with this charge flows for half the time and the input capacitance of the pre-amplifier is charged only half as much relative to the case when there is no trapping. Note that, in the absence of trapping, if the event occurs at z_0 then the electron drifts a distance $d - z_0$ (anti-parallel to the electric field), giving signal $e(d - z_0)/d$, and the hole drifts a distance z_0, adding ez_0/d to the signal. The total charge signal for this pair is then $Q=[e(d - z_0) + ez_0]/d = e$ independent of z_0. So each pair contributes one unit of charge to each of the capacitor plates.

The ideal response of this type of detector is illustrated in figure 3.4.2. Here the drifting charge is viewed as a transient current which charges the capacitance at the input of the pre-amplifier. Consider an event which excites Q_0 free electron-hole pairs occurring at position z_0 (assume initial charge distribution is a point) in the lower half of the crystal ($z_0 < d/2$). If these charges are very quickly accelerated to their drift velocities then the transient current will have the shape shown in figure 3.4.2(b) where v_{dh} and v_{de} are the hole and electron drift velocities respectively. The voltage transient, also shown in figure 3.4.2(b) is simply given as

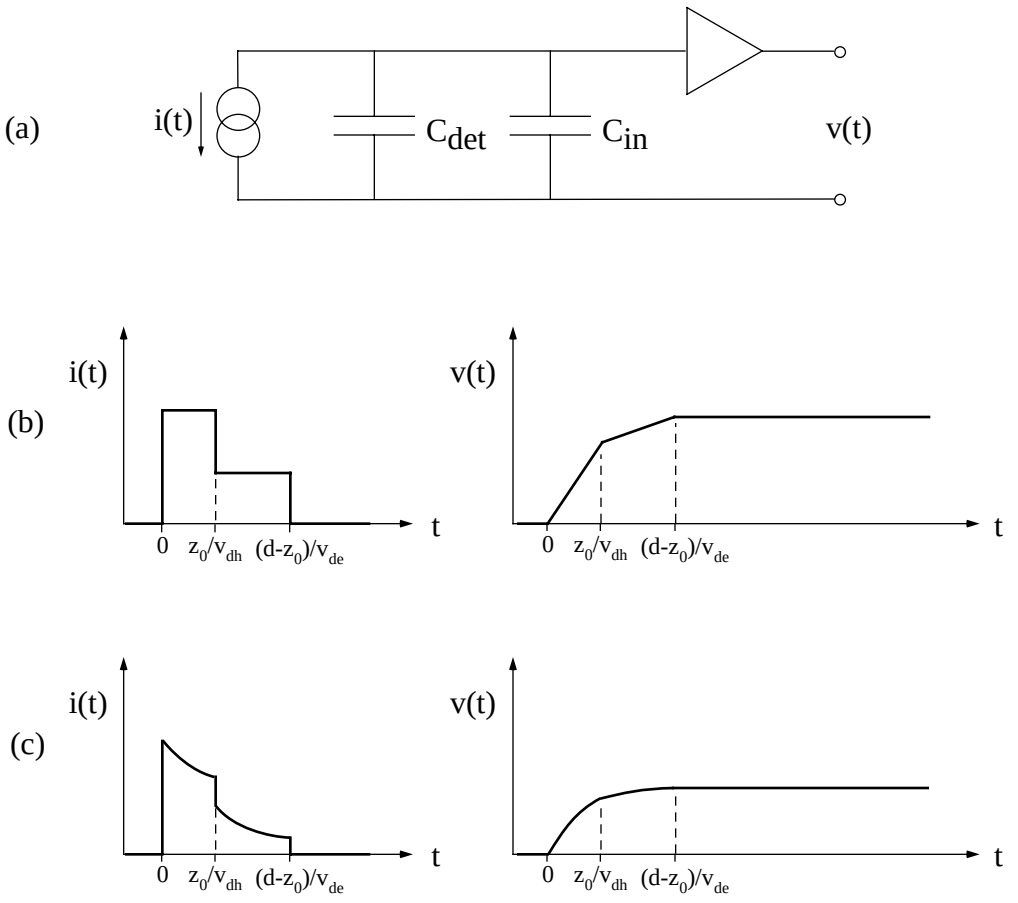

Figure 3.4.2 Ideal response of ionization detector discussed in section 2.4.1. (a) Drifting charge is a current transient, i(t), which charges the total capacitance at the input of the pre-amplifier. The resulting voltage signal is v(t). (b) Current and voltage transients with no trapping. The detector thickness is d, the event occurs at position z_0 (see figure 3.4.1), and v_{dh} and v_{de} are the hole and electron drift velocities. (c) Current and voltage transients with charge trapping along the drift.

$$v(t) = \frac{1}{C_{in} + C_{det}} \int i(t)dt \,. \tag{3.8}$$

This voltage transient is at first linearly charged by the current from the drifting electrons and the drifting holes. When the holes reach the surface of the crystal at time $t = z_0/v_{dh}$ their contribution to the current ceases and a step appears in the current transient. This

step induces a kink and change in slope for the voltage transient. The electron current continues to flow until time $t = (d - z_0)/v_{de}$ when the electrons are collected at the opposite electrode. After the current has returned to zero ($t > (d - z_0)/v_{de}$) the voltage signal remains at a constant value $v(t) = Q_0 / (C_{det} + C_{in})$.

If there are trapping processes in operation during the free charge drift, then the transient shapes are modified as shown in figure 3.4.2(c). The transient current is attenuated as the charges drift and are trapped. As time goes on fewer and fewer charges are left untrapped to contribute to the current. If the probability of trapping is a constant per unit drift length then the current attenuation is exponential (number of charges trapped per unit drift length proportional to the number of charges still moving). The attenuation of the current also affects the voltage signal. The front edge of the voltage transient is rounded instead of linear. There is still a kink at $t = z_0/v_{dh}$ but it is less pronounced. The flat part of the voltage transient for $t > (d - z_0)/v_{de}$ is now lower than the case with no trapping since according to eqn. 3.7 the trapped charge contributes less to the signal when it does not travel all the way through the detector.

This analysis of the current and voltage transients demonstrates that there is a lot of useful information in the current transient or the leading edge of the voltage transient. If the event location z_0 is known this technique can be used to measure v_{dh} and v_{de} as functions of electric field and temperature. Conversely, if v_{dh} and v_{de} are known then the transients allow the measurement of z_0 which can be useful for defining a fiducial volume for the detector (for background suppression for example, see section 1.3). In the case of charge trapping, the shape of the transients directly relate to electron and hole trapping lengths under the conditions of the experiment. Furthermore, if the temperature of the detector is high enough that some of the trapped charge is thermally de-trapped (slow rise in v(t) or long tail in i(t) for $t > (d - z_0)/v_{de}$), then the temperature dependence of the de-trapping measures the trap depth. An excellent review of this technique, called "transient charge technique," and its applications is given in Ref. [38].

One of the main difficulties with this technique is the need for very fast amplifiers. The drift times are of order $\sim d/v_{de}$. For our detectors $d \sim 300$ μm and v_{de} is $\sim 10^6$ cm sec^{-1} which gives $t_{drift} \sim 30$ ns. In order to resolve a transient which is only 30 ns long we need an amplifier with a bandwidth of ~ 250 MHz. A low noise amplifier with this bandwidth and a white noise level of 1 $nV_{rms}/\sqrt{Hz}$ has an integrated noise level of 15 μV_{rms}. For typical input capacitance of ~ 20 pF we need to collect $Q = CV \sim 2 \times 10^3$ electron-hole pairs just to equal the rms voltage noise. For useful signal to noise one would like the signal charge to be much larger than this 2×10^3 pairs.

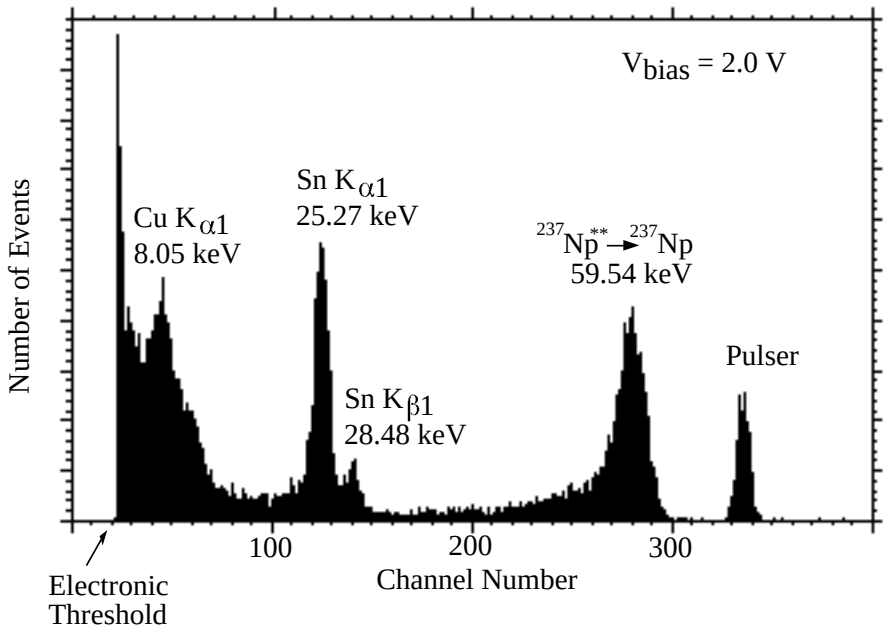

Figure 3.4.3 Sample pulse height spectrum for the ionization measurement. The applied bias is 2.0 V (E ~ 60 V/cm). The resolution is 2 keV FWHM at 25 keV. The pulser peak measures the amplifier noise contribution to the width of the data peaks.

The "transient charge technique" is very successful in experiments where the free carriers are excited by a pulse of high-energy electrons (~ 10^4 30 keV electrons) [39, 40, 41, 42] or by alpha-particles (E ~ 5^+ MeV). In these experiments the number of free carriers which are excited per pulse is controlled by the electron gun and varies from ~ 10^6 -10^9 electron-hole pairs. Here the signal-to-noise ratio can be quite large. However, for our application of dark matter detection, the energy range of interest is much lower: we wish to understand the response of the detector to energy depositions of only a few tens of keV. An absorbed 60 keV gamma-ray produces only ~ 2 x 10^4 electron-hole pairs in silicon. This would give a low signal-to-noise ratio using a fast amplifier for the transient charge technique, to say nothing of the difficulties involved in implementing a 250 MHz bandwidth amplifier in the cryostat. In the event, a cryogenic pre-amplifier was used which has a bandwidth of 10 MHz and a white noise level near 1 nV/√Hz above ~ 50 kHz [17] (see section 2.2). This amplifier gave an RC limited pulse risetime of ~ 100 ns, too long to see any transient effects on the front edge of the voltage pulse (we did see some rounding of the front edge of the pulse at very low electric field in the thickest samples tested). We were typically able only to measure the height of the pulse (number of charges collected). The ideal detector response predicts a pulse which is flat with time after the transient current is over. This condition is not realized because the input

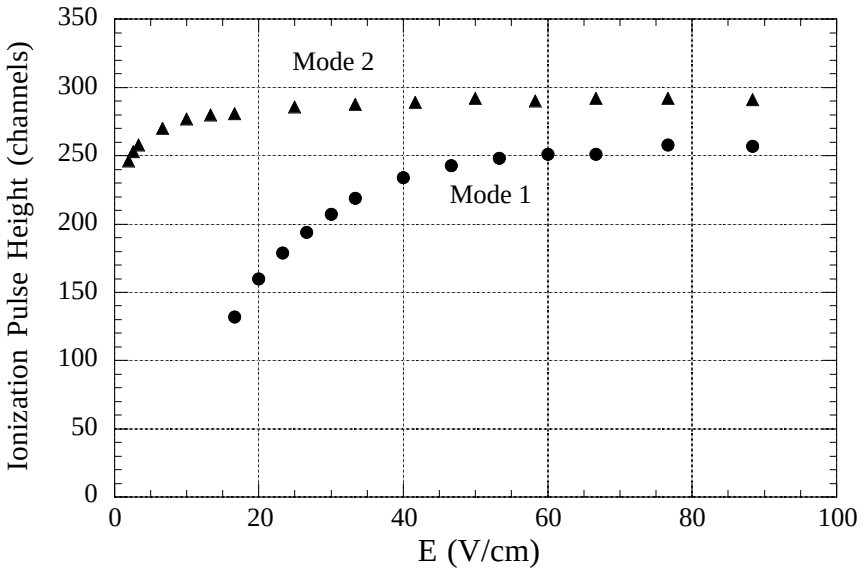

Figure 3.4.4 Ionization pulse height for 60 keV events versus electric field for Mode 1 and Mode 2. Charge collection efficiency is better at low field for Mode 2 compared to Mode 1.

capacitance discharges slowly (~ 30 μs 1/e time) through the 2 MΩ resistor shown in figure 3.4.1.

A set of voltage tail pulses can be turned into a pulse height spectrum such as that shown in figure 3.4.3. Here the detector was exposed to photons of energy 8, 25, and 60 keV. The pre-amp noise was added to a clean (essentially noiseless) pulse from a pulse generator in order to measure the electronics noise contribution to the widths of the spectral peaks. The electronics noise limited energy resolution is ≈ 2 keV FWHM at 25 keV (resolution at 60 keV is 4 keV FWHM which is not electronics limited).

3.4.2 Mode change effects

The position of the peaks in the spectrum depend on the applied electric field. The charges are more efficiently collected with a larger electric field. As the field is lowered, more of the free charges created in an event are lost and the signal size drops. This is qualitatively understood as charge trapping on impurities; the cross section for trapping is expected to drop with an increase in electric field, hence better charge collection at higher fields. This charge loss at low electric field will be explored in depth in chapter 5.

Since in mode 1 the crystal contains ionized impurities which are fairly strong traps, we expect the charge collection to be poor compared to mode 2 (no ionized impurities) at the same applied electric field. This behavior is in fact seen in figure 3.4.4. The charge collection efficiency (position of peak relative to its maximum value) does drop with electric field in both modes but it remains high for lower fields in mode 2. Thus the detector response is much better in mode 2 compared to mode 1 as far as charge collection at low electric field is concerned.

CHAPTER 4: NUCLEAR-RECOIL/ELECTRON-RECOIL DISCRIMINATION

In the WIMP dark matter search that we envision, low event rates are expected (~ 1 event/kg/day). Thus, one is faced with the difficulty of separating the events of interest (nuclear-recoils) from background events (mostly electron-recoils) (see chapter 1). An attractive background rejection technique involves the discrimination of event types based on the different partitioning of energy into phonons and ionization. In solid state materials, low-energy nuclear-recoils dissipate more energy into phonons, and less into ionization, than do equal-energy electron-recoils. A detector which measures both signals simultaneously can then be used to veto typical backgrounds due to charged particles and photons on an event by event basis. The only significant remaining background for nuclear-recoils is due to neutrons from the experimental surroundings, but careful selection of materials and shielding can be used to avoid these events.

This discrimination technique has been successfully demonstrated using slow (~ few msec) thermistors attached to 60 g Ge [43] and 1 g Si [44] crystals. In this chapter, we will demonstrate the discrimination with a Si detector using a much faster (~ μsec) Ti transition edge sensor (TES) as the phonon detector. The faster response time allows such sensors to be sensitive to event location, which further improves background rejection capabilities. In addition, the fast response makes better use of a fast muon veto signal from plastic scintillators surrounding the dark matter search experiment (see section 6.4). The detector can resolve event location in two dimensions, and can completely discriminate nuclear-recoils from electron-recoils for about 50% of nuclear-recoil events.

4.1 Simultaneous Phonons and Ionization

4.1.1 Effects of applied electric field on TES response

As free charge drifts through the crystal under the influence of an electric field, the energy gained from the field is subsequently released as phonons. These "Luke Effect" phonons [45] "contaminate" those generated in the particle interaction. In other words, the charge measurement disturbs the phonon measurement. Since the total energy shed by a charge (q) drifting through a potential V_{bias} is given by $E = q\ V_{bias}$, V_{bias} must be kept as small as possible in order to minimize the contamination. Of the ≈ 3.6 eV that goes into creating an electron-hole pair in silicon, ≈ 2.5 eV goes into phonons and the remaining ≈ 1.1 eV is stored as the gap potential energy. We wish to limit the drift-

induced phonon energy to less than the original 2.5 eV per electron-hole pair. For the experiments described here this limit requires $V_{bias} < 2.5$ V. For $V_{bias} < 0.5$ V ($E < 20$ V/cm) the charge collection efficiency drops dramatically due to trapping, particularly in mode 1 (see figure 3.4.4).

The TES phonon sensor is not a calorimetric detector. It does not sense all of the energy shed as "Luke" phonons by the drifting charge. Only a fraction of this phonon energy contributes to the TES signal. In this respect the TES has an advantage over thermometer/calorimeter type phonon measurements since those detectors are much more sensitive to the drift induced phonon contamination because they measure the total energy deposited into the detector heat capacity (drifting the charge with an electric field is doing work on the crystal).

The details of the TES response to drift induced phonons are not understood. Regardless, under specific experimental conditions (temperature, electric field, dc bias current, etc.) the response of the TES can be "calibrated" by the shape of the ear plot described in section 3.3.3. Some general, qualitative points can be made. First, the phonon pulse height does generally increase with applied bias. This trend is shown for mode 1 in figure 4.1.1 and for mode 2 in figure 4.1.2.

In figure 4.1.1 the TES response is shown for a progression of positive and negative applied voltages across the 300 μm thick silicon substrate. The maximum phonon pulse height is seen to increase with applied bias more quickly with negative bias than with positive bias. For negative bias the electrons drift toward the TES and the holes drift away from it. The opposite is true of positive applied bias. The electrons, upon reaching the TES film, can deposit a significant amount of energy (near the full gap) when they relax to the fermi level. This effect, in combination with the contribution of "Luke" phonons during drift, should increase with larger applied voltage. The holes, however, are blocked by the Schottky barrier contact and, in addition, they carry very little potential energy since the fermi level is near the valence band in p-type silicon at low temperature. Thus, drifting holes will contribute only drift-induced "Luke" phonons to the phonon system and will not contribute any "extra" energy to the TES from the gap as do electrons. This difference may explain the peak phonon pulse height versus applied bias behavior seen in figure 4.1.1. Alternatively, if the holes are trapped more strongly than the electrons then they will not emit as much phonon energy as they drift toward the TES.

It can also be seen in figure 4.1.1 that the part of the ear plot for 60 keV events separates from the rest of the curves when the applied bias reaches ~ -1.0 V. This means

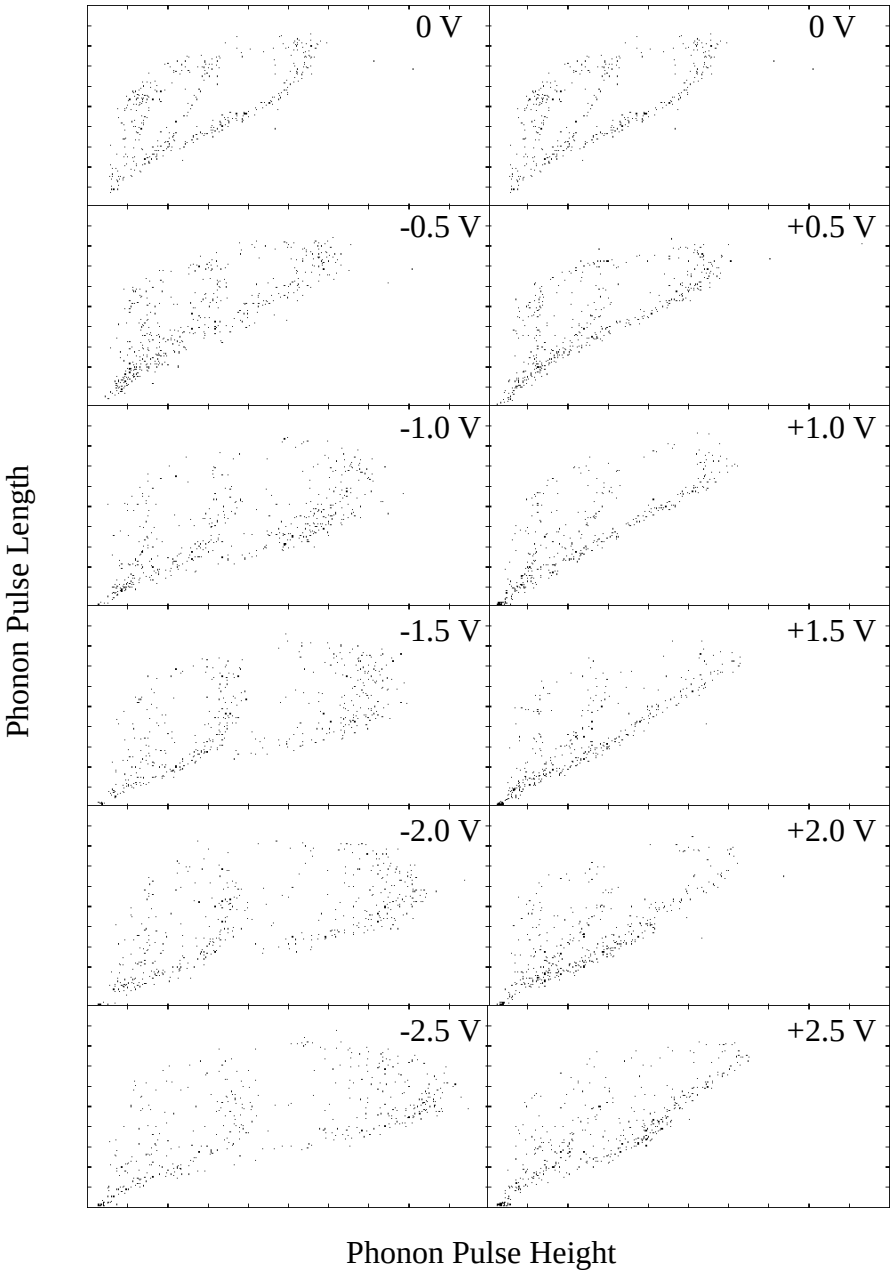

Figure 4.1.1 Mode 1 ear plots as a function of applied bias. The bias is applied in order to make the ionization measurement (see figure 4.1.3). The 300 μm thick detector was exposed to 8, 25, and 60 keV photons.

that the TES is detecting events throughout the crystal thickness since there is both a maximum and a minimum phonon pulse length. The 60 keV curve further separates as the negative bias is increased. In contrast, for positive bias the 60 keV curve does not

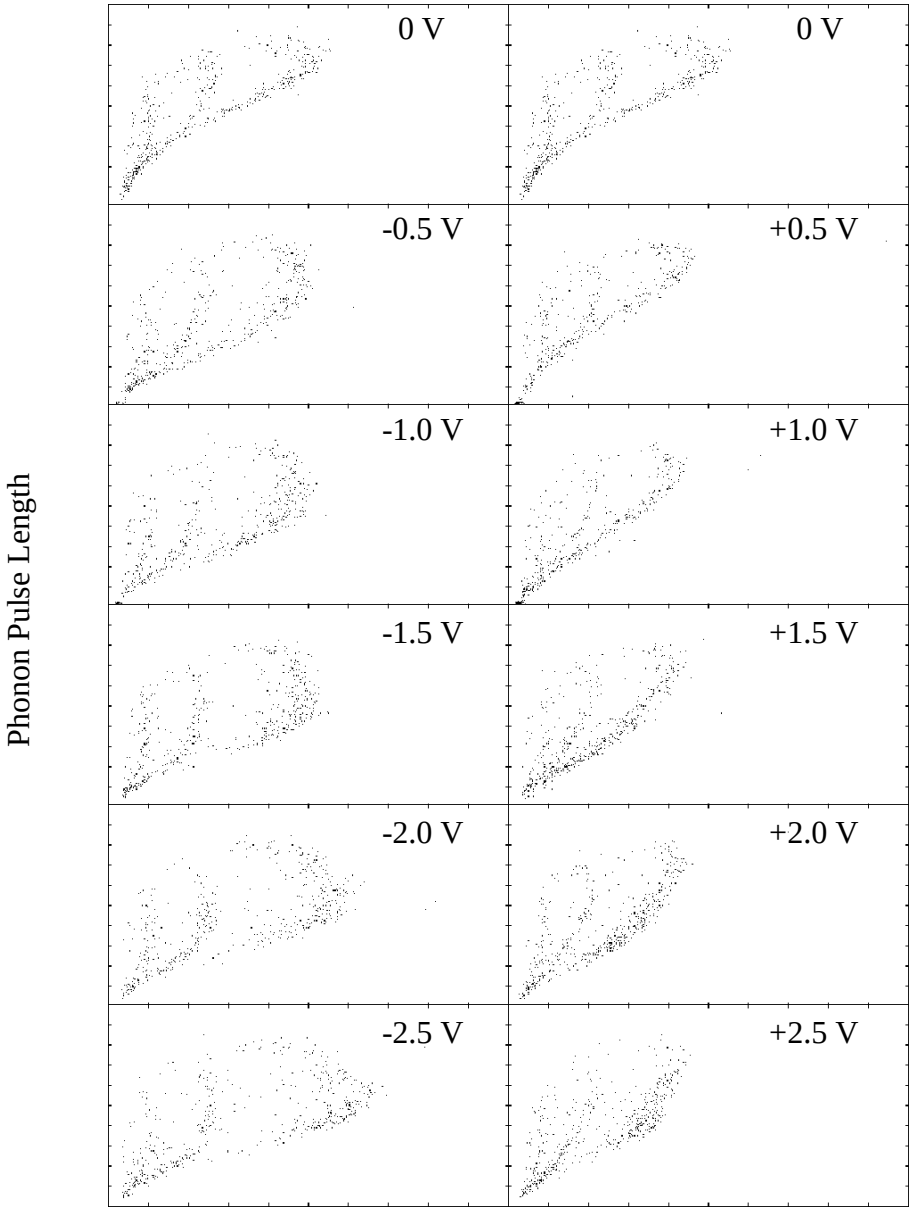

Figure 4.1.2 Mode 2 ear plots as a function of applied bias. The bias is applied in order to make the ionization measurement (see figure 4.1.3). The 300 μm thick detector was exposed to 8, 25, and 60 keV photons.

separate in the same way until the applied bias is ~ +2.5 V. Also note the different shape to the ear plots for positive and negative bias.

Figure 4.1.2 gives a similar set of data for mode 2. The trends in the data are similar to those in mode 1 (figure 4.1.1) with some interesting differences. First, the peak

phonon pulse height drops with applied bias (for bias < ± 0.5 V) before increasing again. For applied bias greater than ± 0.5 V the peak signal monotonically increases with bias. This behavior can be qualitatively explained as a competition between the restriction of the free charge diffusion by the applied electric field causing the electron potential energy to be deposited into a smaller region of the TES film (giving a smaller signal) (the applied field forces electrons to largely move along field lines rather than freely diffuse) and the overall increase in phonon energy from the "Luke" effect. At small applied bias the drift induced phonon energy is small and yet the electric field can restrain the electron diffusion transverse to the field. As the bias is increased the drift induced phonon energy grows and eventually overcomes the signal loss due to the restriction of the electron diffusion. This picture fits nicely with the explanation of the TES mode dependence (section 3.3) being due to electrons entering the Ti film in mode 2.

The other trends in the data that were seen in mode 1 are also seen in mode 2. For example, for bias greater than ± 0.5 V the peak phonon pulse height increases more slowly with positive bias compared to negative bias. In addition, the onset of the 60 keV curve separating from the other curves in the ear plot occurs at -1.0 V and +2.5 V. Notice also the extreme shape difference for applied bias of ± 2.5 V. As was stated above, although these effects are not unambiguously understood they are to some extent irrelevant from the point of view of the operation of the detector since they can be calibrated out. From a scientific point of view, however, one would like to understand the behavior in detail.

4.1.2 Effects of TES measurement on the charge signal

The detector acts in figure 4.1.3 as a ~ 3 pF capacitor with the dielectric silicon electrically coupling the phonon and ionization sensors together. During an event detection, a small resistive region forms in the TES, thus changing the potential on a portion of this metallic contact which otherwise forms the ground plane of the ionization sensor. An image of the TES pulse is then seen in the ionization channel (see figure 4.1.3). The voltage change on part of the TES can be seen as a transient charge on C_2, C_{2stray}, and the input capacitance of the phonon channel pre-amplifier. This charge is quickly supplied by the bias current I_{bias}. An equal charge is supplied to the other side of C_2 and C_{2stray} from the input capacitance of the ionization channel pre-amplifier.

The detector capacitance is divided into C_1 and C_2 (where $C_1 + C_2 = C_{det}$) which are separated in the phonon channel by the event-induced region of time-dependent resistance R(t). The detected phonon pulse is given by $V_{phonon}(t) = I_{bias}R(t)$, and its

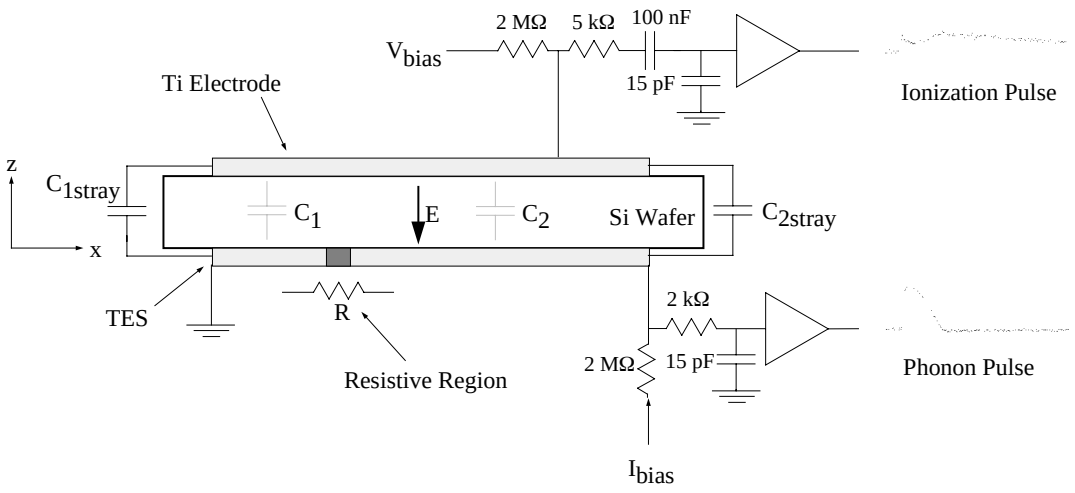

Figure 4.1.3 Schematic diagram of detector for simultaneous measurement of phonons and ionization showing sample digitized pulses. Typical phonon pulses are ~ 5 μs long. The vertical scale and size of the resistive region are exaggerated. C_1 and C_2 refer to the discussion in section 4.1.3.

image on the ionization channel is coupled through C_2 and C_{2stray} only (the stray capacitances are due to bonding pads and leads). The size of this "crosstalk" pulse depends on the relative size of C_1 and C_2. If the resistive region (particle interaction location) occurs near the phonon sensor ground connection, then C_1 is very small and $C_2 \approx C_{det}$. In this instance the crosstalk has its largest magnitude. At the opposite extreme, when the resistive region occurs near the I_{bias} end of the phonon sensor, C_2 is small, $C_1 \approx C_{det}$ and the crosstalk has its minimum magnitude. The crosstalk never vanishes due to the stray capacitance. Thus, the magnitude of the crosstalk between the two detector channels measures the position of the event in the x-direction, as shown in figure 4.1.3. Figure 4.1.4 shows some sample pulse pairs which have different amounts of crosstalk (different event position along x).

4.1.3 Position measurements in two dimensions

In order to properly measure the height of the ionization pulse we need to subtract out the crosstalk. We must therefore account for the different electronic networks at the front end of the ionization and phonon channels. A phonon pulse can be thought of as a transient charge of ~ 5 μsec duration appearing on C_2, C_{2stray}, and the input capacitance of the TES pre-amplifier. Due to the capacitive coupling between sensors an equal charge appears on the ionization channel. This charge drains away with the ~30 μsec RC

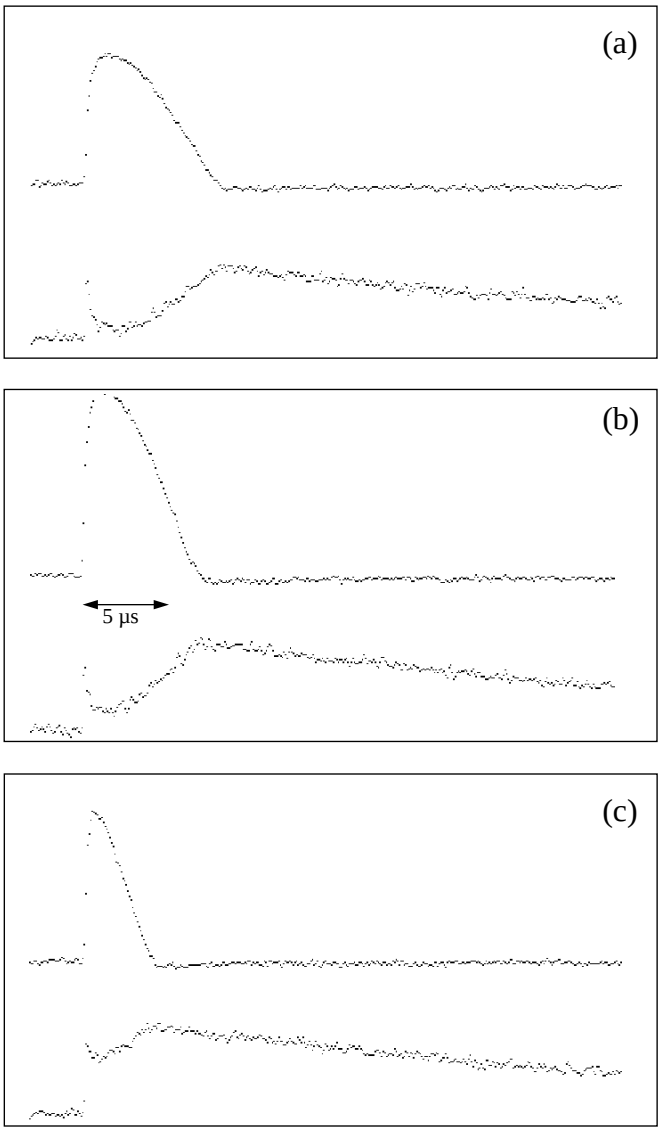

Figure 4.1.4 Sample digitized phonon (top) and ionization (bottom) pulse pairs showing varying amounts of "crosstalk" (see section 4.1.2 and figure 4.1.3). (a) Large crosstalk fraction for event near the TES ground connection. (b) Event near the center of the TES. (c) Small crosstalk fraction for event near the TES's I_{bias} connection.

time of the ionization network. Thus the image pulse is not an exact replica of the TES signal; it is shaped by this RC time. The two channels have different frequency response, and therefore different impulse response, at the input. The TES channel can accurately

follow an impulse of charge while the ionization channel's response is a tail pulse which falls exponentially with time.

The pulse shaping in the ionization channel can be solved analytically (see figure 4.1.5). The phonon pulse is considered as a sum of small additions (voltage rising with time) and subtractions (voltage falling with time) of charge dq to and from C_2, C_{2stray}, and the input capacitance of the TES pre-amplifier. The TES channel amplifier can follow these changes and give an accurate reproduction of the TES pulse shape. The ionization channel responds to each dq with a tail pulse. The resulting time response in the ionization channel to a phonon pulse is a sum of many tail pulses, each delayed in time from the previous one by dt, as illustrated in figure 4.1.5(c). Figure 4.1.5(a) shows a typical phonon pulse $f_p(t)$ which appears at the input of the ionization channel pre-amplifier via the capacitive coupling through the silicon substrate; $f_p(t)$ can be regarded as a charge signal $q_p(t)$ through the relation $q_p(t) = C\, f_p(t)$, where C is the relevant capacitance. Figure 4.1.5(b) gives the amount of charge which is added or subtracted to the capacitance for each time interval dt,

$$dq_p = C\frac{df_p(t)}{dt}dt \tag{4.1}$$

and the resulting tail pulses are shown in figure 4.1.5(c). At a given time t, the charge $q_i(t)$ on the ionization channel side of the capacitance is equal to the sum of all the dq_p's up to that time taking into account the decay of the tail pulses for times t' earlier than t,

$$q_i(t) = C\int_0^t \frac{df_p(t')}{dt'} e^{-(t-t')/\tau} dt' \tag{4.2}$$

where the time constant $\tau \sim 30$ μsec. Eqn. 4.2 can be rewritten using integration by parts

$$q_i(t) = Cf_p(t')e^{-(t-t')/\tau}\Big|_0^t - C\frac{e^{-t/\tau}}{\tau}\int_0^t f_p(t')e^{t'/\tau}dt'. \tag{4.3}$$

Since $f_p(0) = 0$ we can evaluate the first term on the right hand side in Eqn. 4.3, and dividing by the capacitance, we obtain the final analytical form of the shaping

$$f_i(t) = f_p(t) - \frac{e^{-t/\tau}}{\tau}\int_0^t f_p(t')e^{t'/\tau}dt'. \tag{4.4}$$

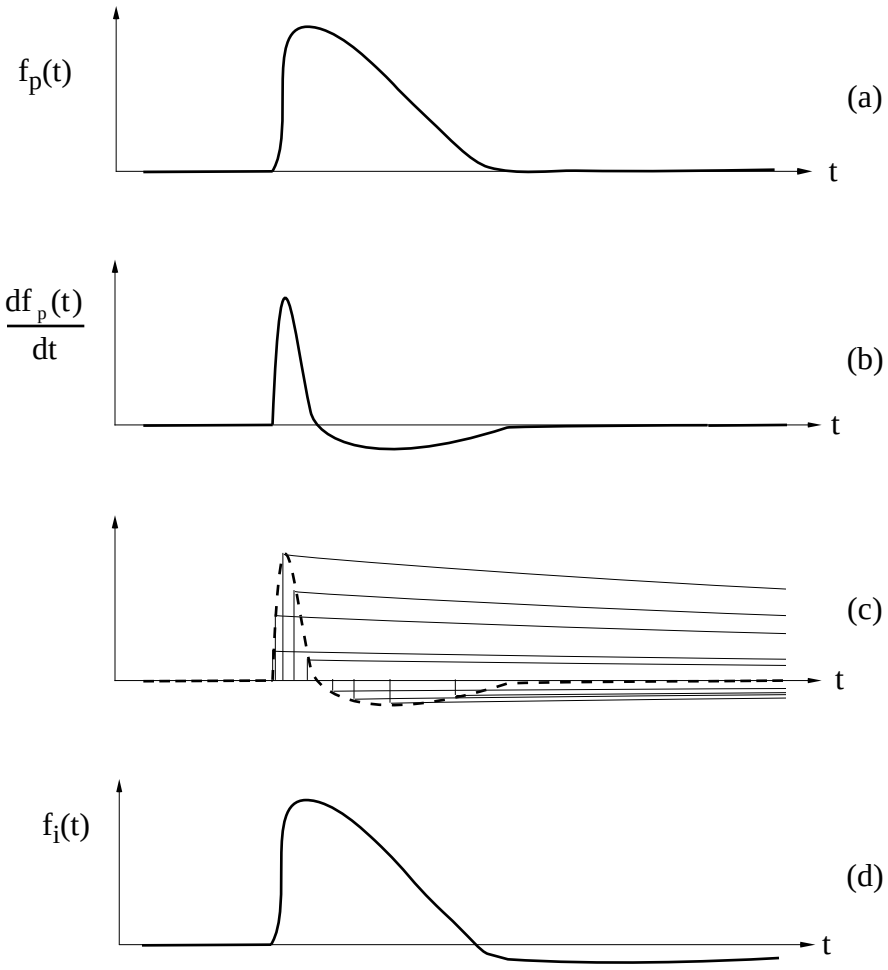

Figure 4.1.5 Illustration of pulse shaping by the front-end of the ionization channel pre-amplifier (see discussion in section 4.1.3). (a) Shape of the ~ 5 μs phonon pulse, $f_p(t)$, coupled through the detector. (b) Derivative of (a) with respect to time. (c) Representation of the response of the ionization channel to the time-profile in (a). (d) The shaped pulse, $f_i(t)$, seen at the ionization channel with the same vertical scale as (a). Note the long, ~ 30 μs falltime undershoot

The shaped pulse is shown in figure 4.1.5(d).

In the experiments, we digitize and store both the phonon and ionization voltage pulses. We then shape the phonon pulse in software and add a fitted fraction of this shaped pulse to the ionization signal in order to remove the crosstalk. This process results in a straight tail pulse with τ ~ 30 μsec from which it is straightforward to extract

the height. Hence we determine both the height of the tail pulse and the crosstalk fraction, yielding measurements of the amount of ionization generated and the event location along the x-direction for each event. Our detector then measures both ionization and phonons with a few keV resolution and is sensitive to event location in 2 dimensions (x by crosstalk, z by phonon pulse length). Both energy measurements have an electronics threshold of ~3 keV.

4.2 X-ray and Gamma-ray Experiment

The results of two experiments are shown in Figure 4.2.1. The first experiment was the simultaneous measurement of phonons and ionization for electron-recoils using an ^{241}Am source of 59.54 keV gamma-rays, including fluorescence x-rays from Cu (8.05 keV) and Sn (25.27 keV). In Figure 4.2.1(a) the plot of ionization pulse height vs. phonon pulse height shows horizontal bands for each of the three photo absorption energies. These bands terminate at points which lie roughly on a line given by the ionization efficiency for electron-recoil events (which is independent of energy) and by the maximum pulse heights observed with the phonon sensor. The "tails" leading down to lower TES pulse heights are due to the depth dependence of phonon signals. Approximately 2/3 of the events occur in the dark group of points at the end of the bands. Of particular importance is the lack of events below and to the right of the line connecting the ends of the bands. Since nuclear-recoils partition more energy into phonons, and less into ionization, than do equal-energy electron-recoils, we expect nuclear-recoil events to extend past this line.

Figure 4.2.1(a) also shows the crosstalk vs. ionization plot and the phonon pulse length vs. ionization plot. In the crosstalk vs. ionization plot most of the events occur with crosstalk fractions between 25% and 63%. Because this fraction reflects the position of an event along the TES (x direction in figure 4.1.3), the edges of the dark band in the center of the plot correspond to events at the edges of the Ti film. The crosstalk fraction does not extend to 0 or 1 because of the ~ 2 pF stray capacitances shown in figure 4.1.3. Since the width of the sensor in the x direction is 2 mm, the sharpness of the edges (HWHM) in this plot indicates a position resolution along x of ~ 0.2 mm. Events occurring beyond the sensor edges produce artificially small phonon pulses, which, due to computational errors on very small pulses, lead to crosstalk fractions below 25% and above 63%. We can make a mild fiducial volume cut on the crosstalk fraction (shown by arrows in figure 4.2.1(a)) to exclude these edge events. The edge events can also be

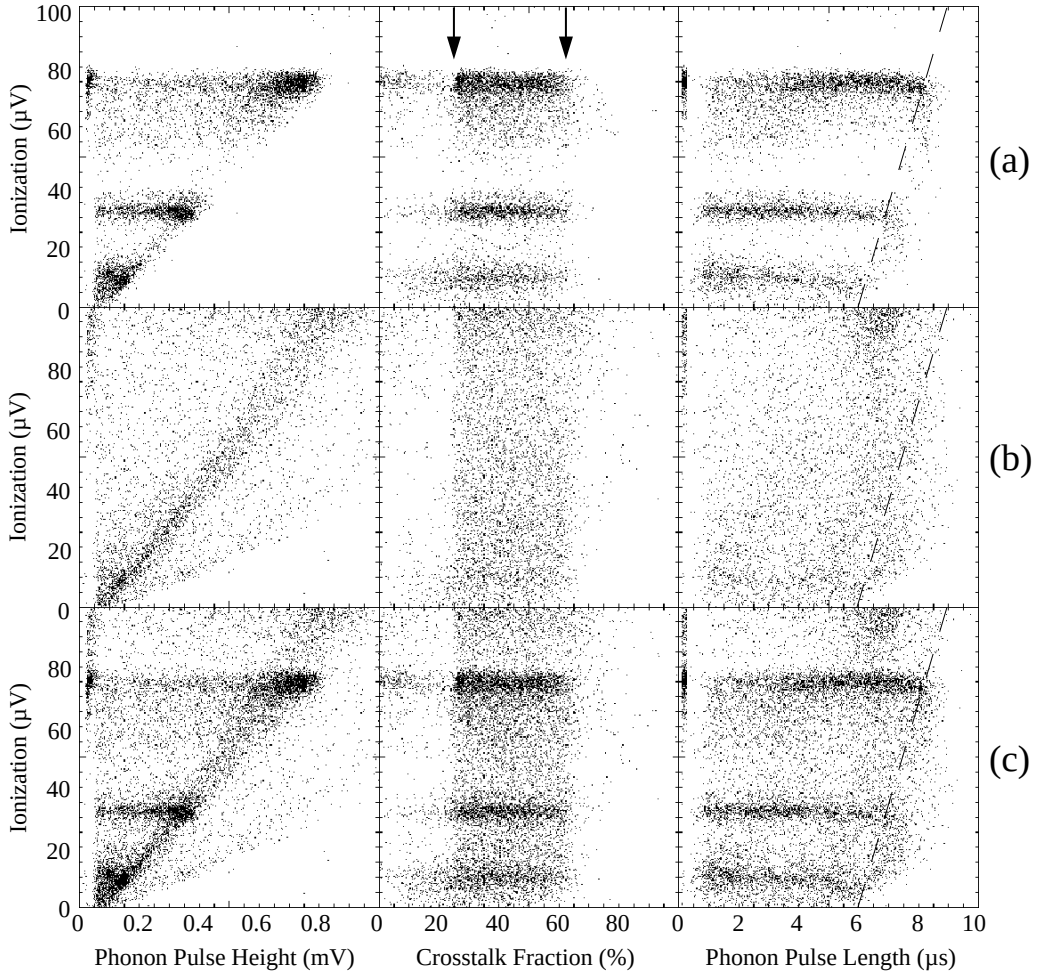

Figure 4.2.1 Data from simultaneous measurement of phonons and ionization. (a) The x-ray and gamma-ray experiment. Horizontal bands are due to ionization peaks from 59.54 keV, 25.27 keV, and 8.05 keV energy depositions. (b) The neutron and gamma-ray experiment. (c) A superposition of (a) and (b). The arrows and dashed lines indicate where fiducial volume cuts will be made.

avoided by eliminating events with small phonon pulse height, but this introduces an artificially high threshold in the phonon measurement.

The phonon pulse length is a monotonic function of the depth of the event (z direction in figure 4.1.3). Long pulses correspond to events close to the detecting surface and short pulses correspond to events deep in the crystal. For 60 keV (25 keV) photons the shortest phonon signals correspond to events ~ 100 μm (70 μm) from the detecting surface giving a resolution in event depth of ~few μm. It is evident in figure 4.2.1(a) that near surface events (longest phonon pulse lengths) give poorer charge collection (vertical

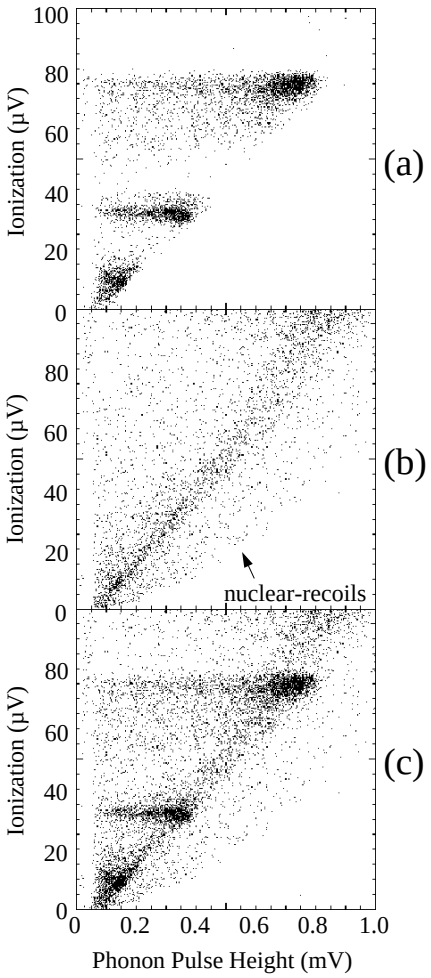

Figure 4.2.2 Ionization pulse height vs. phonon pulse height plots (same as figure 4.2.1) after the fiducial volume cuts discussed in the text and shown in figure 4.2.1. (b) Shows the region of nuclear-recoil / electron-recoil discrimination. (c) is a superposition of (a) and (b).

"tails" in figure 4.2.1(a) right) for each of the three photon energies. This effect is probably due to electrons escaping from the crystal since the phonon signal is also reduced in figure 4.2.1(a) left. These events can be excluded by another fiducial volume cut shown as a dashed line in Figure 4.2.1(a). Figure 4.2.2(a) shows the data after the two cuts have been applied.

Since the ionization measurement is an independent energy measurement we can use it to isolate particular energy depositions in the phonon pulse ear plots. If a cut is made on the data to exclude events which deposit more or less than a particular amount of ionization then the earplot for the energy which corresponds to that particular amount

of ionization only results. This type of cut on the data is given in figure 4.2.3 where each x–ray or gamma-ray energy is separately displayed. It can be seen in the figure that the simultaneous measurement of phonons and ionization allows an unambiguous energy measurement for small phonon pulses. In the standard ear plot these energies cannot be distinguished since any energy deposition event will give a small, short phonon pulse if it occurs sufficiently far from the detecting surface.

4.3 Neutron and Gamma-ray Experiment

In another experiment the detector was exposed to a broad spectrum of neutrons and gamma-rays from a PuBe source. Figures 4.2.1(b) and 4.2.2(b) show the results of this experiment. The ionization pulse height vs. phonon pulse height plot shows a dark, diagonal band corresponding to where electron-recoil events give maximum phonon pulse height. Events having the same ionization pulse height but larger phonon pulse height than those in this band are due to nuclear-recoils. A comparison between figures 4.2.2(a) and 4.2.2(b) shows nuclear-recoil/electron-recoil discrimination of > 1000:1 in the region below and to the right of the band. However, there are some nuclear-recoil events which extend down into the electron-recoil region since deep nuclear-recoils will give small phonon signals. Since ~ 2/3 of the events occur near the largest phonon pulse height for electron-recoils, we can conservatively estimate that ~ 50% of the nuclear-recoil events have a large enough phonon pulse height to be distinguishable from electron-recoils. Figures 4.2.1(c) and 4.2.2(c) are superpositions of the data from the x-ray and gamma-ray experiment and the neutron and gamma-ray experiment.

The ionization efficiency for low energy nuclear-recoils varies non-linearly with energy and decreases with decreasing recoil energy. If K is the nuclear recoil energy and E is the energy dissipated as ionization (both measured in units of keV) then $E \approx 0.17\ K^{1.23}$ [46]. Thus, the ionization axis in figures 4.2.1(b) and 4.2.2(b) is a non-linear energy scale for nuclear-recoils. The scale varies as the following: 10 μV ionization signal ≈ 23 keV, 30 μV ≈ 58 keV, 75 μV ≈ 119 keV. For electron-recoils the scale is linear and gives a full scale range of 100 μV ionization signal ≈ 80 keV.

We can again make a cut on the ionization axis to isolate events which deposit a particular amount of ionization. This allows us to study the TES response to monochromatic nuclear-recoils. This is a useful technique since even a monochromatic beam of incident neutrons will produce a broad range of energy depositions in the silicon

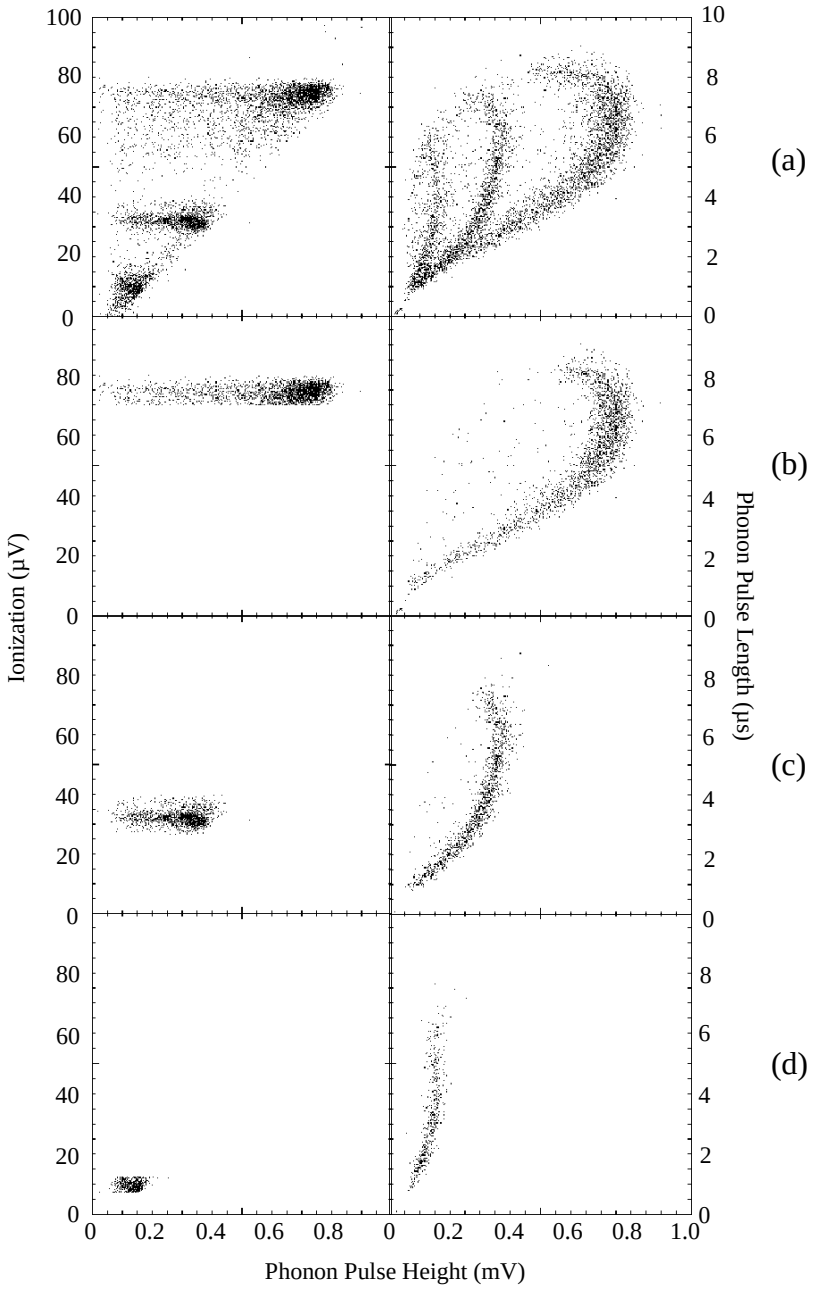

Figure 4.2.3 Response of the TES to events which deposit a fixed amount of ionization in the x-ray and gamma-ray experiment. (a) All the data. (b) Events near 60 keV only. (c) 25 keV events. (d) 8 keV events. The simultaneous measurement of phonons and ionization allows an unambiguous energy determination for events with small phonon signal.

crystal by elastically scattering at all angles. A common but more difficult way to isolate nuclear-recoil energy depositions in conventional detectors is to use coincidence between

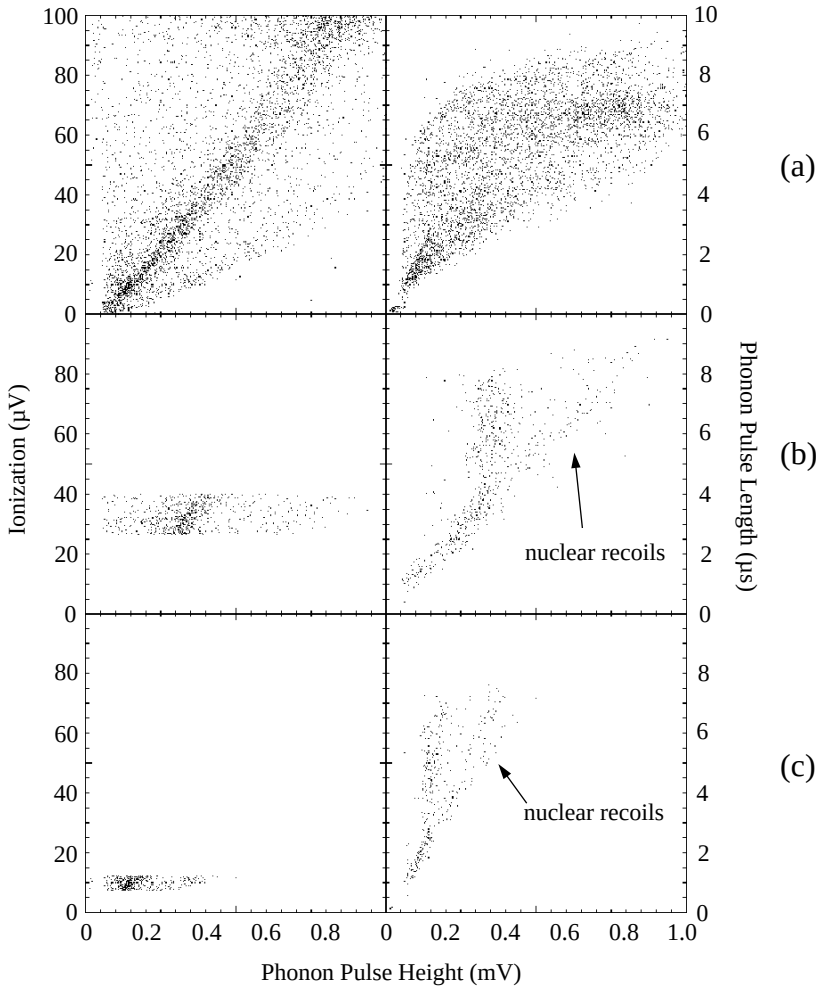

Figure 4.3.1 Response of the TES to events which deposit a fixed amount of ionization in the neutron and gamma-ray experiment. (a) All the data. (b) Ear plot for ionization near 25 keV equivalent x-ray energy only (compare to figure 4.2.3(c)). (c) Same as (b) but for 8 keV (compare to figure 4.2.3(d)). The events at large phonon pulse height (above the x-ray ears) are due to nuclear-recoils which deposit the corresponding amount of ionization only.

two detectors to kinematically reconstruct the recoil. Our technique is simpler and is illustrated in figure 4.3.1.

Figure 4.3.1(b) shows a cut made to isolate events which deposit 25 keV equivalent x-ray energy (58 keV nuclear-recoils). The ear plot for electron-recoils is plainly seen (compare figure 4.2.3(c)) as is a set of data points which have larger phonon signal. These last events are the nuclear-recoil events. A similar plot with a cut near 8 keV (23 keV) electron-recoils (nuclear-recoils) is shown in figure 4.3.1(c). Although the

statistics are poor, it is possible that there are subtle ear plot shape differences (after accounting for the fact that a nuclear-recoil with the same ionization signal inherently has a larger phonon signal) for nuclear and electron-recoils which could indicate a phonon spectral difference for the two types of recoil. Recently, Ref. [35] has found a limit on the extra ballistic phonon production for nuclear-recoils compared to equal energy electron-recoils. The results given there are consistent with no extra ballistic component but the data allow a small increase in ballistic component for nuclear-recoils. The ballistic phonons participate in phonon focusing effects (phonon energy concentrated along the crystal's axes of symmetry) which affect the TES pulse height (typically resulting in smaller areas of film driven normal since the phonon energy is concentrated in a smaller area). It may be possible to exploit this phonon spectral difference to distinguish electron-recoils from nuclear-recoils using the a phonon sensor alone. Unfortunately, only a small fraction (few %) of the phonon energy is ballistic so discriminating the two types of recoil will be quite challenging.

CHAPTER 5: CHARGE COLLECTION AND TRAPPING AT LOW TEMPERATURE

We have seen in chapter 4 that the nuclear-recoil/electron-recoil discrimination technique requires that charge collection be reasonably good (~ 90%) at low applied electric field. The electric field is required to separate and drift (in opposite directions) the event induced free electrons and holes. The field must be low in magnitude in order to minimize the extra charge-drift induced phonon energy.

Unfortunately, charge collection efficiency drops rapidly at very low applied field, presumably due to charge trapping (see figure 3.4.4). Since the CDMS (Cryogenic Dark Matter Search) experiment will use detector substrates 1 cm thick, we need to be able to achieve good charge collection through 1 cm with only ~ 2 V/cm applied electric field. We therefore set out to study a variety of high-purity silicon detectors in order to understand the low-field trapping effects and their dependence on crystal purity.

In addition to confirming that good charge collection can be achieved through ~ 1 cm thick substrates, in silicon of sufficiently high purity, we found interesting and unexpected effects due to the initial electron-hole cloud surrounding the event location.

5.1 Electron Stopping in Si

When a photon of energy ~ few tens keV is photo-absorbed by an electron in a semiconductor like silicon, the resulting high energy electron excites, as it rapidly losses energy, a large number of other electron-hole pairs. The initial energy is cascaded down through several generations of electron-hole pairs until the excited free charge carriers fall below the threshold for further ionization production.

The stopping power (rate of energy loss per unit distance) in the silicon for the high energy electron is modeled in different energy ranges by different theories. For energies above ~ 10 keV the stopping power is dominated by electron-electron collisions and is described by the Bethe-Bloch theory [47]. From 10 keV down to ~ 10 eV energy loss is given by the complex dielectric function theory [48], and down to ~ 1 eV using the gap induced threshold [49]. Below E ~ 1 eV the charges cool first by optical phonon emission (down to ~ 60 meV) and then by acoustic phonon emission. At a threshold of ~ 0.2 meV (~ 2 K equivalent temperature) [50], corresponding to electron velocity equal to the speed of sound in silicon, the charges can no longer emit or absorb phonons. In a detector at T < 2 K the free charge carriers will presumably diffuse (limited by impurity scattering) after reaching this threshold. In high purity silicon, the elastic scattering

length for electrons off neutral impurities can be as large as ~ 100 μm, so charges can perhaps diffuse macroscopic distances before reaching the crystal temperature.

For 60 keV energy depositions in cold silicon at T ~ 2 K, the average total track length for the high-energy electron is ~ 35 μm. The secondary electrons and holes have energies ~ 100 eV and they will thermallize after moving ~ 10 nm. The average energy spent to create an electron-hole pair is ≈ 3.6 eV [49]. If the resulting electron-hole cloud is considered roughly spherical with radius ~ 15 μm then the charge density is $n \sim 10^{12}$ electron-hole pairs cm^{-3}. This density is roughly independent of deposited energy since for smaller energy depositions fewer charges will be found in a smaller volume. At low temperatures, this electron-hole cloud is dense enough to be considered a plasma. In other words, the Debye shielding length ($\lambda_D = 740(\varepsilon T_{eV}/n)^{1/2}$ cm ≈ 0.3 μm at 2 K [51]) is much smaller than the size of the cloud. It is possible, therefore, that the interior of the cloud is shielded temporarily from the applied electric field. The shielding will be temporary since the cloud will be eroded from its surface by the electric field.

The applied electric field in our detectors acts to pull this cloud apart and drift the different sign charges in opposite directions. Typical data sets, like figure 3.4.4, plot the position of the 60 keV peak in the ionization pulse height spectrum as a function of electric field. There are several possible ways that charges could be lost, causing the peak position to fall, in the cloud or during drift: (a) back-diffusion, where an electron or hole diffuses against the electric field and is collected by the "wrong" electrode, (b) charge loss out of the crystal for near surface events when energies are above the work function, (c) electron-hole recombination, and (d) trapping on impurities.

We will find in the next sections that the peak in an ionization pulse height spectrum comes from events near the center of the crystal thickness so (a) and (b), which are near-surface effects, should not be important in determining peak position.

Electron-hole recombination during drift should certainly be negligible since the different sign charges are drifting away from each other. Recombination within the initial cloud is also expected to be negligible in our high purity samples, where lifetimes on the order of 1 ms are found at room temperature. In addition, experiments with heavy fission fragments in high-purity detectors [52, 53] give much higher charge densities along the track ($n \sim 10^{22}$ cm^{-3}), leading to pronounced "plasma delays" in the ionization signal risetime, but recombination losses of ≤ 6% are deduced, which the authors consider anomalously large and they attribute to local crystal damage done by the heavy fragments. Alternatively, if the recombination loss in the fission fragment experiments is due to Auger recombination, the dominant band-to-band mechanism in silicon, then this effect should be completely negligible in our detectors since the Auger process depends

roughly on charge density as ~ n^3 [54]. Finally, Ref. [39] measured drift velocity in high-purity silicon as a function of electric field down to ~ 8 K. In those experiments, the charge density could be varied as high as ~ 10^{13} cm^{-3} and no effect due to electron-electron interactions was seen.

We are left, then with (d), charge trapping during drift or in the initial cloud, as the most likely charge loss mechanism. In what follows we will develop simple models of the charge loss due to trapping and compare them to a variety of data from our samples.

As a caution, it should be emphasized that although charge loss in the cloud due to recombination seems unlikely it is essentially indistinguishable experimentally from simple trapping.

5.2 Simple Trapping Model

The simplest model of charge loss in our detectors considers only trapping along the drift path. All of the free electrons and holes excited by a particle interaction start at a point in the crystal and they drift to opposite electrodes with a constant drift velocity. This model assumes that the charges are very quickly accelerated to their drift velocities. The charges will trap on a uniform density of impurities and each charge has the same chance to trap per unit drift length. The number of charges which trap while drifting a small distance dz in the direction of the electric field is given by

$$-dQ = \frac{Q}{\lambda} dz \tag{5.1}$$

where the factor λ, which is defined as a trapping length, contains the density of impurities (N_A, the density of acceptor impurities in p-type samples) and the cross section (σ) for trapping. The trapping length should scale as $\lambda \sim 1/\sigma N_A$ with σ decreasing for increasing applied electric field. Eqn. 5.1 is the simple exponential decay equation where the number of charges trapped is proportional to the number that are still moving. The drifting charge is therefore attenuated exponentially with drift distance:

$$Q = Q_0 e^{-z/\lambda} \tag{5.2}$$

where Q_0 is the initial number of charges created in the event.

If an amount Q of charge drifts a distance dz then, by eqn. 3.7, signal charge is induced on the electrodes of amount

$$dS = Q\frac{dz}{d} \tag{5.3}$$

where d is the thickness of the detector and S represents the signal charge. If Q_0 is deposited at position z_0 then eqn. 5.2 allows us to plot Q as a function of z, as in figure 5.2.1(a). In figure 5.2.1, the electrons drift against the direction of the electric field with trapping length $\lambda_e(E)$ and the holes drift along the electric field with trapping length $\lambda_h(E)$. It is expected that the trapping lengths will increase as the electric field increases. By combining eqn. 5.2 and 5.3 we find that for each dz we get a contribution to the signal

$$dS = Q_0 e^{-(z-z_0)/\lambda}\frac{dz}{d}. \tag{5.4}$$

The total signal will be the integral of eqn 5.4 over all z. Referring to figure 5.2.1, this is the same as saying that the signal is the area under the curve Q(z). Thus, the total normalized signal can be written as a function of event position as

$$\frac{S(z_0)}{Q_0} = \int_0^{z_0} e^{-(z_0-z)/\lambda_e}\frac{dz}{d} + \int_{z_0}^{d} e^{-(z-z_0)/\lambda_h}\frac{dz}{d} \tag{5.5}$$

which can easily be evaluated to obtain

$$\frac{S(z_0)}{Q_0} = \frac{\lambda_e}{d}(1 - e^{-z_0/\lambda_e}) + \frac{\lambda_h}{d}(1 - e^{-(d-z_0)/\lambda_h}). \tag{5.6}$$

Eqn 5.6 describes how the measured charge signal depends on event position through the thickness of the detector. Figure 5.2.1(b) and (c) demonstrate (for $\lambda_h \approx \lambda_e$) that for events near the edges of the detector the signal is smaller. For uniform illumination of the crystal (attenuation length for 60 keV photons in Si is ~ 3 cm), all event locations are equally probable and we can find the position which gives maximum signal

$$(z_0)_{max} = \frac{d}{1 + \lambda_h / \lambda_e}. \tag{5.7}$$

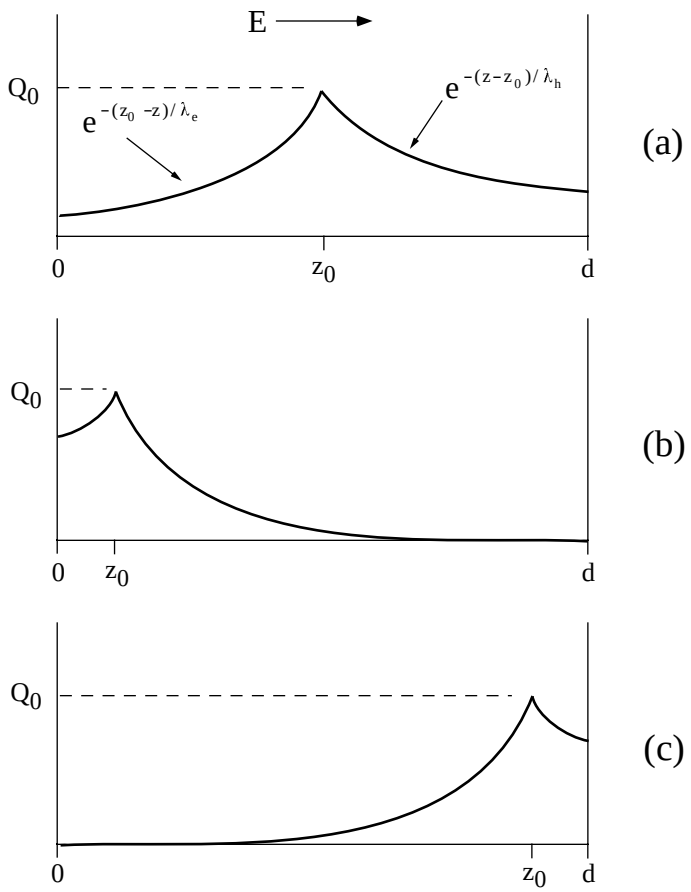

Figure 5.2.1 Simple Trapping Model. Electrons and holes drift through the detector under the influence of the electric field, E. A uniform density of traps causes exponential attenuation of the drifting charge. The signal is the area under the curves for (a) an event near the center of the detector, or (b) and (c) events near one side of the crystal. The largest signal is for events which occur near the center of the detector.

For $\lambda_h = \lambda_e$ the maximum signal occurs at $z_0 = d/2$. If λ_h (λ_e) >> λ_e (λ_h) then the maximum signal occurs at $z_0 = 0$ (d). By inserting eqn. 5.7 into eqn. 5.6 we obtain the maximum signal size, which corresponds to the peak in a pulse height spectrum. The events in the tail which lies below the peak (see figure 3.4.3) arise from the position dependence of eqn. 5.6. By making the electric field dependence of the trapping lengths explicit, we have an expression for how the spectral peak position varies with electric field:

$$\frac{S_{max}(E)}{Q_0} = \left(\frac{\lambda_e(E) + \lambda_h(E)}{d}\right)\left(1 - e^{-\frac{d}{\lambda_e(E)+\lambda_h(E)}}\right). \quad (5.8)$$

Finally, we can define a mean trapping length $2\lambda(E) \equiv \lambda_e(E) + \lambda_h(E)$ which when inserted in eqn. 5.8 gives the simplest form of normalized peak position as a function of electric field:

$$\frac{S_{max}(E)}{Q_0} = \frac{2\lambda(E)}{d}\left(1 - e^{-\frac{d}{2\lambda(E)}}\right). \quad (5.9)$$

Two general statements can be made with respect to eqn. 5.9. First, as the electric field is increased the trapping length also increases and therefore the signal increases. At large enough electric field the pulse height saturates and becomes flat, independent of applied field. This situation is obvious since clearly a larger trapping length, i.e. less trapping overall, leads to a larger signal and no more than the deposited amount of charge (in the absence of impact ionization) can be collected. It is advantageous, therefore, to have λ be as large as possible at the applied electric field of interest (~ 2 V/cm); since $\lambda \sim 1/N_A$ a crystal with N_A as small as possible (highest purity) is desirable.

Second, eqn. 5.9 shows that for the same bulk semiconductor material (same N_A and same σ), a detector which is thicker (d larger) will give worse charge signal. Thus, we have an explicit prediction for how the charge pulse height should depend on detector thickness for detectors made from nominally the same starting material.

5.3 Experimental Survey of Si Samples

A variety of high-purity, p-type, <100> silicon samples were studied for charge collection at low electric field and low temperature. The samples are about 1 cm x 1 cm and vary in thickness from 300 μm to nearly 5 mm. Thin (~ 400 Å thick) Ti electrodes were deposited on each face of the samples using the procedure outlined in section 3.3.1. For each of the three highest resistivity samples (room temperature resistivity of 8 kΩ-cm, 15 kΩ-cm, and 40 kΩ-cm) two different thicknesses were fabricated from the same bulk material, typically ~ 2 mm and ~ 5 mm, in order to test the sample thickness dependence of charge trapping models. For the lowest resistivity samples, room temperature resistivity of 2 kΩ-cm, three thicknesses were examined: 300 μm, 1 mm, and 2 mm. All the crystals we used were grown specifically for high purity, either by

magnetic-Czochralski or float-zone techniques. In fact, the 40 kΩ-cm samples were grown using a combination Czochralski-CVD-Float zone technique which achieves impurity densities limited by the gas supply in the CVD step. The important point here is that the high resistivity of the samples is not achieved by intentional compensation so higher resistivity implies higher purity. Compensation of the semiconductor ($N_A \approx N_D$) can give very high resistivity in a fairly un-pure crystal. For the 2 kΩ-cm samples $N_A \sim 10^{13}$ cm^{-3} and for the higher resistivity samples $N_A \sim 10^{12}$ cm^{-3}.

The detectors were characterized by exposure to the same set of electron-recoil energies as was used in chapter 4: 60 keV, and 25 keV. The results were virtually identical for these two energies and in what follows only the 60 keV data will be discussed. The experiments consisted of measuring ionization pulse height spectra in both detector modes at different applied electric fields. The results are presented in the form of peak position (relative to full charge collection) as a function of electric field. It was not possible in the thicker samples (d > 2 mm) to apply a large enough electric field to saturate the ionization pulse height. In other words, we could not reach the flat, asymptotic region of pulse height versus electric field. The pulse heights were normalized to an extrapolated maximum signal by fitting the data to a smooth curve. This procedure, in which all data sets were treated equally, introduces a common-mode uncertainty in the normalized pulse height values of ~ 20% depending on how the extrapolation is done. This common-mode uncertainty does not affect any of the conclusions drawn from the relative positions of the various data sets.

5.3.1 Mode 2 data

First we will discuss the charge collection experiments in mode 2. Remember that here the detector performance is much improved compared to mode 1 (see figure 3.4.4) and trapping is presumably due to neutral impurities (impurity density $\approx N_A$). Data for the three highest purity samples are presented together in figure 5.3.1. The general trend of better charge collection for the higher purity samples is seen. For clarity the data are also presented separately in figures 5.3.2 - 5.3.4. Figure 5.3.2 shows typical error bars which represent the FWHM of the 60 keV ionization peak. Since these error bars clutter up the plot, and they are roughly the same from sample to sample, they will be omitted in the other plots. Estimated error bars in any of the experiments can be found by referring to figure 5.3.2. Most notable in figures 5.3.2 - 5.3.4 is a complete lack of thickness dependence for each of the three purities. In stark contrast to eqn. 5.9 the data show that

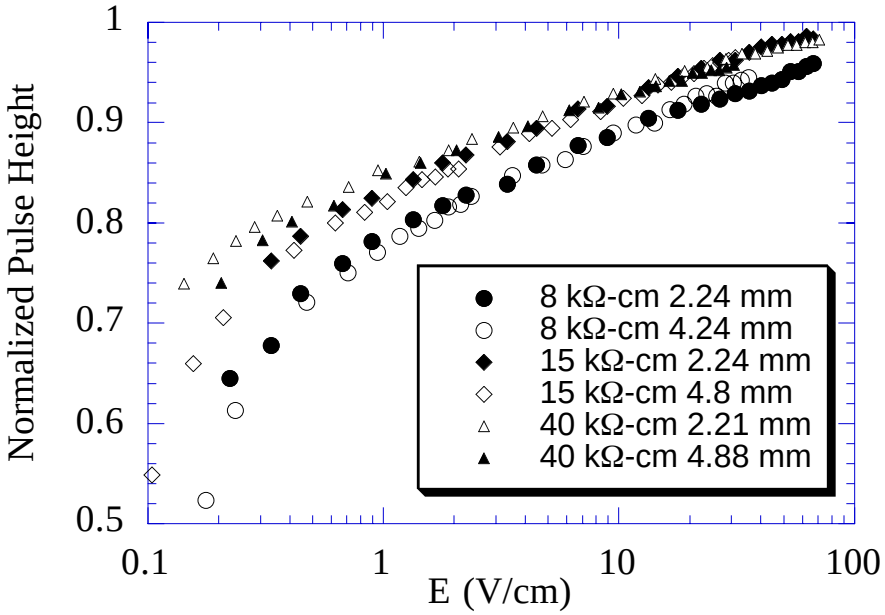

Figure 5.3.1 Normalized pulse height data for high-purity samples in Mode 2.

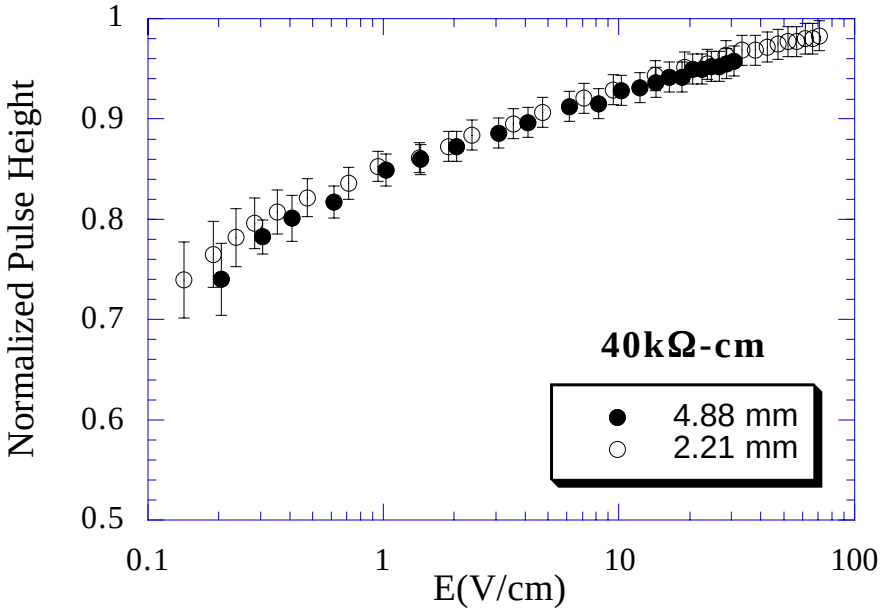

Figure 5.3.2 Normalized pulse height data for 40 kΩ-cm samples in Mode 2.

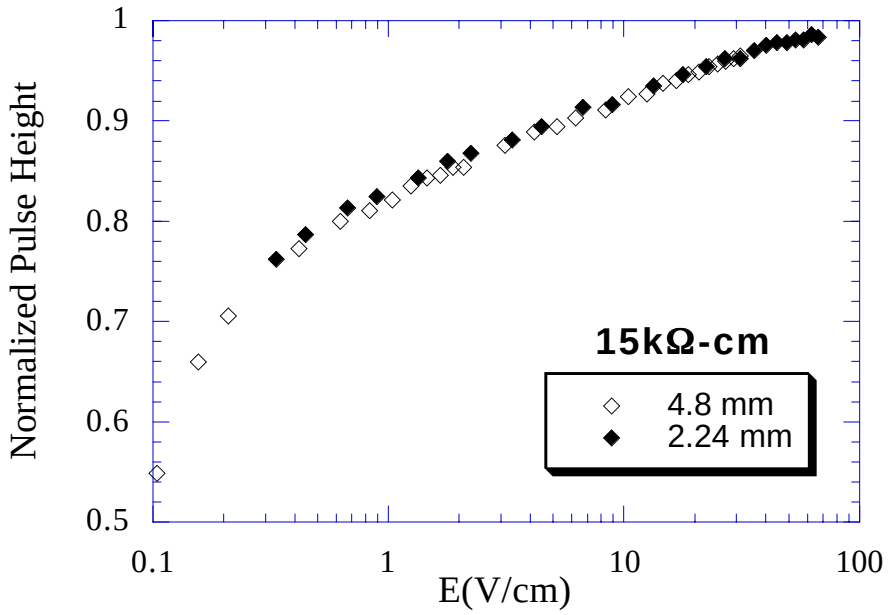

Figure 5.3.3 Normalized pulse height data for 15 kΩ-cm samples in Mode 2.

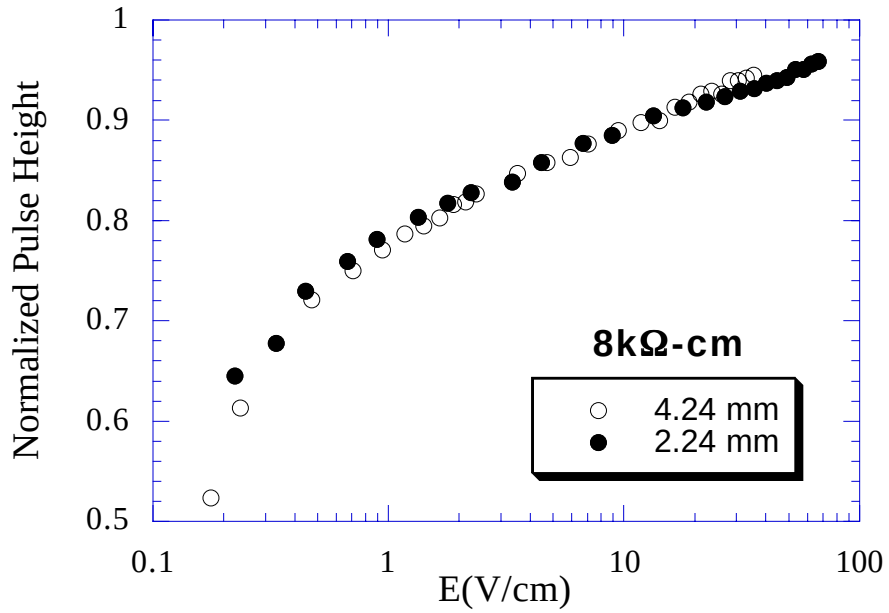

Figure 5.3.4 Normalized pulse height data for 8 kΩ-cm samples in Mode 2.

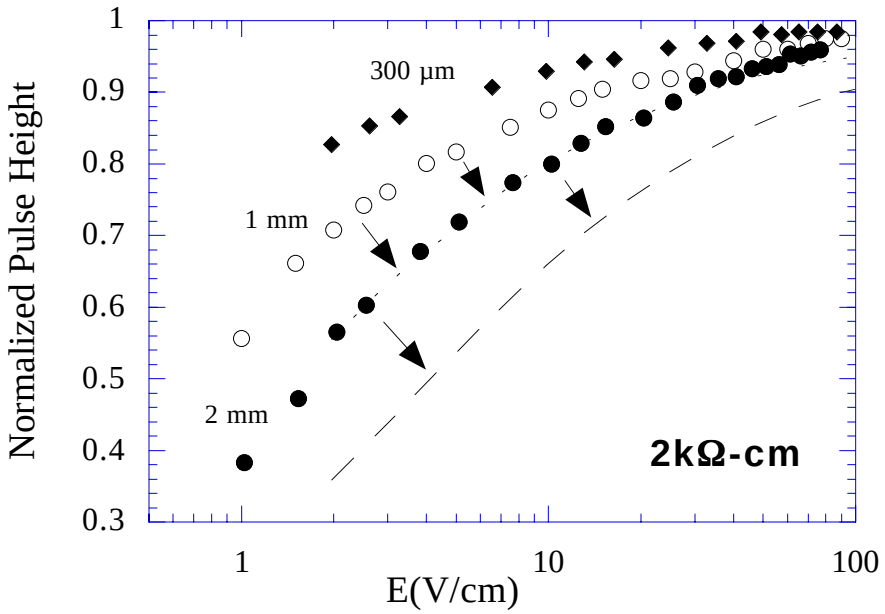

Figure 5.3.5 Normalized pulse height data for 2 kΩ-cm samples in Mode 2 showing predictions of the simple trapping model. Dashed lines indicate where 1 mm and 2 mm data would lie (relative to the 300 μm data) if trapping only occurred during drift.

the charge collection efficiency is the same for detectors ~ 2 mm thick and ~ 5 mm thick. Clearly, something is wrong with the model of section 5.2.

Data for the lowest purity samples (2 kΩ-cm) are shown in figure 5.3.5. Here there is a clear thickness dependence with the thicker detectors giving lower charge signal

at the same electric field. Each data point (normalized pulse height = S_{max}/Q_0) in the top data set in the figure (300 μm) can, using eqn. 5.9, be converted into a λ(E). The simple trapping model predicts that the deduced set of points λ(E) will be the same for all three thicknesses. This can be tested by taking the 300 μm set of λ(E) and replotting them as eqn. 5.9 but using d = 1 mm and d = 2 mm. The results of this test are shown as dashed lines in figure 5.3.5. Once again we find that the simple trapping model does not explain the data. In this case the data do show some thickness dependence but to a lesser degree than that predicted by eqn. 5.9.

5.3.2 Mode 1 data

A similar analysis can be made to test the simple trapping model in mode 1, where trapping is dominated by ionized impurity processes (density of ionized impurities $\approx N_D$). The procedure is the same as that described above. The thin sample normalized pulse height data are converted to $\lambda(E)$ and then replotted using eqn. 5.9 with the thickness of the thicker sample and compared to the thicker sample data. The results are shown for the three highest purity samples in figures 5.3.6 - 5.3.8 with the dashed lines indicating the predictions of eqn. 5.9. The thicker samples do show worse charge collection compared to the thinner samples but, again, not as much as that predicted by eqn. 5.9.

5.3.3 Charge coincidence experiments

The inability of the simple trapping model to account for the thickness dependence of the data in the charge collection experiments led us to suppose that the charge loss could be occurring, at least partially, in a small region close to the interaction location. If all the charge loss occurs in this "source region," which is smaller than the detector thickness, then the charge collection efficiency should not depend on thickness. This is precisely what the data say in figures 5.3.2 - 5.3.4. On the other hand, if the charge loss is partially in the source region (same for all thicknesses) and partially along the drift (more for thicker detectors), then the data will behave roughly as shown in figure 5.3.5. We suppose that the "source region" is the initial electron-hole cloud which is formed by a particle interaction.

In order to measure the size of the "source region," we instrumented a detector (40 kΩ-cm, 4.88 mm thick) with one electrode split in half as shown in figure 5.3.9(a). The top electrodes are now about 1 cm x 5 mm with $\approx$ 0.3 mm gap between them. The experiment pictures the cloud as expanding to some radius before being pulled apart by the electric field. In our setup, then, we can correlate the size of the cloud transverse to the electric field to the partitioning of charge between the two top electrodes. If the cloud occurs beneath the split in the electrodes then the charge signal will be shared by the two electrodes. If the cloud occurs away from the split then only one electrode will collect a signal. In the simplest analysis we can think of the cloud as a sphere of radius a(E) with uniform charge density. The detector will see coincident charge pulses if the event occurs within a distance a(E) of the split (see figure 5.3.9(b)). If the event occurs further from the split then a pulse will be seen on only one electrode. A cut can be made on the

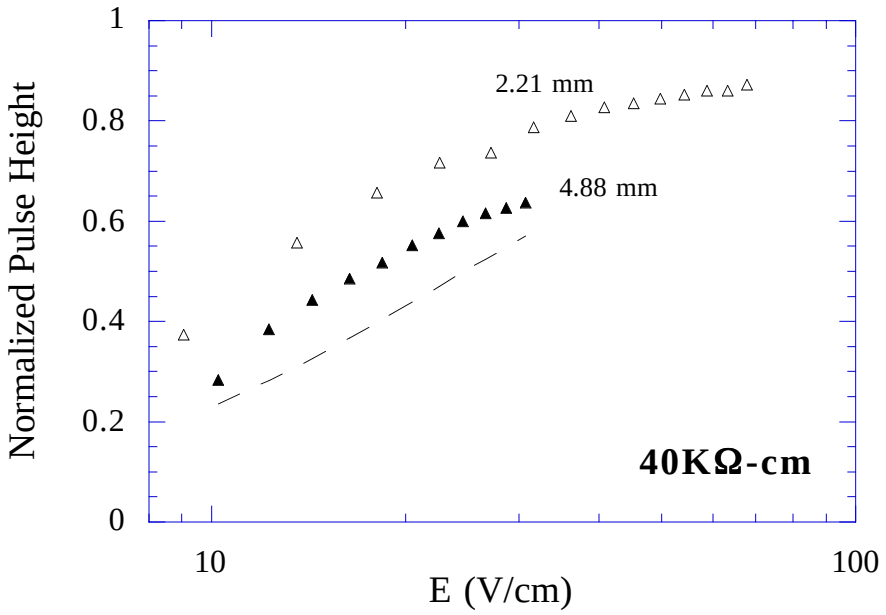

Figure 5.3.6 Normalized pulse height data for 40 kΩ-cm samples in Mode 1. The dashed line indicates the thicker sample prediction of the simple trapping model.

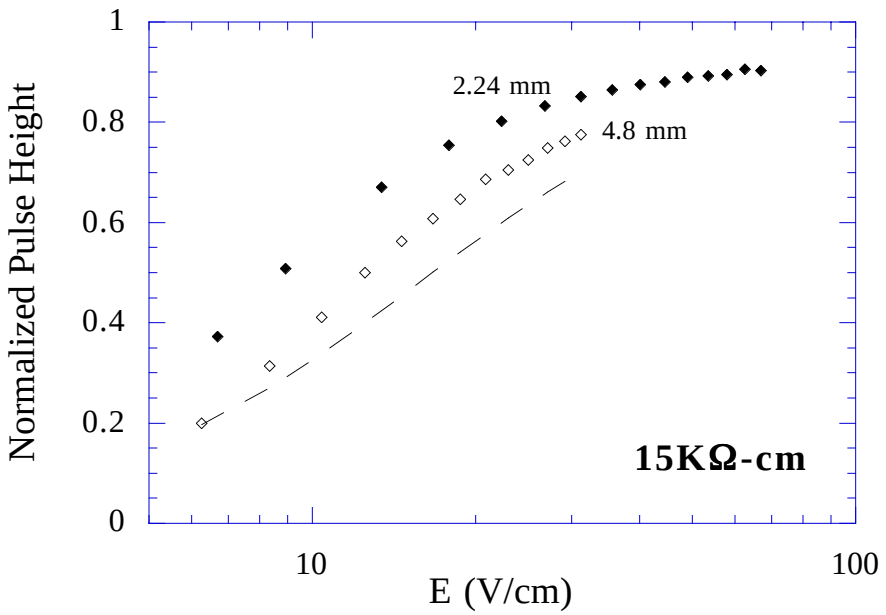

Figure 5.3.7 Normalized pulse height data for 15 kΩ-cm samples in Mode 1. The dashed line indicates the thicker sample prediction of the simple trapping model.

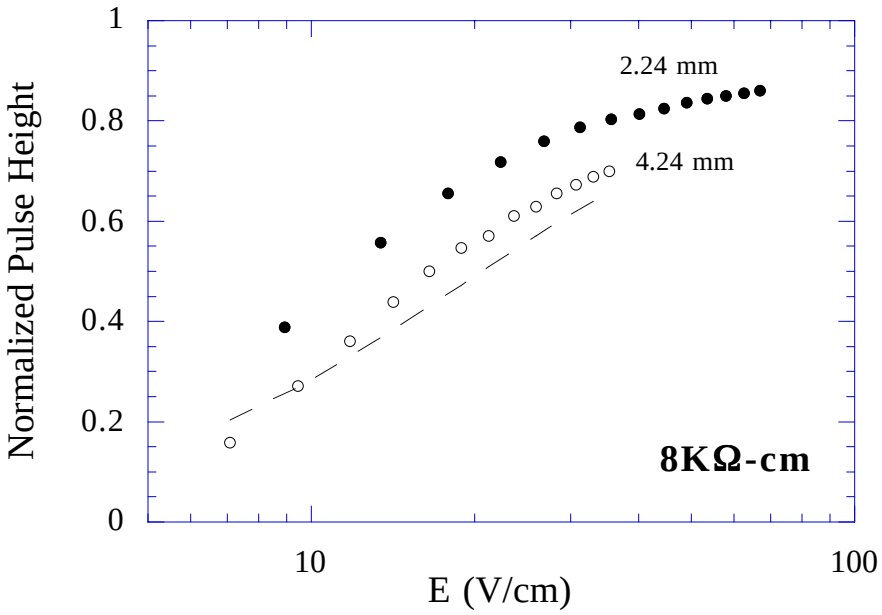

Figure 5.3.8 Normalized pulse height data for 8 kΩ-cm samples in Mode 1. The dashed line indicates the thicker sample prediction of the simple trapping model.

data to assure that a total of 60 keV of energy is collected. This requirement is a constraint on the sum of the output of the two amplifier channels.

The ratio, R, of the rate of coincident pulses to the rate of single pulses, for uniform illumination of the detector with 60 keV photons, tells us the diameter of the spherical charge cloud in this simple model. We can write the expression, with w = detector width,

$$R = \frac{2a(E)}{w - 2a(E)}. \tag{5.10}$$

This expression can be rewritten to extract a(E):

$$2a(E) = w\frac{R}{1+R} \tag{5.11}$$

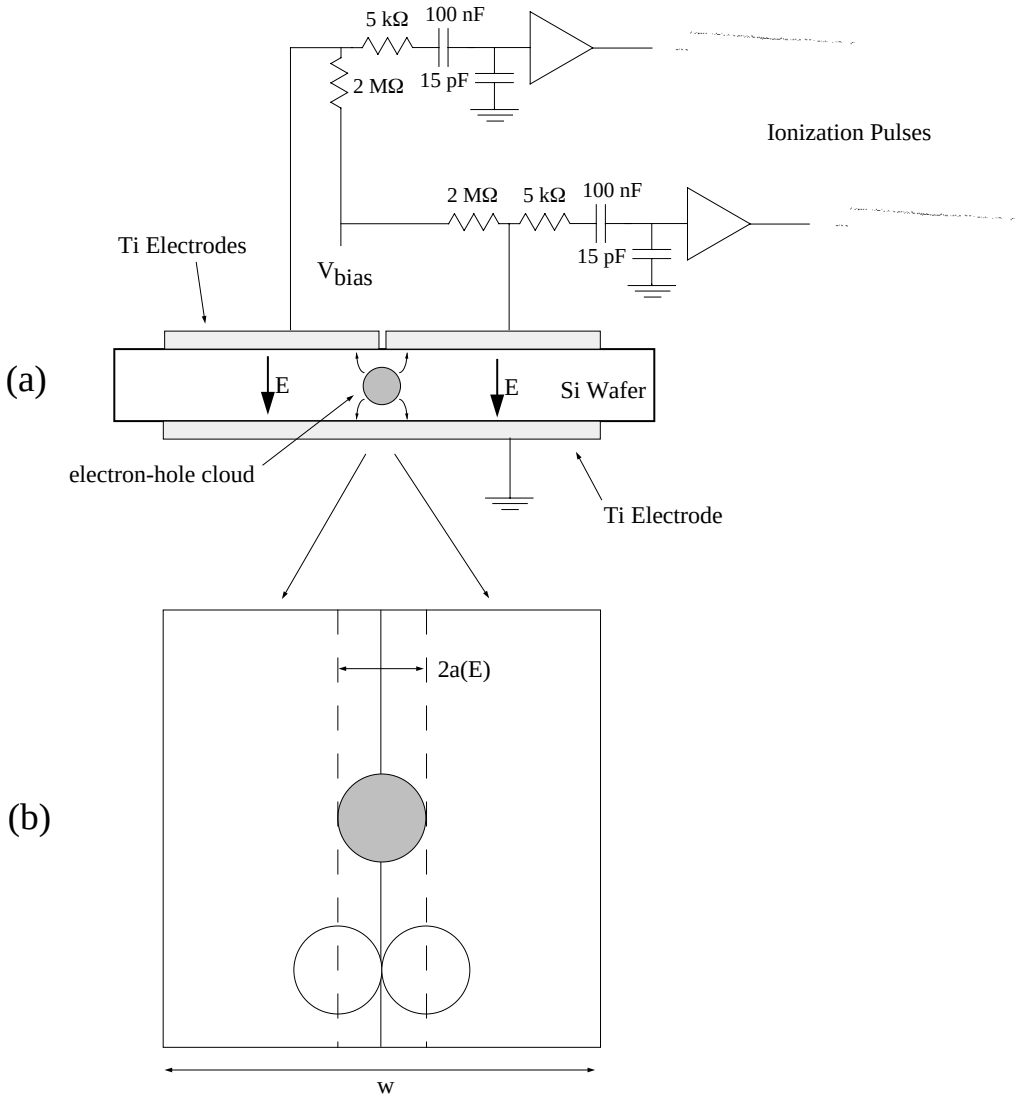

Figure 5.3.9 (a) Schematic diagram of detector for the simultaneous ionization experiment. The top electrode is split in half to measure the lateral size of the electron-hole cloud. (b) Expanded view from above. A fraction 2a(E)/(w-2a(E)) of the ionization pulses (events which occur within the dashed lines) will give signal in both amplifier channels for uniform illumination of the crystal.

The rate of coincidences, then, should give a rough measure of the size of the cloud. The cloud is not exactly spherical with uniform density so we should use eqn. 5.11 as a rough guide only.

Data were collected with the split electrode set up at different electric fields and the rate of coincidences was found to rise with decreasing applied field. The results are

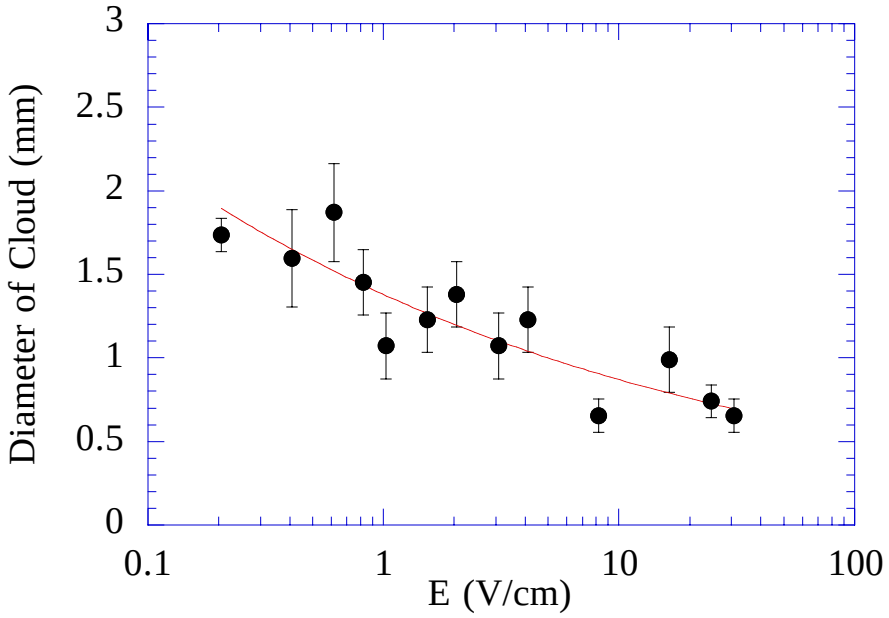

Figure 5.3.10 Rate of coincident ionization pulses converted to cloud diameter using eqn. 5.11. The smooth curve is a two parameter fit described in the text.

shown in figure 5.3.10. The statistics in the experiment are poor and the error bars shown in the figure are entirely statistical. A two parameter fit to the data is also shown in figure 5.3.10. The fit indicates that $2a(E) = (1.4 \pm 0.05)\, E^{(-0.19 \pm 0.03)}$ mm for E in V/cm. Thus, the data indicate that a large, ≈ 1 mm charge cloud is present at low electric fields. The scale of this cloud is much larger than that predicted by the stopping power calculations in section 5.1 (diameter ~ 35 μm). We suspect that the large cloud is due to the threshold for phonon emission at electron energy ~ 0.2 meV. Upon reaching this energy, the electrons diffuse against impurities and can reach macroscopic distances in high-purity crystals.

Accidental coincidences could occur, giving a field-independent rate, if a 60 keV photon Compton scatters in one half of the detector and then is photo-absorbed in the other half. The detector would, in this case, still measure a total (summed) pulse height of 60 keV. An estimate of the rate of such contaminating events gave a low rate smaller than the error bars shown in figure 5.3.10 so this background source can be neglected. In addition, the rate of coincidences could be affected by drift induced transverse spreading of the charges. This effect, which is calculated [55] to be nearly independent

of applied electric field, is found to give a coincidence rate at least a factor of four lower than what we measured. Thus, a more detailed analysis than that given above should include this effect but it is of secondary importance since by itself it cannot account for the magnitude and electric field dependence of the data.

5.4 Analysis of Charge Collection Data

We are now in a position to modify the simple trapping model presented in section 5.2. Although the model is plausible it clearly fails to explain the thickness dependence of every sample in both mode 1 and mode 2. In addition, we know that there is a macroscopic charge cloud which must be influencing the charge measurements.

5.4.1 Mode 2 (high-purity samples)

The data in figures 5.3.2 - 5.3.4 show no thickness dependence at all. This implies that all of the charge loss is occurring in the charge cloud with no further loss due to trapping along the drift after the electric field penetrates the cloud. The simplest model of this situation is one of diffusion in a field-free region near the event location which is shielded temporarily from the applied electric field by the electron-hole plasma. Each charge executes a random walk in three dimensions, independent of the others, with a constant step length (λ_{step}) and a constant trapping length (λ_{trap}) which both are determined by the density of impurities and the relevant cross sections for elastic scattering and trapping. Let each charge diffuse from the event location to some radius a(E) where it comes under the influence of the electric field. This a(E) will represent the maximum radius of the charge cloud before it is destroyed by the electric field. For N steps, where N is much greater than one, the position distribution function for each charge is a gaussian with [56]

$$\sigma^2 = \frac{N}{3}\lambda_{step}^2. \tag{5.12}$$

The total distance traveled in N steps is $x = N\lambda_{step}$. Thus, we can rewrite eqn. 5.12 and, setting $\sigma = a(E)$, we find

$$x = \frac{3a^2(E)}{\lambda_{step}}. \tag{5.13}$$

Since the charges trap with trapping length λ_{trap} we find that the fraction of charges which escape the cloud can be expressed as

$$\frac{Q}{Q_0} = e^{-x/\lambda_{trap}} = e^{-3a^2(E)/\lambda_{step}\lambda_{trap}}. \qquad (5.14)$$

Thus we have a very simple model of charges diffusing in the cloud, some fraction of them trapping in the process, before the remainder are drifted to the detector electrodes without further attenuation. The model clearly does not contain the actual dynamics of the situation, which include erosion of the cloud from its surface as it expands and the fact that a larger fraction of the charges in the cloud are affected by the electric field as its density decreases with expansion (λ_D increases and shielding is less effective). In addition, the actual step and trapping lengths will not be constants and the electrons and holes will need to be treated separately. As a simple, zeroeth-order model, however, it contains the necessary features which are required by the data: a plausible mechanism by which the interior of the cloud is temporarily shielded from the electric field, and a means by which charges can trap before leaving the cloud.

In order to estimate how the maximum radius of the cloud will depend on applied electric field we can consider the problem of a conducting, metal sphere in a uniform electric field. The total amount of charge available for shielding is spread over a sphere of radius a and it can cancel the applied field within the sphere. The charge is held on the sphere by the work function of the metal. The amount of charge of each sign required to shield an applied field E_a is $Q \sim E_a a^2$. Thus, for a given amount of available charge created in an event, a will scale as $E_a^{-1/2}$. The electron-hole cloud is not a conducting sphere, however, since the charges diffuse away from each other and since it is pulled apart by the applied field. If λ_{step} is quite small, then the plasma is more strongly confined at early times near the event location and its behavior will more closely resemble the conducting sphere; for λ_{step} larger, the plasma will behave less like a conducting sphere.

The data for the highest purity samples are shown, with fits to eqn. 5.14, in figures 5.4.1 - 5.4.3. The fits have somewhat more curvature than the data but, given the simplicity of the model and the error bars in figure 5.3.2, they are satisfactory. In the fits we set $a(E) = b\,E^{-n}$ cm for E in V/cm and fit to the parameters $3b^2/\lambda_{step}\lambda_{trap}$ and n. The results are shown in table 5.1. Remarkably, the fits require $a(E) \sim E^{-0.2}$ cm, the same result found in our coincident charge measurements. Also, the coincident charge

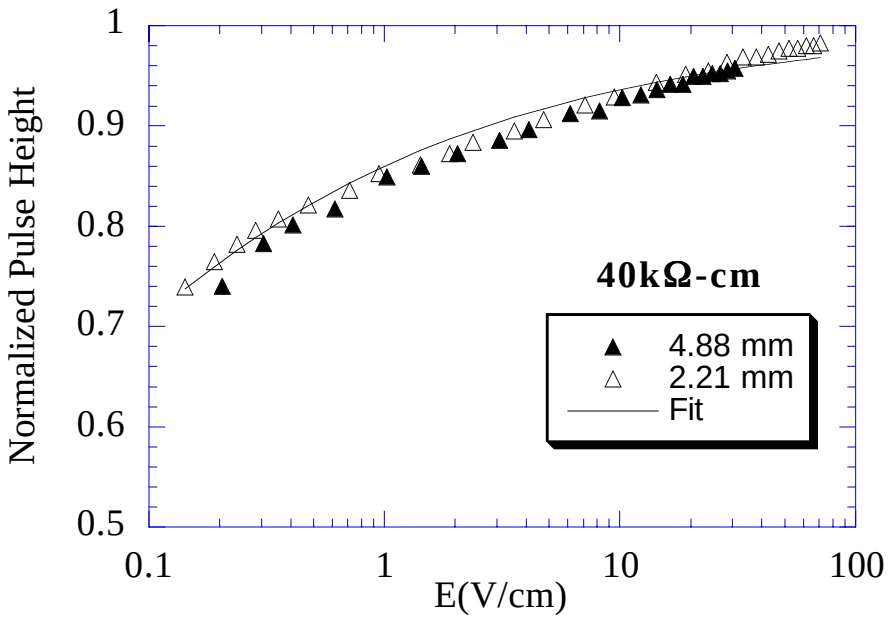

Figure 5.4.1 Pulse height data for 40 kΩ-cm samples in Mode 2 showing fit to eqn. 5.14. The parameters of the fit are shown in Table 5.1.

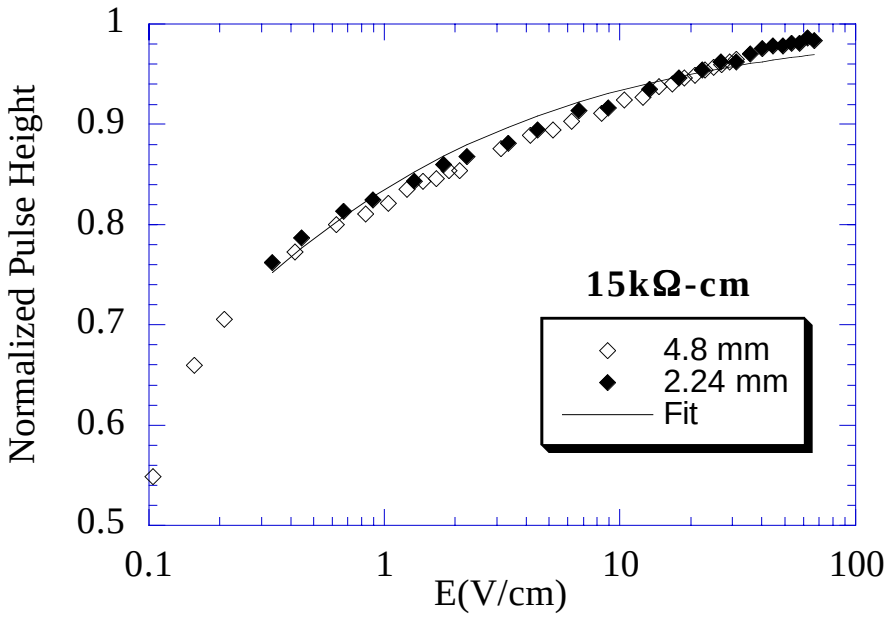

Figure 5.4.2 Pulse height data for 15 kΩ-cm samples in Mode 2 showing fit to eqn. 5.14. The parameters of the fit are shown in Table 5.1.

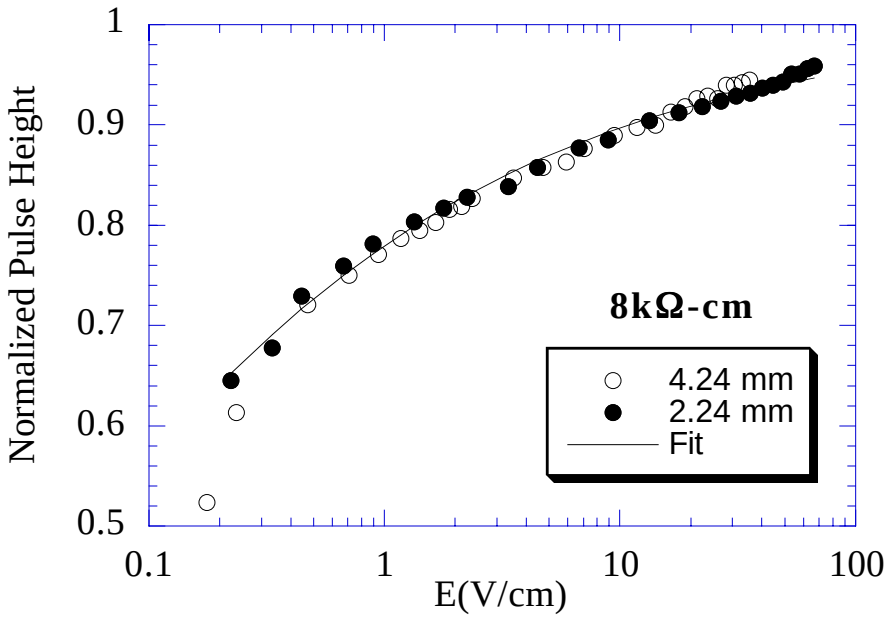

Figure 5.4.3 Pulse height data for 8 kΩ-cm samples in Mode 2 showing fit to eqn. 5.14. The parameters of the fit are shown in Table 5.1.

measurements give an independent measure of the parameter b for the 40 kΩ-cm sample, namely $b \approx 0.07$ cm. This allows us to estimate the values of λ_{step} and λ_{trap} in these detectors. Since $3b^2/\lambda_{step}\lambda_{trap} \approx 0.15$ and $a \approx 0.07$ cm we get $\lambda_{step}\lambda_{trap} \approx 0.1$ cm^2. These numbers are consistent with estimates from the cross sections and impurity density ($N_A \sim 10^{12}$ cm^{-3}, $\sigma \sim 10^{-10}$ cm^2 for elastic scattering and $\sigma \sim 10^{-13}$ cm^2 for trapping [30, 32]) which give $\lambda_{step} \sim 0.01$ cm and $\lambda_{trap} \sim 10$ cm. The parameter $3b^2/\lambda_{step}\lambda_{trap}$ is slightly higher in the 15 kΩ-cm and 8 kΩ-cm detectors indicating a higher impurity density which will make λ_{step}, and λ_{trap} smaller.

5.4.2 Mode 2 (MagCZ sample)

For the 2 kΩ-cm samples we need a model which includes the charge loss in the cloud plus loss during drift (see figure 5.3.5). This is a straightforward extension of the simple trapping model. Figure 5.4.4, in analogy to figure 5.2.1, shows the situation. The charge which survives the cloud is separated by the diameter of the cloud. No signal is derived from within the cloud since both electrons and holes are presumed to diffuse

Sample	$\frac{3b^2}{\lambda_{step}\lambda_{trap}}$	n
40 kΩ-cm	0.151 ± 0.002	0.18 ± 0.01
15 kΩ-cm	0.180 ± 0.004	0.21 ± 0.03
8 kΩ-cm	0.249 ± 0.003	0.18 ± 0.01

Table 5.1 Parameters used in the charge cloud fits to eqn. 5.14 shown in figures 5.4.1 - 5.4.3.

uniformly and only a net separation of charge gives signal. The problem is reduced to one dimension and the fact that the cloud is at least roughly spherical is neglected: all the surviving charge is assumed to separate to the diameter of the cloud. Following section 5.2 the total signal is given by the area under the curve shown in figure 5.4.4. This area is expressed, with Q' = charge which survives the cloud (eqn. 5.14), as

$$\frac{S(z_0,a)}{Q_0} = Q'\{\frac{2a}{d} + \int_0^{z_0-a} e^{-((z_0-a)-z)/\lambda_e}\frac{dz}{d} + \int_{z_0+a}^{d} e^{-(z-(z_0+a))/\lambda_h}\frac{dz}{d}\}. \qquad (5.15)$$

After evaluating the integrals in eqn. 5.15, we obtain

$$\frac{S(z_0,a)}{Q_0} = Q'\{\frac{2a}{d} + \frac{\lambda_e}{d}(1 - e^{-(z_0-a)/\lambda_e}) + \frac{\lambda_h}{d}(1 - e^{-(d-(z_0+a))/\lambda_h})\}. \qquad (5.16)$$

We can again find the value of z_0 which gives the maximum signal since we are trying to model the position of the peak in the spectrum. The maximum signal occurs for

$$(z_0)_{max} = a(\frac{\lambda_h - \lambda_e}{\lambda_h + \lambda_e}) + \frac{d}{1 + \lambda_h/\lambda_e}. \qquad (5.17)$$

If a = 0 then we recover eqn. 5.7. If λ_h (λ_e) >> λ_e (λ_h) then the maximum signal occurs at z_0 = a (z_0 = d - a). If $\lambda_h \approx \lambda_e$ then the maximum signal occurs near z_0 = d/2. Inserting eqn. 5.17 into eqn. 5.16 we obtain

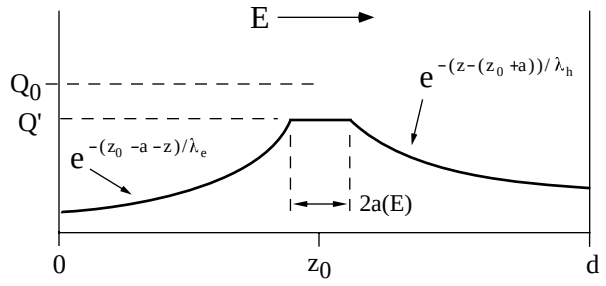

Figure 5.4.4 Hybrid Trapping Model. Electron-hole cloud of radius a(E) shields its interior from the applied electric field. A fraction, Q', of the charge generated in an event does not trap in the cloud and it drifts to the electrodes. The trapping during drift is expressed by the exponentials. The measured signal is the area under the curve.

$$\frac{S_{max}(a)}{Q_0} = Q'\{\frac{2a}{d} + (\frac{\lambda_h + \lambda_e}{d})(1 - e^{-\frac{(d-2a)}{(\lambda_h+\lambda_e)}})\} \qquad (5.18)$$

as the maximum signal pulse height in the hybrid model. Making the electric field dependence explicit, defining the mean trapping length $2\lambda(E) \equiv \lambda_e(E) + \lambda_h(E)$, and using eqn. 5.14 for Q' we arrive at the final expression of the model:

$$\frac{S_{max}(E)}{Q_0} = e^{-\frac{3a^2(E)}{\lambda_{step}\lambda_{trap}}}\{\frac{2a(E)}{d} + \frac{2\lambda(E)}{d}(1 - e^{-\frac{(d-2a(E))}{2\lambda(E)}})\}. \qquad (5.19)$$

The pre-factor outside the brackets represents the charge loss in the diffuse cloud. The first term in the brackets is the signal from the surviving charge separated to the diameter of the cloud and the second term in the brackets represents the signal due to trapping during drift (compare to eqn. 5.9). Eqn. 5.19 predicts the position of the peak in the ionization pulse height spectrum, in this hybrid model, as a function of applied electric field and the detector thickness.

The hybrid model can be applied to the 2 kΩ-cm data. The model requires a five parameter fit to the data for each detector thickness: for $a(E) = b\,E^{-n}$ cm, $\lambda(E) = c\,E^{m}$ cm, and $3b^2/\lambda_{step}\lambda_{trap}$ we need to specify five parameters. The set of these five parameters which fit the data for all three thicknesses is given in table 5.2. The estimated

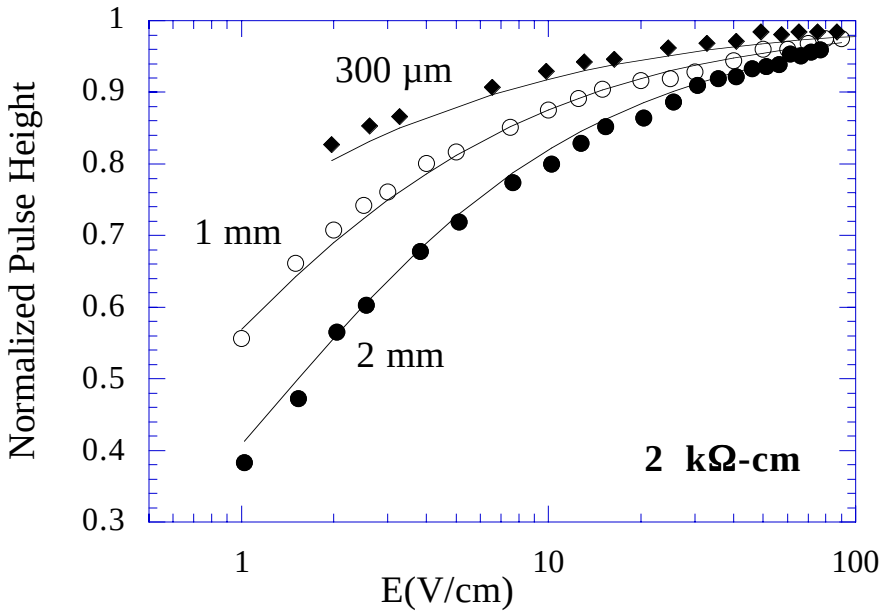

Figure 5.4.5 Pulse height data for 2 kΩ-cm samples in Mode 2 showing the fit to eqn. 5.19 (hybrid trapping model). The parameters of the fit are given in Table 5.2.

uncertainties listed in the table were found by varying each parameter in the fit separately. The fits from eqn. 5.19, using the parameters in table 5.2, are shown in figure 5.4.5 for the 2 kΩ-cm samples.

In the 2 kΩ-cm samples the impurity density $N_A \sim 10^{13}$ cm^{-3}. From this density we can estimate $\lambda_{step} \sim 10$ µm and $\lambda_{trap} \sim 1$ cm. The fit implies that $b \approx 0.01$ cm and $n \approx 0.3$. (b is smaller than in the higher purity samples, in agreement with the expectation that the charge cloud will not be able to expand as much in the lower purity samples. Also, $n \approx 0.3$ is consistent with the more confined plasma behaving more like a conducting sphere compared to the higher purity samples where $n \approx 0.2$.) If $3b^2/\lambda_{step}\lambda_{trap} \approx 0.3$ then $\lambda_{step}\lambda_{trap} \approx 0.001$, which is consistent with our estimates above. The fit also gives us $\lambda(E) \approx 0.055\ E^{0.8}$ cm for E in V/cm. This is reasonable since the applied electric field is analogous to a raised temperature for the drifting electrons and holes ($T_{electron} \sim E$). The trapping cross section should scale as T^{-1} at low temperature [31] so, by analogy, the trapping length should scale $\lambda \sim E$.

Sample	$\frac{3b^2}{\lambda_{step}\lambda_{trap}}$	b	n	c	m
2 kΩ-cm	0.30 ± 0.05	0.010 ± 0.005	0.30 ± 0.02	0.055 ± 0.005	0.80 ± 0.03
40 kΩ-cm	3.0 ± 0.2	0.005 ± 0.003	0.5 ± 0.02	0.01 ± 0.002	1.00 ± 0.02
15 kΩ-cm	3.0 ± 0.2	0.005 ± 0.003	0.5 ± 0.02	0.02 ± 0.002	1.00 ± 0.02
8 kΩ-cm	3.0 ± 0.2	0.005 ± 0.003	0.5 ± 0.02	0.01 ± 0.002	1.00 ± 0.02

Table 5.2 Parameters used in the hybrid trapping model fits to eqn. 5.19 shown in figures 5.4.5 - 5.4.8. The fits are for Mode 2 for the 2 kΩ-cm samples and for Mode 1 for the higher purity samples.

5.4.3 Mode 1

The hybrid trapping model can also be applied to the mode 1 data shown in section 5.3.2. For mode 1 the trapping processes are dominated by ionized impurities and thus they are expected to be stronger in magnitude. The relevant cross sections are estimated to be $\sigma \sim 10^{-8}$ cm^2 for elastic scattering and $\sigma \sim 10^{-11}$ cm^2 for trapping in the absence of an electric field. For impurity densities of $N \sim 10^{12}$ cm^{-3} we can estimate $\lambda_{step} \sim 1$ μm and $\lambda_{trap} \sim 1$ mm. The mode 1 data with the hybrid model fits are shown in figures 5.4.6 - 5.4.8. The parameters for these fits are given in table 5.2. The parameters tell us that the scale of the charge cloud (parameter b) is much smaller and that its size varies as $\sim E^{-0.5}$. Both effects are consistent with our previous idea of the charge cloud. Trapping during the drift is also stronger than in mode 2. Interestingly, the 15 kΩ-cm sample gives a longer trapping length (parameter c) than the 40 kΩ-cm sample. This makes sense, however, considering the fact that the 15 kΩ-cm sample took less time, at the same exposure rate, to change modes. The time it takes to neutralize all the ionized impurities (change modes) is proportional to the number of minority impurities and it is the density of minority impurities which determines the mode 1 detector behavior (see section 3.2.4). Figure 5.4.9 shows the ionization peak position time profile showing the mode shift.

The parameters of the fits give consistent results. Taking $b \approx 0.005$ cm and $3b^2/\lambda_{step}\lambda_{trap} \approx 3$ we obtain $\lambda_{step}\lambda_{trap} \approx 10^{-5}$ cm^2 which is in agreement with our simple estimates above. Also, we now have $\lambda \sim T^{-1} \sim E$ as expected for trapping on ionized impurities [31].

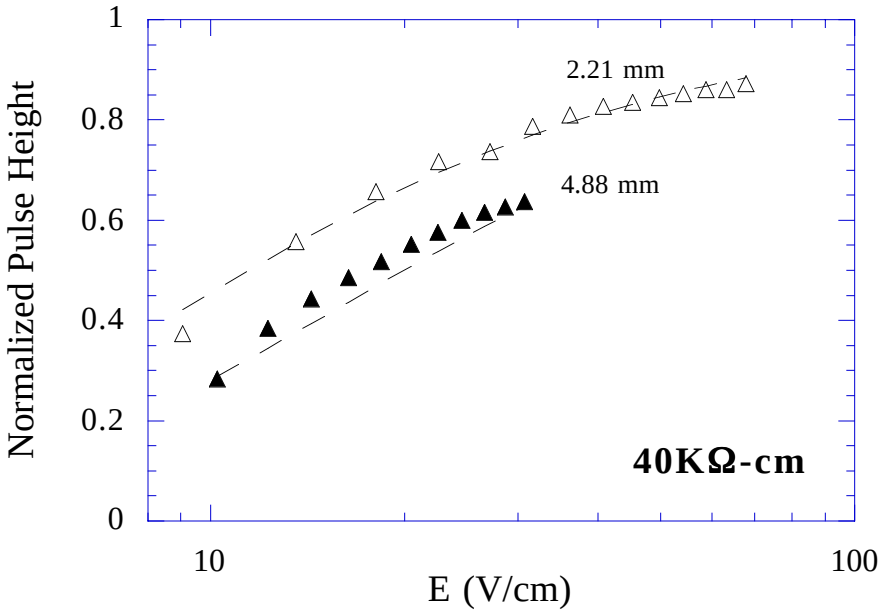

Figure 5.4.6 Pulse height data for 40 kΩ-cm samples in Mode 1 showing the fit to eqn. 5.19 (hybrid trapping model). The parameters of the fit are given in Table 5.2.

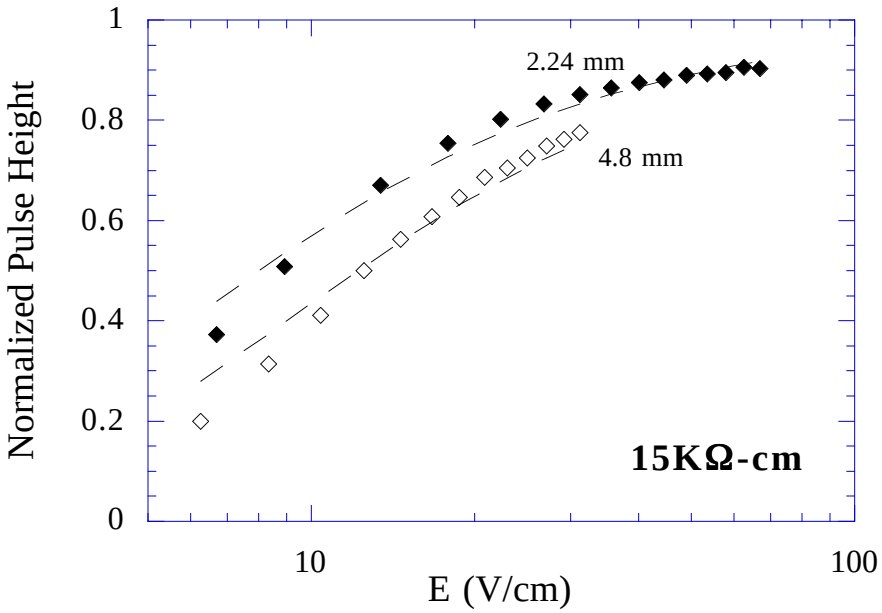

Figure 5.4.7 Pulse height data for 15 kΩ-cm samples in Mode 1 showing the fit to eqn. 5.19 (hybrid trapping model). The parameters of the fit are given in Table 5.2.

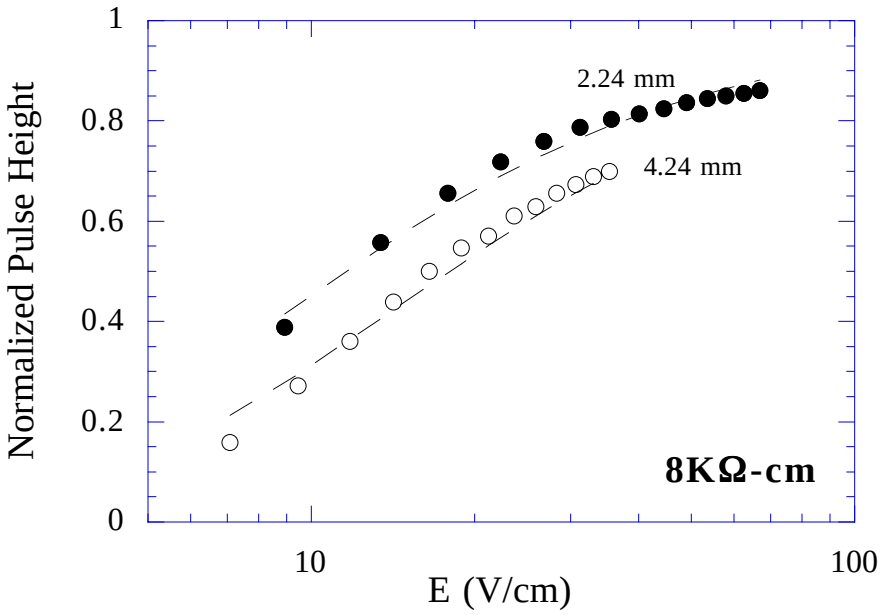

Figure 5.4.8 Pulse height data for 8 kΩ-cm samples in Mode 1 showing the fit to eqn. 5.19 (hybrid trapping model). The parameters of the fit are given in Table 5.2.

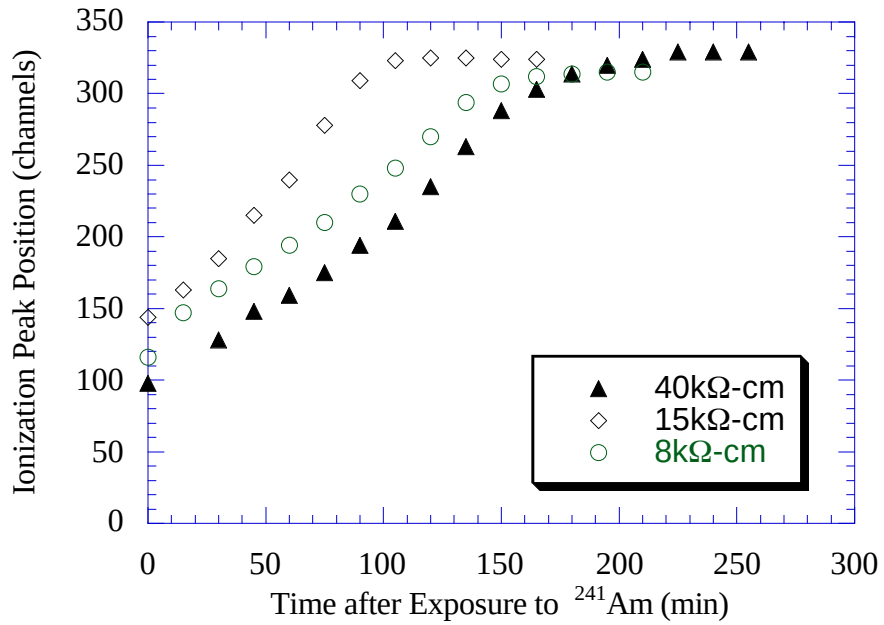

Figure 5.4.9 Mode shift time profiles. A shorter mode shift time at the same exposure rate to ionizing radiation indicates a lower density of minority impurities.

5.5 Remarks on the Charge Collection Experiments

Our results on charge collection at low temperature and low electric field indicate clearly that some amount, depending on crystal purity, of the charge loss at low electric field is occurring in the initial electron-hole plasma created by a particle interaction. We have presented a simple model of how this charge cloud may be behaving and satisfactory results were obtained. In addition we have seen that the simple trapping model is unsatisfactory. It failed to explain the thickness dependence of the data in both detector modes.

It is clear that a dark matter search will require a thick (~ 1 cm) very high-purity silicon wafer. Even at very high purity, however, the charge collection efficiency is adequate but not perfect at low electric field (E ~ 1 V/cm) because of the source effects we have described.

The model we have presented has not addressed the influence that surfaces may have on the formation and destruction of the electron-hole cloud. In our experiments the detectors were uniformly illuminated and a pulse height spectrum was measured which represents the distribution of pulse height versus event position. The experiments all gave the spectral peak, the dependence of which on electric field was what we were trying to explain, for events near the middle of the detector, far from the surfaces. Thus, the experiments presented here were not strongly influenced by the surfaces. Since expected background events in the dark matter search will be mostly near surface events we will wish to understand the charge collection physics for these events in order to see if there is any difference from events which occur deep in the crystal. A calibration source for near surface events is not particularly convenient. Low energy x-rays (< 10 keV) would serve this purpose but they will generate signals only slightly above the electronics noise. A better choice, but much more difficult to implement, would be ~ 50 keV electrons. Events from these electrons would be near surface (range ~ 10 μm) and could provide enough signal to conduct a comprehensive study of near surface effects. It is hoped that such experiments would shed more light on the charge loss processes operating in the initial electron-hole cloud.

Finally, although our data are in rough agreement with the simple prediction $\lambda(E) \sim E$ (by making the analogy $E \sim T_{electron}$ and using $\sigma \sim T^{-1}$ for low temperature from Ref. [31]) a more detailed understanding of how the trapping cross section depends on applied electric field is required. In particular, this simple dependence does not include the effect the applied field has on the attractive potential of the traps: the

superposition of the attractive potential and the applied potential gradient leads to a decrease in the geometrical radius of the trap [57]. A more detailed consideration of these effects will be discussed with reference to our data in a future paper [58].

CHAPTER 6: RECENT DEVELOPMENTS AND FUTURE PROSPECTS

In order to actually mount a dark matter search a detector which meets the operating capability criteria listed in section 1.4 must be constructed. It should be obvious at this point that one of these criteria, background suppression through the simultaneous measurement of phonons and ionization, has been demonstrated as a viable technique. In the last year rather amazing progress has been made in achieving the other detector capability requirements. In this chapter we will summarize these developments and describe the future prospects for the detector design.

6.1 Low-Impedance Electro-Thermal Feedback Phonon Sensors

Recently, K.D. Irwin, with our group, created the low-impedance electro-thermal feedback (ETF) phonon sensor which is based on thin W films [13, 21, 22]. This sensor operates on a different principle from the TES sensor described in chapter 3. The TES consists of many thin lines of metal connected in series to make an overall high-impedance device. The film is dc current biased to read out the changes in resistance. This arrangement is unstable to large changes in resistance since the Joule heating in the film is given by $P = I^2R$. The bias current must be kept below the so called latching current defined by the current which causes resistance pulses to grow with time due to the I^2R heating.

In contrast, the ETF sensor contains many lines connected in parallel to make a low-impedance device. In addition, instead of temperature biasing the thin metal film at the bottom of its superconductor-normal metal transition (as with the Ti TES), the ETF phonon sensor is biased in the middle of its transition. Rather than a current bias, the ETF sensor is voltage biased and a dc power is dissipated $P = V^2/R$ where R is the dc resistance of the sensor at the middle of its transition. This situation is stable since an increase in resistance leads to a decrease in the power dissipation; so the ETF is self-regulating. The strength of the self-regulation is characterized by a unitless parameter $\alpha = (T / R)(dR / dT)$ which measures the sharpness of the resistive transition. The steady-state condition of the ETF sensor has the silicon substrate cooled to well below the W T_c. The voltage bias raises the temperature of the parallel lines in the ETF sensor to the middle of each line's transition (this minimizes the effect of T_c gradients across a silicon wafer). Each line then dissipates just enough power to maintain its position in the transition. The current through the parallel array is monitored with a SQUID amplifier.

Particle interactions in the silicon substrate produce athermal phonons which are absorbed by the W film. This absorbed energy heats up the film thereby increasing its resistance. The energy can be reemitted to the substrate on a time scale τ_0 which is given by the Kapitsa boundary resistance between the film and the substrate (electron-phonon decoupling effects can dominate this resistance). However, the increase in resistance caused by a particle interaction leads to a decrease in the V^2/R power dissipated by the film. The absorbed energy can be removed from the film by a decrease in the Joule power on the time scale of $\sim n\tau_0 / \alpha$ where $n \approx 5$. W films with $\alpha > 1000$ have been made so the absorbed energy is removed quickly, before it can be reemitted to the substrate. The signal is read out as a change in the current flowing through the sensor. Since there is a constant voltage bias the total energy absorbed is given by the time integral of $V\Delta I$. This is an absolute measure of the energy absorbed with no free parameters when the energy lost back to the substrate is negligible.

Detectors of this type have been operated with amazing results. Thin Al films are also used to collect the phonon energy over large areas and funnel it into the W lines. These detectors have no intrinsic threshold, since an infinitesimal change in temperature of the sensor gives an infinitesimal change in resistance, but there are electronics noise limits. A resolution of ~ 400 eV FWHM at 6 keV has been demonstrated with a threshold of ~ 100 eV which includes the loss of sub-gap phonons in the Al which are radiated back to the Si substrate. The theoretical limits to the resolution are even better. A FWHM of 20 eV was achieved with calibration heat pulses which were introduced into the sensor itself by a pulse generator.

The electro-thermal feedback phonon sensor thus satisfies the detector criteria for a dark matter search. It easily achieves both threshold and resolution better than 1 keV for low energy events. This technology also has other applications. For example, high resolution x-ray spectroscopy and infra-red radiation detection.

6.2 SQUID-Array Instrumentation and Amptek A250 Charge Amplifier

Another recent development that has made the ETF sensor feasible is the availability of dc SQUID array instrumentation. A conventional SQUID readout is a very sensitive detector of current changes in its input coil. However, the typical output voltages are quite small (~ μV). Complicated and expensive electronics are required to read out these small voltages. Typically a lock-in technique is used and the system bandwidth is limited to ~ 30 kHz. For our detector systems which have a fast response

(~ μs) these systems are too slow. They are also too expensive to use in a many-channel dark matter search.

A collaboration between NIST and HYPRES has recently fabricated dc SQUID arrays [59]. In these devices the SQUID input coil is shared equally by a series connection of 200 dc SQUIDs . If the SQUIDs all operate in phase (a condition which can be achieved with care) then the output voltage is 200 times larger and low-cost room temperature electronics can be used to read out the signal. The arrays have a bandwidth of > 1 MHz, are small (0.2" x 0.2 " chip), and are easy to mount at the 1 K stage of a cryostat. The design of the arrays is being improved with the aid of our group (C. Fertig and S. Nam who have been performing noise measurements that have influenced the design changes). The best noise performance seen so far is ≤ 2 pA/√Hz current noise with 0.25 μH input inductance. The arrays are operated in a feedback mode for linearity and to increase the dynamic range but with some decrease of the bandwidth.

Another recent improvement in the detector instrumentation is the use of an Amptek A250 charge-sensitive pre-amplifier to read out the ionization signal. This amplifier, which was tested and installed by R. Clarke, uses a Si JFET (mounted in the cryostat and heated to ~ 120 K) as the front end. This JFET is connected to a room-temperature amplifier which provides feedback to set the gain. The noise performance is substantially better than that of the GaAs based pre-amplifiers. The electronics noise contribution to the energy resolution in the ionization pulse height spectra have been improved from ≈ 2 keV to ≈ 600 eV FWHM at 25 keV (equivalent noise charge ~ 200 e^-). For feedback stability the bandwidth must be reduced compared to the open-loop amplifier design. The ionization pulse risetime is now as slow as ~ 1 μs. However, the feedback eliminates the gain changes due to slow temperature drifts of the JFET or possible capacitance changes at the input of the pre-amplifier.

6.3 1 kg Scale Detector Design

The dark matter search requires ~ 1 kg of detector mass in order to have a reasonable event rate. The design of a detector of this mass scale is now in hand and the fabrication is beginning. The detector will consist of 6 1 cm thick wafers (4 Si and 2 Ge) to give a total mass of ~ 900 g arranged in a holder as shown in figure 6.3.1. One surface of each of the wafers will be instrumented with four W/Al QET (Quasi-particle trap assisted Electrothermal feedback Transition edge) sensors. By examining the partitioning of energy among the four phonon sensors it is expected that event position in the plane of the wafer will be measured to within ~ 1 mm. On the opposite face there will be two

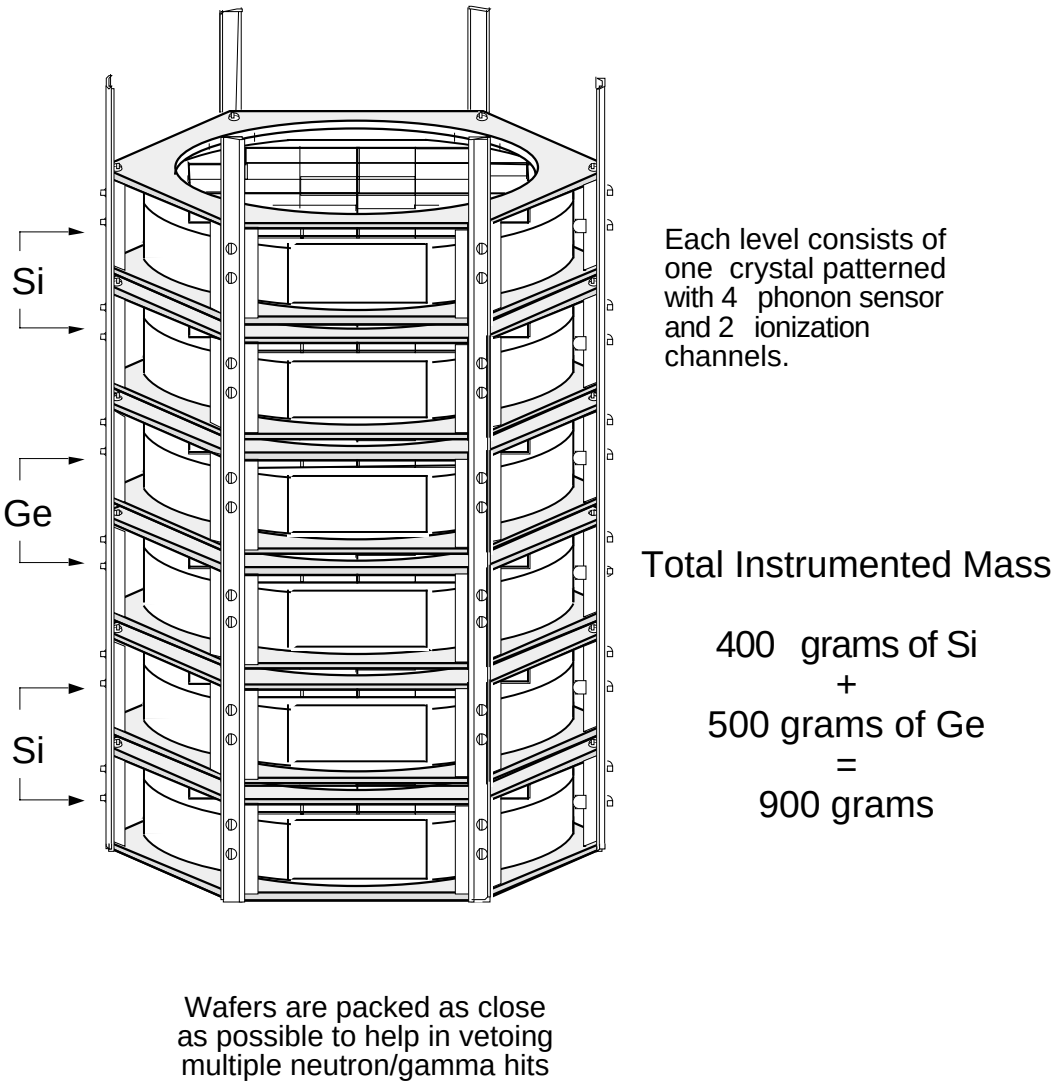

Figure 6.3.1 Diagram of the 1 kg mass scale detector. The tower consists of six 1 cm thick wafers (4 Si and 2 Ge). Drawing by Barron D. Chugg.

electrodes for making the ionization measurement. Timing differences between ionization and phonon signals will measure event position in the direction perpendicular to the plane of the wafer.

Considerable effort is involved in the thin film processing on such thick wafers. All of the equipment at the Center for Integrated Systems at Stanford which is used to fabricate the detectors had to be modified to accept the thick substrates. This done, our group (B.D. Chugg, B.A. Young, R.M. Clarke, and P.L. Brink) is now verifying that the

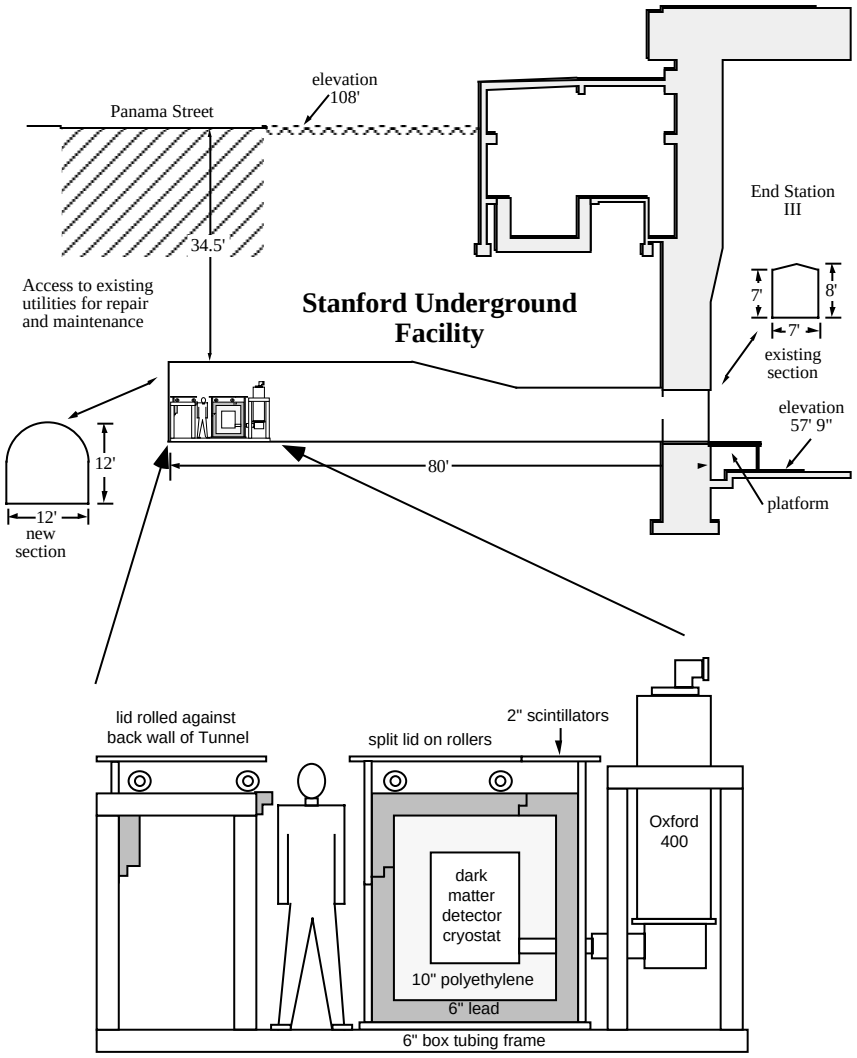

Figure 6.4.1 A cross-sectional view of the Stanford Underground Facility.

fabrication will actually work on the 1 cm thick wafers. It is expected that the 900 g detector will be ready to run within 1 year.

6.4 Low Background Facility

The CDMS (Cryogenic Dark Matter Search) experiment will be conducted in the Stanford Underground Facility (SUF). This laboratory is an extension of an unused beam-dump in HEPL End-station III. A cross section view is given in figure 6.4.1. The facility provides a soil overburden for cosmic ray shielding of ~ 20 MWE (meters water-

equivalent) which effectively cuts out the hadronic component of the cosmic rays. Muons do penetrate to the laboratory and an active muon veto consisting of plastic scintillators surrounding the detector shield has been constructed. Within the muon veto a lead and copper shield isolates the detector from the laboratory background radioactivity. In addition, the shield contains polyethylene for neutron moderation. This highly hydrogenous material is an effective moderator since a neutron will most efficiently lose its energy by elastically scattering from equal-mass particles, in this case protons.

A modified Oxford 400 dilution refrigerator is used to cool the detector to ~ 20 mK. The cryostat itself is located outside the lead shield and a system of dog-legs is used to bring the cold stages into the experimental space. This cryostat system, which was designed and built at the Lawrence Berkeley Laboratory and U.C. Berkeley, was recently moved to the SUF and reassembled. It has achieved its no power load base temperature of ~ 5 mK. Detector operation should begin in the near future.

CHAPTER 7: CONCLUSIONS

We have shown that there is evidence which suggests that the majority (> 90%) of the mass in the universe is dark. Weakly Interacting Massive Particles (WIMPs) are a particularly well motivated class of candidate dark matter particles. A dark matter search experiment would provide a very low signal event rate (~ 1 nuclear-recoil event kg^{-1} day^{-1}) and one of the main challenges of the experiment would be the reduction of contaminating background events (mostly electron-recoils) due to radioactivity in the laboratory or the detector itself. One attractive background rejection technique is the discrimination of nuclear-recoils (signal) from electron-recoils (backgrounds) based on the simultaneous measurement of both phonons and ionization. A nuclear-recoil event partitions more of its energy into phonons, and less into ionization, than does an equal energy electron-recoil event.

We have demonstrated the simultaneous measurement of phonons and ionization in a cryogenic Si detector using a Ti TES as the phonon sensor. The resolution on the ionization signal (which is not electronics limited) is 4 keV FWHM at 60 keV. The detector is position sensitive in two dimensions: the depth of an event is measured by phonon pulse length, and the position along the sensor, parallel to the surface, is found by deconvolving the crosstalk between the two amplifier channels. The position sensitivity allows us to make fiducial volume cuts to exclude near surface and edge events where either charge collection or the phonon measurement is incomplete. We find a nuclear-recoil/electron-recoil discrimination ratio > 1000:1 for large phonon pulse heights.

We have demonstrated the background rejection capability required for a dark matter search with a position sensitive cryogenic silicon detector. In addition, we have found that charge loss at low applied electric field in high purity silicon detectors can be understood in terms of diffuse propagation of charges with trapping in a field-free shielded charge cloud near the event location followed by electric field induced drift to the surfaces which may or may not, depending on purity, further attenuate the charge signal. The diameter of this charge cloud can be as large as 1 mm in the highest purity samples.

By instrumenting several phonon sensors on one Si substrate it is straightforward to determine event location in three dimensions. We plan to combine the charge measurement and background suppression technique with recently developed, more sensitive phonon detectors based on tungsten (W) thin films. The W sensors are capable of fully reconstructing event location while measuring the total energy deposition in

phonons. These devices will be used in a low background facility for WIMP dark matter searches and neutrino physics experiments.

APPENDIX: COMPUTER CODES FOR DATA ACQUISITION AND ANALYSIS

This appendix contains some of the Microsoft QuickBASIC version 1.00E routines used for data acquisition and analysis. These sample programs are intended to give some detail about the data acquisition and analysis process but it must be kept in mind that a variety of parameters must be changed to suit a particular data set and combination of experimental conditions.

A: Storing traces for simultaneous phonons and ionization

Program Title: Take P&Q v4
This program stores simultaneous traces from the oscilloscope and performs some preliminary analysis of the pulses.

```
LIBRARY "QuickBASIC4882.lib" : i1%=0:i2%=0:i3&=0:CALL IBINIT(i1%,i2%,i3&)

TEXTSIZE 9 : DEFDBL D,P,t,c,e,a,s,Q : DIM HQ(200)
RD$ = SPACE$(1078) : spr% = 0

PRINT " param file"; Fp$ : Fp$ = FILES$(0) : OPEN Fp$ FOR OUTPUT AS #1
PRINT "  trace file"; Ft$  : Ft$ = FILES$(0) : OPEN Ft$ FOR OUTPUT AS #2
CLOSE #2 : OPEN Ft$ AS #2 LEN = 2056 : Nevt = LOF(2)/2056
FIELD #2, 1024 AS Pdata$, 1024 AS Qdata$, 8 AS sec$

device1$ = "dev8" : D1% = 0 : CALL IBFIND (device1$, D1%):'  Initialize and set scope settings
WRT$="FRO 0, VER A, CPL AC, ATT 20E-3"+CHR$(10)
CALL IBWRT (D1%,WRT$)
WRT$="FRO 0, VER B, CPL AC, ATT 5E-3"+CHR$(10)
CALL IBWRT (D1%,WRT$)
WRT$="FRO 0, HOR MTB, TIM 5E-06, MOD SNG"+CHR$(10)
CALL IBWRT (D1%,WRT$)
WRT$="REG 0, MSC TRACE, INTF IEEE488.0, PRT REAL, REPEAT OFF, CNT 1"+CHR$(10)
CALL IBWRT (D1%,WRT$)

CLS : LINE(15,25)-(215,285),,B : LINE(15,225)-(215,225):'              Set up screen output
FOR n=0 TO 2   : LINE(15+100*n,285)-(15+100*n,290) : NEXT
FOR n=1 TO 19 : LINE(15+10*n,285)-(15+10*n,287)    : NEXT
FOR n=0 TO 2   : LINE(15,25+100*n)-(10,25+100*n)    : NEXT
FOR n=0 TO 26 : LINE(15,25+10*n)-(13,25+10*n)       : NEXT

trigger:
WHILE INKEY$<>CHR$(13) AND Nevt<1000
   CALL IBTRG (D1%) : CALL IBWAIT (D1%,&H4800):'              wait for scope trigger
   CALL IBRSP (D1%,spr%) : IF spr%<>64 THEN GOTO trigger
   Ntrig = Ntrig +1

   WRT$="REG 0, MSC TRACE, INTF IEEE488.0, DATA_TYPE BINARY, BGN 0, END 4095,
CHANNEL A, DAT ?"+CHR$(10):'           read scope channel A
   CALL IBWRT (D1%,WRT$)
   CALL IBRD (D1%,RD$) : FOR n=1 TO 500 : NEXT : P$ = MID$(RD$,11,1024)
```

```
   IF CVI(MID$(P$,241,2))>500 THEN BEEP:GOTO trigger
   GOSUB GetP :'            do priliminary analysis on phonon trace

   WRT$="REG 0, MSC TRACE, INTF IEEE488.0, DATA_TYPE BINARY, BGN 0, END 4095,
CHANNEL B, DAT ?"+CHR$(10):'            read scope channel B
   CALL IBWRT (D1%,WRT$)
   CALL IBRD (D1%,RD$) : FOR n=1 TO 500 : NEXT : Q$ = MID$(RD$,11,1024)
'  IF CVI(MID$(Q$,401,2))>100 THEN GOTO trigger
'  IF CVI(MID$(Q$,241,2))>100 THEN GOTO trigger
'  IF CVI(MID$(Q$,241,2))<-500 THEN GOTO trigger
   GOSUB GetQ:'            do preliminary analysis on charge trace

   Nevt=Nevt+1
   GOSUB plotstuff:'                                                    do screen output
   WRITE #1, Hour$, PHQ, PHP, PLP, CTF, sQ, sP, chi2/(Nfit-2):'       store paramaters  in paramater  file
   LSET Pdata$=P$ : LSET Qdata$=Q$ : LSET sec$=Hour$ : PUT #2, Nevt:' store traces in trace file
WEND

PRINT Ntrig "triggers":'                                    set instruments to local mode at end of data set
WRT$="FRO 0, HOR MTB, MOD REC"+CHR$(10)
CALL IBWRT (D1%,WRT$)
CALL IBLOC (D1%) : CALL IBSIC (D1%)
CLOSE : BEEP : WHILE INKEY$<>CHR$(13):WEND
END

GetP:'                                          preliminary analysis of phonon trace
   y1=0 : y2=0 : Nbase = 80 : NP0 = 0
   FOR n=1 TO Nbase : y=CVI(MID$(P$,2*n+1,2)) : y1=y1+y : y2=y2+y*y : NEXT
   Pbase=y1/Nbase : sP=SQR(y2/Nbase-Pbase*Pbase)
   WHILE NP0=0 AND n<200
      Pn = CVI(MID$(P$,2*n+1,2)) - Pbase   :   n=n+1 : IF Pn>3*sP THEN NP0=n
   WEND
'  IF NP0=0 GOTO trigger
   n = 80 : NL0 = 0 : PLP = 0 : PHP = 0 : thresh = 10
   WHILE PLP=0 AND n<400
      Pn = CVI(MID$(P$,2*n+1,2)) - Pbase   :   n=n+1
      IF NL0 =  0 AND Pn>thresh THEN NL0=n
      IF NL0 <> 0 AND Pn<thresh THEN PLP=n-NL0
      IF NL0 <> 0 AND Pn>PHP     THEN PHP=Pn
   WEND
'  IF PLP<=3 THEN GOTO trigger
RETURN

GetQ:'                                          preliminary analysis of charge trace
   y1=0 : y2=0 : chi2=0 : NQ0=0
   FOR n=1 TO Nbase : y=CVI(MID$(Q$,2*n+1,2)) : y1=y1+y : y2=y2+y*y : NEXT
   Qbase = y1/Nbase   :   sQ = SQR(y2/Nbase-Qbase*Qbase)
   WHILE NQ0=0 AND n<150
      Qn = CVI(MID$(Q$,2*n+1,2)) - Qbase   :   n=n+1 : IF Qn>4*sQ THEN NQ0=n
   WEND

   ee=0 : Qe=0 : Pe=0 : QP=0 : PP=0 : Ntau=360 : Nofs=4 : Nfit=300:'  find crosstalk fraction
   FOR n = NQ0+Nofs TO NQ0+Nofs+Nfit
      Qn = CVI(MID$(Q$,2*n+1,2)) - Qbase
      Pn = CVI(MID$(P$,2*n+1,2)) - Pbase
      en = EXP(-(n-NQ0)/Ntau) : ee = ee + en*en
      Qe = Qe + Qn*en   :   QP = QP + Qn*Pn
      Pe = Pe + Pn*en   :   PP = PP + Pn*Pn
```

```
   NEXT
   D = (Pe*Pe-ee*PP)  :  CTF = (QP*ee-Qe*Pe)/D  :  PHQ = (QP*Pe-Qe*PP)/D
   IF PHQ<40 THEN GOTO trigger   'look at 60's only
   FOR n = NQ0+Nofs TO NQ0+Nofs+Nfit
      Qn = CVI(MID$(Q$,2*n+1,2)) - Qbase
      Qfit = PHQ*EXP(-(n-NQ0)/Ntau)
      Pfit = CTF*(CVI(MID$(P$,2*n+1,2))-Pbase)
      chi2 = chi2 + (Qfit-Pfit-Qn)*(Qfit-Pfit-Qn)/(sQ*sQ)
   NEXT
RETURN

plotstuff:'                                    screen output
Hour$ = TIME$ : LOCATE 1,1
PRINT " File = "; Fp$, DATE$, Hour$," Event#"Nevt : LOCATE 2,1
PRINT USING " PHQ=###    PHP=###    PLP=###   CTF=##.##
chi2/DoF=##.###";PHQ,PHP,PLP,CTF,chi2/(Nfit-2)
'PRINT USING " Qbase=+###.## ±#.##   Pbase=+###.## ±#.##"; Qbase,sQ,Pbase,sP
iQ=INT(PHQ/2) : iP=INT(PHP/4) : iL=INT(PLP/4)
IF iQ>0 AND iQ<200 AND iP>=0 AND iP<200 AND iL>=0 AND iL<60 THEN
   PSET(15+iP,285-iL) :PSET(15+iP,225-iQ)
   HQ(iQ)=HQ(iQ)+1 : PSET(215+HQ(iQ),225-iQ)
END IF
RETURN
```

B: Analysis of simultaneous phonon and ionization traces

Program Title: Analyze traces PQ

This program performs a detailed analysis of the trace data taken with the program in A.

```
TEXTSIZE 9 : DEFDBL E,P,Q,x,Sx,Sy,Sxx,Sxy,XX:'                    open file to analyze
PRINT "  traces" : Ft$ = FILES$(1)  : OPEN Ft$ FOR INPUT AS #1 : CLOSE #1
OPEN Ft$ AS #1 LEN = 2056 : FIELD #1, 1024 AS P$, 1024 AS Q$, 8 AS T$
DIM VinQ(512), VmidQ(512), VoutQ(512)
ON ERROR GOTO fixer

GOSUB frames
FOR Ne=1 TO 1000
endfix:
 GET #1, Ne : GOSUB FilterQ :GOSUB Q: GOSUB IO : NEXT
CLOSE : BEEP : WHILE INKEY$<>CHR$(13) : WEND : END

frames:'                                ser up for screen output
CLS : LINE(10,50)-(410,250),,b
LINE(210,50)-(210,250)
FOR n=1 TO 9
   LINE(10+20*n,  50)-(10+20*n,  52)
   LINE(10+20*n,248)-(10+20*n,250)
   LINE(10,50+20*n)-(12,50+20*n)
   LINE(208,50+20*n)-(210,50+20*n)
   LINE(210+20*n,  50)-(210+20*n,  52)
   LINE(210+20*n,248)-(210+20*n,250)
   LINE(210,50+20*n)-(212,50+20*n)
   LINE(408,50+20*n)-(410,50+20*n)
NEXT
RETURN
```

```
P:'                                              analysis of phonon trace
   P1 = 0 : P2 = 0 : Nb = 80 : Ph = 0 : Pl = 0
   FOR n=1 TO Nb : P=CVI(MID$(P$,2*n+1,2)) : P1=P1+P : P2=P2+P*P : NEXT
   Pb = P1/Nb : Ps = SQR(P2/Nb-Pb*Pb)
  ' FOR n=Ni TO Ni+Nh-1 : P = P+CVI(MID$(P$,2*n+1,2)) : NEXT : n=n-1
   n=Ni-20 : PCR=0: NCR=0 : NCRflag=0 : PCRflag = 0 :threshu=4*Ps:threshd=0
   WHILE NCRflag=0 AND n<500
      P = CVI(MID$(P$,2*n+1,2)) - Pb
      IF PCRflag = 0 AND P>threshu THEN PCR = n: PCRflag = 1
      IF PCRflag = 1 AND Ph<P THEN Ph = P
      IF PCRflag = 1 AND P<threshd THEN NCR = n: NCRflag = 1
      n = n+1
   WEND
   Pl=NCR-PCR
RETURN

FilterQ:'          correct for ac coupling of amplifier
   tau=.01: dt=.0000001:integral=0:integral2=0
   Q1 = 0 : Q2 = 0 : Nb = 80 : Qh = 0
   FOR n=1 TO Nb : Q=CVI(MID$(Q$,2*n+1,2)) : Q1=Q1+Q : Q2=Q2+Q*Q : NEXT
   Qb = Q1/Nb : Qs = SQR(Q2/Nb-Qb*Qb)
   FOR n=1 TO 511
      VoutQ(n)=CVI(MID$(Q$,2*n+1,2))-Qb
   NEXT
   FOR n=1 TO 511
      integral=integral+(dt/tau)*VoutQ(n)
      VmidQ(n)=integral+VoutQ(n)
      integral2=integral2+(dt/tau)*VmidQ(n)
      VinQ(n)=integral+VmidQ(n)
   NEXT
RETURN

Q:'                              analysis of charge pulse
   Q1 = 0 : Q2 = 0 : XX = 0 : Ni=0 : Nb=80
   FOR n = Nb TO 120
      IF Ni=0 AND VinQ(n) > 4*Qs THEN Ni=n
   NEXT
   GOSUB P
    Nt=360
    Sx=0: Sy=0:Sxx=0:XX=0:Fs=Ni+Pl:Y=0:T=0
   FOR n=Fs TO 511
      Y=Y+(VinQ(n))*EXP(-(n-Ni)/Nt)
      T=T+EXP(-2*(n-Ni)/Nt)
   NEXT
   Qh=Y/T
   FOR n=Fs TO 511
      XX=XX+(VinQ(n)-Qh*EXP(-(n-Ni)/Nt))^2/(Qs*Qs)
   NEXT
   del = 0
   GOSUB delta
RETURN

delta:'                          correct for shaping of ionization network
  fall=(1-EXP(-1/Nt))
  scale=fall/(1+Pl*fall)
  sum=0
  FOR n=0 TO (Pl-1)
```

```
    sum=sum+EXP(n/Nt)*(VinQ(n+Ni)-(Qh*EXP(-n/Nt)))
  NEXT
  del=scale*sum
RETURN


IO: '                          screen output
'CLS
LOCATE 1,50 : PRINT "   Event#"Ne
'LOCATE 1,1 : PRINT "   File = "; Ft$, T$," Event#"Ne
LOCATE 2,50: PRINT USING "   Ph=###.##   Pl=###   Ni=###.#  Fs=###";Ph,Pl,Nt,Ni
LOCATE 3,50: PRINT USING "   Qh=###    MQh=###    XX/DoF=##.###";Qh,Qh+del,XX/(511-Fs-2)
LOCATE 4,50: PRINT USING "   Qb=+###.## ±#.##   Pb=+###.## ±#.##"; Qb,Qs,Pb,Ps
x1=INT(Ph/4)  : y1=INT(Qh+del) : y2=INT(Qh)
IF x1<0 OR x1>200 THEN GOTO skip
'IF x2<0 OR x2>200 THEN GOTO skip
IF y1<0 OR y1>200 OR y2<0 OR y2>200 THEN GOTO skip
    PSET(10+x1,250-y2) : PSET(210+x1,250-y1)
 '   IF x1<45 OR x1>50 OR y2<30 OR y2>40 THEN GOTO skip
 ' FOR n=70 TO 500
  '      PSET(20+(n-70),140-(CVI(MID$(P$,2*n+1,2))-Pb)/2)
  '      PSET(20+(n-70),140)
  '      PSET(20+(n-70),280-(CVI(MID$(Q$,2*n+1,2))-Qb)/2)
   '      IF n>Ni THEN PSET(20+(n-70),280-(Qh/2)*EXP((Ni-n)/Nt))
   ' NEXT
'WHILE INKEY$<>CHR$(13) :WEND
skip:
RETURN

fixer:
LOCATE 2,5: PRINT USING "Error on trace ###, ignoring trace"; Ne
Ne=Ne+1
RESUME endfix
```

C: Analysis of simultaneous charge traces

Program Title: Analyze traces Q&Q

This program performs a detailed analysis of two simultaneous charge pulses.

```
TEXTSIZE 9 : DEFDBL E,P,Q,x
PRINT " param file to create?"; Fp$ : Fp$ = FILES$(0) : OPEN Fp$ FOR OUTPUT AS #2
PRINT "  trace file to analyze" : Ft$ = FILES$(1)  : OPEN Ft$ FOR INPUT AS #1 : CLOSE #1
OPEN Ft$ AS #1 LEN = 2056 : FIELD #1, 1024 AS Q1$, 1024 AS Q2$, 8 AS T$
DIM H(200),C(200), VoutQ1(512),VinQ1(512),VmidQ1(512),VoutQ2(512),VmidQ2(512),VinQ2(512)

CLS
LINE (50,50)-(250,250),,b
FOR Ne=1 TO 1000
   GET #1, Ne
   flag=0
   GOSUB FilterQ1: GOSUB FilterQ2
   GOSUB trigger
   IF flag=1 THEN GOTO jump
   GOSUB charge1 : GOSUB charge2
   GOSUB IO
```

```
   jump:
NEXT

CLOSE #1 : CLOSE #2 : BEEP : WHILE INKEY$<>CHR$(13) : WEND : END

FilterQ1:'                    correct for ac coupling of amplifier
   tau=.01: dt=.0000001:integral1=0:integral2=0
   Q1 = 0 : Q2 = 0 : Nb = 50
   FOR n=1 TO Nb : Q=CVI(MID$(Q1$,2*n+1,2)) : Q1=Q1+Q : Q2=Q2+Q*Q : NEXT
   Q1b = Q1/Nb : Q1s = SQR(Q2/Nb-Q1b*Q1b)
   FOR n=1 TO 511
      VoutQ1(n)=CVI(MID$(Q1$,2*n+1,2))-Q1b
   NEXT
   FOR n=1 TO 511
      integral1=integral1+(dt/tau)*VoutQ1(n)
      VmidQ1(n)=integral1+VoutQ1(n)
      integral2=integral2+(dt/tau)*VmidQ1(n)
      VinQ1(n)=integral2+VmidQ1(n)
   NEXT
RETURN

FilterQ2:'                    correct for ac coupling of amplifier
   tau=.01: dt=.0000001:integral1=0:integral2=0
   Q1 = 0 : Q2 = 0 : Nb = 50
   FOR n=1 TO Nb : Q=CVI(MID$(Q2$,2*n+1,2)) : Q1=Q1+Q : Q2=Q2+Q*Q : NEXT
   Q2b = Q1/Nb : Q2s = SQR(Q2/Nb-Q2b*Q2b)
   FOR n=1 TO 511
      VoutQ2(n)=CVI(MID$(Q2$,2*n+1,2))-Q2b
   NEXT
   FOR n=1 TO 511
      integral1=integral1+(dt/tau)*VoutQ2(n)
      VmidQ2(n)=integral1+VoutQ2(n)
      integral2=integral2+(dt/tau)*VmidQ2(n)
      VinQ2(n)=integral2+VmidQ2(n)
   NEXT
RETURN

trigger:'                     find which trace gave the trigger
   Ni=0
   FOR n = Nb TO 150
      IF Ni=0 AND ABS(VinQ1(n)) > 4*Q1s THEN Ni=n
      IF Ni=0 AND ABS(VinQ2(n)) > 4*Q2s THEN Ni=n
   NEXT
   IF Ni=0 THEN flag=1
RETURN

charge1:'                           simple least quares fit to exponential to extract pulse height
   XX1 = 0 : Nb=50 : Nt=400
   Ysum=0 : Fitsum=0
   FOR n = Ni + 10 TO 500
      Ysum=Ysum + VinQ1(n)
      Fitsum=Fitsum + EXP(-(n-Ni)/Nt)
   NEXT
   Q1h=Ysum/Fitsum
   FOR n = Ni + 10 TO 500
      XX1=XX1 + ((VinQ1(n) - Q1h*EXP(-(n-Ni)/Nt))^2)/(Q1s*Q1s)
   NEXT
   XX1dof = XX1/(500-Ni-9)
```

```
RETURN

charge2:'                                simple least quares fit to exponential to extract pulse height
   XX2 = 0 : Nb=50 : Nt=400
   Ysum=0 : Fitsum=0
   FOR n = Ni + 10 TO 500
      Ysum=Ysum + VinQ2(n)
      Fitsum=Fitsum + EXP(-(n-Ni)/Nt)
   NEXT
   Q2h=Ysum/Fitsum
   FOR n = Ni + 10 TO 500
      XX2=XX2 + ((VinQ2(n) - Q2h*EXP(-(n-Ni)/Nt))^2)/(Q2s*Q2s)
   NEXT
   XX2dof = XX2/(500-Ni-9)
RETURN

IO:        '            screen output
'CLS
WRITE #2,Q1h,Q2h, XX1dof, XX2dof,Q1b,Q1s,Q2b,Q2s,Ni,Nt
LOCATE 1,1 : PRINT "   File = "; Ft$, T$," Event#"Ne
LOCATE 2,30: PRINT USING "   Q1=###.##   Q2=###.##  XX1=##.###  XX2=##.###";Q1h,Q2h,
XX1dof, XX2dof
LOCATE 3,30: PRINT USING "   Q1b=+###.## ±#.##   Q2b=+###.## ±#.##  Ni=###  Nt=###";
Q1b,Q1s,Q2b,Q2s,Ni,Nt
x=INT((Q1h+RND)*2) : y=INT((Q2h+RND)*2)
   PSET (50+x,250-y)
'FOR n=10 TO 500
'   PSET(10+n,100-VinQ1(n)/2)
'    PSET(10+n, 200-VinQ2(n)/2)
'    IF n > Ni+10 THEN
'       PSET(10+n, 100-Q1h*EXP(-(n-Ni)/Nt)/2)
'       PSET(10+n, 200-Q2h*EXP(-(n-Ni)/Nt)/2)
'    END IF
'NEXT

'WHILE INKEY$<>CHR$(13) :WEND
skip:
RETURN
```

D: Plotting results of analysis

Program Title: Plot params 300

This program plots the output of the analysis programs.

```
TEXTSIZE 12
DIM HY1(300),HY2(300),HX1(300),HX2(300),FILE$(100)
LOCATE 1,1 : INPUT " How many input files";NT
FOR NF=1 TO NT
   FILE$(NF)=FILES$(1)
NEXT
Ngood=0:n=0
LINE(10,40)-(910,340),,B: LINE(310,40)-(310,340):LINE(610,40)-(610,340)
FOR i = 0 TO 20
   LINE(10+15*i,40)-(10+15*i,43)
   LINE(10+15*i,337)-(10+15*i,340)
```

```
   LINE(310+15*i,40)-(310+15*i,43)
   LINE(310+15*i,337)-(310+15*i,340)
   LINE(610+15*i,40)-(610+15*i,43)
   LINE(610+15*i,337)-(610+15*i,340)

   LINE(10,40+15*i)-(13,40+15*i)
   LINE(307,40+15*i)-(313,40+15*i)
   LINE(607,40+15*i)-(613,40+15*i)
   LINE(907,40+15*i)-(910,40+15*i)
NEXT
   LINE(160,40)-(160,46): LINE(460,40)-(460,46)
   LINE(760,40)-(760,46)
   LINE(160,434)-(160,440): LINE(460,434)-(460,440)
   LINE(760,434)-(760,440)
   LINE(10,190)-(16,190)
   LINE(304,190)-(316,190):   LINE(604,190)-(616,190)

FOR NF=1 TO NT'                        read data from input file
   OPEN FILE$(NF) FOR INPUT AS #1
   LOCATE 1,1 : PRINT "       File = "FILE$(NF)
   WHILE NOT EOF(1)
      flag=0
      INPUT #1, PHQ, PHP, PLP, CTF, SQ, SP, chi2
      x1=INT(PHP*3/4) : x2=INT(300*CTF) : x3=INT((PLP+RND)*3) : y1=INT(PHQ*3/2)
      IF x1<0 OR x1>299 THEN flag=1
      IF x2<0 OR x2>299 THEN flag=1
      IF y1<0 OR y1>299 THEN flag=1
      IF y2<0 OR y2>299 THEN flag=1
      IF chi2 > 2 THEN flag=1
      'IF x1<6 THEN flag=1
      'IF x2<51 OR x2>125 THEN flag=1
      n=n+1
      IF flag = 0 THEN'                              plot data to screen
         Ngood = Ngood + 1
         PSET(10+x1,340-y1)          : PSET(310+x2,340-y1)
         PSET(610+x3,340-y1)
        'LOCATE 45,5 : PRINT "y1="y1", y2="y2",x1="x1", x2="x2", n="n
         HY1(y1)=HY1(y1)+1              : HX1(x1)=HX1(x1)+1
         HY2(y2)=HY2(y2)+1              : HX2(x2)=HX2(x2)+1
         LINE(910,340-y1)-(910+INT(HY1(y1)/10),340-y1)
         'LINE(410,240-y2)-(410+INT(HY2(y2)/10),240-y2)
         'LINE(10+x1,440)-(10+x1,440+INT(HX1(x1)/10))
         'LINE(210+x2,440)-(210+x2,440+INT(HX2(x2)/10))
      END IF
   WEND

   CLOSE #1
NEXT NF
LOCATE 2,1
PRINT "       No. events passing cuts = "Ngood",  out of "n"total
BEEP : WHILE INKEY$="" : WEND
END
```

E: Storing pulse height spectra

Program Title: Take TN spectra

This program reads and stores the 4096 channels of the Tracor Northern mult-channel analyzer.

```
'TRANSFER PHS FROM TRACOR NORTHERN TO MAC SE

LIBRARY "HD-80:NI-488.2:BASIC LI:QuickBASIC4882.lib"          'open the library (which should be in the System Folder).
ibsta%=0 : iberr%=0 : ibcnt&=0          'initialize the variables so the library can write to them.
CALL ibinit(ibsta%,iberr%,ibcnt&)    'tell the library what variables to write to.

'DIM Mem$(5)
'Mem$(1) = "M14": Mem$(2) = "M24": Mem$(3) = "M34": Mem$(4) = "M44"
Gexp = 1
TEXTSIZE 10

N$ = FILES$(0)
INPUT "Live time (sec) "; T
INPUT "Real time (sec) "; R
'INPUT "Memory Sector to Receive (1-4) "; S
CLS
PRINT "Filename: "; N$,

BDnames$ = "tracor"
BDinter$ = "gpib0"
BD% = 0
spr% = 0
'Cnt% = 14+1024    'number of bytes in each data string from Tracor
Cnt% = 14+4096   'number of bytes in each data string from Tracor
'RD$ = SPACE$(3*256+9)
'Cnt$ = SPACE$(3*256+9)
RD$ = SPACE$(3*4096+15)
Cnt$ = SPACE$(3*4096+15)

DIM Cnts(4096)

   'CALL IBFIND (BDinter$, BD%)
   'IF BD%<0 THEN PRINT "IBFIND error"
   CALL IBFIND (BDnames$, BD%)
   WRT$=" "+CHR$(13)
   CALL IBWRT (BD%,WRT$)
   CALL IBRSP (BD%,spr%):PRINT spr%
   CALL IBRD (BD%,RD$)
   PRINT ibcnt&;":";MID$(RD$,1,ibcnt&)
   CALL IBRD (BD%,RD$)
   PRINT ibcnt&;":";MID$(RD$,1,ibcnt&)
   CALL IBRD (BD%,RD$)
   PRINT ibcnt&;":";MID$(RD$,1,ibcnt&)
   WRT$="M11;HO "+CHR$(13)
   CALL IBWRT (BD%,WRT$)
   WHILE spr%>29: CALL IBRSP (BD%,spr%): WEND
   CALL IBRD (BD%,RD$)
   PRINT "Count:";ibcnt&
```

```
   WHILE spr%>29: CALL IBRSP (BD%,spr%): WEND
   Cnt$ = RD$
   CALL IBLOC (BD%)
   CALL IBRD (BD%,RD$)
   PRINT MID$(RD$,1,ibcnt&)
   CALL IBRD (BD%,RD$)
   PRINT MID$(RD$,1,ibcnt&)
   CALL IBSIC (BD%)


    FOR N = 0 TO 4095
      Cnts(N) = CVI(MID$(Cnt$,15+3*N,1)+MID$(Cnt$,14+3*N,1))
      'PRINT USING " #####"; Cnts(N);
      'IF (N MOD 8) = 7 THEN PRINT " "
      IF CntsMax<Cnts(N) THEN CntsMax=Cnts(N): ChanMax = N
      Sum = Sum + Cnts(N)
   NEXT N

      CLS
      PRINT "Filename is "; N$; ";  Time(sec) ="; T
      PRINT "Total Cnts ="; Sum; ";   Peak ="; ChanMax; ";  No. in Peak ="; CntsMax
      IF Gexp<>1 THEN PRINT "Horizontal Expansion ="; Gexp

      LINE(94,256)-(106+Gexp*256,44),,B
      FOR K = 0 TO 10
         LINE(94,250-K*20)-(96,250-K*20)
         LINE(106+Gexp*256,250-K*20)-(104+Gexp*256,250-K*20)
      NEXT K
      FOR K = 0 TO 3
         LINE(94,250-K*100)-(98,250-K*100)
         LINE(106+Gexp*256,250-K*100)-(102+Gexp*256,250-K*100)
      NEXT K
      FOR K = 0 TO 5
         LINE(100+Gexp*K*50,256)-(100+Gexp*K*50,252)
         LINE(100+Gexp*K*50,44)-(100+Gexp*K*50,48)
      NEXT K
      FOR M = 0 TO 4095
         'CIRCLE(100+Gexp*M,250-200*(Cnts(M)/CntsMax)),1
        LINE(100+Gexp*M/16,250)-(100+Gexp*M/16,250-200*(Cnts(M)/CntsMax))
      NEXT M

StoreFile:
OPEN N$ FOR OUTPUT AS #1
   A% = T
   PRINT #1, A%
   A% = R
   PRINT #1, A%

FOR K=0 TO 4095
   A% = Cnts(K)
   PRINT #1,A%
NEXT K
CLOSE #1

BEEP:PRINT "done"
WHILE INKEY$<>CHR$(13):WEND

'LCOPY
```

```
'WHILE INKEY$<>CHR$(13):WEND
END
```

F: Viewing stored spectra

Program Title: View TN spectra

This program reads a stored TN data file and plots the data by quadrant.

```
TEXTSIZE 9:OPTION BASE 1:DEFLNG c,s:DIM c(4,1024):DIM cm(4):DIM ct(4)
indata:
CLS:PRINT" Name input file":f$=FILES$(1):OPEN f$ FOR INPUT AS #1
INPUT#1,tl:INPUT#1,tr
FOR n=1 TO 4:cm(n)=0:ct(n)=0:NEXT
FOR n=1 TO 4
   FOR m=1 TO 1024
      INPUT#1,c:c(n,m)=c:ct(n)=ct(n)+c
      IF cm(n)<c(n,m) THEN cm(n)=c(n,m)
   NEXT m
NEXT n
CLOSE
show:
INPUT" Which quadrant do you want to look at",n
PRINT" The vertical scale is",cm(n)
INPUT" Change this to what?",cm
CLS:PRINT" Filename ="f$"  ; quadrant "n"/4; Total counts ="ct(n):LINE(10,280)-(410,30),,b
LOCATE 2,1:PRINT cm
FOR i=1 TO 40:LINE(10+i*10,  30)-(10+i*10,  28):NEXT
FOR i=1 TO 40:LINE(10+i*10,280)-(10+i*10,282):NEXT
FOR i=0 TO 4:LINE(10+i*100,  30)-(10+i*100,24):NEXT
FOR i=0 TO 4:LINE(10+i*100,280)-(10+i*100,286):NEXT
FOR m=1 TO 400:LINE(10+m,280)-(10+m,280-250*c(n,m)/cm):NEXT:BEEP
FOR i=1 TO 50:LINE(  10,280-5*i)-(    8,280-5*i):NEXT
FOR i=1 TO 50:LINE(410,280-5*i)-(412,280-5*i):NEXT
FOR i=0 TO 10:LINE(  10,280-25*i)-(    5,280-25*i):NEXT
FOR i=0 TO 10:LINE(410,280-25*i)-(415,280-25*i):NEXT

WHILE INKEY$="":WEND
GOTO show
END
```

REFERENCES

1. See, for example, Proceedings of the Fifth International Workshop on Low-Temperature Detectors. Held: Berkeley, CA, USA, 29 July - 3 Aug. 1993. *J. Low Temp. Physics* 93, nos. 3/4 (1993).

2. J.R. Primack, D. Seckel, and B. Sadoulet, *Ann. Rev. Nucl. Part. Sci*. **38**, 751 (1988).

3. A.H. Guth, *Phys. Rev.* ***D*** **23**, 347 (1981).

4. L. Moscoso and M. Spiro, *Nuclear Physics B (Proc. Suppl.)* **28A**, 267 (1992).

5. V.C. Rubin, *Science* **220**, 1339 (1983).

6. M.C. Kutner, Astronomy: A Physical Perspective, chapter 5, John Wiley & Sons, New York, 1987.

7. M.S. Turner, in Trends in Astroparticle Physics, eds. D. Cline and R. Peccei, World Scientific Ltd., 1992.

8. D.N. Schramm and R.V. Wagoner, *Ann. Rev. Nucl. Sci*. **27**, 37 (1977).

9. T.P. Walker, G. Steigman, D.N. Schramm, K.A. Olive, and H. Kang, *Astrophysical Journal* **376**, 51 (1991).

10. See the Physics Update section in *Physics Today* (June 1995).

11. B.L. Dougherty, in Particle and Nuclear Astrophysics and Cosmology in the Next Millenium, Proceedings of Snowmass '94, eds. R. Peccei and E. Kolb, World Scientific.

12. P.D. Barnes, Jr., *et al.*, Proceedings of the Fifth International Workshop on Low-Temperature Detectors. Held: Berkeley, CA, USA, 29 July - 3 Aug. 1993. *J. Low Temp. Physics* 93, 791 (1993).

13. K.D. Irwin, Ph.D. Thesis, Stanford University (1995), unpublished.

14. B.D. Chugg, K.D. Irwin, and B. Cabrera, Proceedings of the Fifth International Workshop on Low-Temperature Detectors. Held: Berkeley, CA, USA, 29 July - 3 Aug. 1993. *J. Low Temp. Physics* 93, 429 (1993).

15. M.J. Penn, B.L. Dougherty, B. Cabrera, and D.L. Sisson, *Nucl. Instrum. and Meth. A*, in press.

16. B. Neuhauser, *Rev. Sci. Instrum.*, in preparation.

17. A.T. Lee, *Rev. Sci. Instrum.* **64**, 2373 (1993).

18. A.T. Lee, *Rev. Sci. Instrum.* **60**, 3315 (1989).

19. A. van der Zeil, Noise in Solid State Devices and Circuits, John Wiley & Sons, New York, 1986.

20. M. LeGros, *et al.*, *Nucl. Instrum. and Meth.* **A345**, 492 (1994).

21. K.D. Irwin, *Appl. Phys. Lett.* **66**, 1998 (1995).

22. K.D. Irwin, *et al.*, *Rev. Sci. Instrum.* **66**, 1 (1995).

23. M.M. Lowry, D. Deptuck, and I.C. Girit, Proceedings of the Fifth International Workshop on Low-Temperature Detectors. Held: Berkeley, CA, USA, 29 July - 3 Aug. 1993. *J. Low Temp. Phys.* **93**, 239 (1993).

24. J. Menedez and M. Cardona, *Phys. Rev.* **B29**, 2051 (1984).

25. S. Tamura, *Phys. Rev.* **B31**, 2574 (1985).

26. A. Berke, A.P. Mayer, and R.K. Wehner, *J. Phys. C* **21**. 2305 (1988).

27. G.A. Northrop and J.P. Wolfe, *Phys. Rev.* **B22**, 6196 (1980).

28. B.A. Young, B. Cabrera, and A.T. Lee, *Phys. Rev. Lett.* **64**, 2795 (1990).

29. R.S. Muller and T.I. Kamins, Device Electronics for Integrated Circuits, 2nd ed., chapter 3, John Wiley & Sons, New York, 1986.

30. R.A. Smith, Semiconductors, 2nd. ed., sections 8.9 and 8.10, Cambridge University Press, London, 1978.

31. V.N. Abakumov, V.I. Perel, and I.N. Yassievich, *Sov. Phys. Semicond.* **12**, 1 (1978).

32. Assuming that the trapping cross sections are not too different in Ge, which is true for trapping on ionized impurities, then recent data in Ge are applicable. See T. Shutt, *et al., Phys. Rev. Lett.* **69**, 3531 (1992) and T. Shutt, Ph.D. Thesis, University of California, Berkeley (1993), unpublished.

33. B.A. Young, *et al., Nucl. Inst. and Meth.* **A311**, 195 (1992).

34. A.T. Lee, Ph.D. Thesis, Stanford University (1992), unpublished.

35. A.T. Lee, B. Cabrera, B.L. Dougherty, M.J. Penn, J.G. Pronko, and S. Tamura, in preparation, to be submitted to *Phys. Rev.* **B**.

36. B.L. Dougherty, *et al., Nucl. Inst. and Meth.* **A333**, 464 (1993).

37. S. Ramo, *Proc. IRE* **27**, 584 (1939).

38. M. Martini, J.W. Mayer, and K.R. Zanio, p. 181 - 261 in Applied Solid State Science, vol. 3, R. Wolfe ed., Academic Press, 1972.

39. For measurements of electron drift velocity in silicon using the transient charge technique see C. Canali, C. Jacoboni, F. Nava, G. Ottaviani, and A. Alberigi-Quantara, *Phys. Rev.* **B12**, 2265 (1975).

40. For measurements of hole drift velocity in silicon using the transient charge technique see G. Ottaviani, L. Reggiani, C. Canali, F. Nava, and A. Alberigi-Quantara, *Phys. Rev.* **B12**, 3318 (1975).

41. For measurements of hole drift velocity in germanium using the transient charge technique see L. Reggiani, C. Canali, F. Nava, and G. Ottaviani, *Phys. Rev.* **B16**, 2781 (1977).

42. For measurements of electron drift velocity and diffusivity in germanium using the transient charge technique see C. Jacoboni, F. Nava, C. Canali, and G. Ottaviani, *Phys. Rev.* **B24,** 1014 (1981).

43. T. Shutt, *et al*., *Phys. Rev. Lett.* **69**, 3425 (1992).

44. N.J.C. Spooner, *et al.*, *Phys. Lett.* **B273**, 333 (1991).

45. P.N. Luke, *J. Appl. Phys.* **64**, 6858 (1988).

46. B.L. Dougherty, *Phys. Rev.* **A45**, 2104 (1992).

47. L. Pages, *et al*., *Atomic Data* **4**, 1 (1972).

48. J.C. Ashley, *et al.*, *IEEE Trans. on Nucl. Sci*. **NS-23**, 1833 (1976).

49. G. Restelli, and A. Rota, in Semiconductor Detectors, G. Bertolini, A. Coche, eds., North-Holland, Amsterdam (1968).

50. E.M. Conwell, *Phys. Rev.* **135**, A1138 (1964).

51. F.F. Chen, Introduction to Plasma Physics and Controlled Fusion Vol.1, Plenum Press, New York and London (1984).

52. E.C. Finch, *et al.*, *Nucl. Instr. Meth.* **163**, 467 (1979).

53. I. Kanno, *Rev. Sci. Instrum.* **58**, 1926 (1987).

54. J.S. Blakemore, Semiconductor Statistics, Dover Publications, Inc., New York (1987).

55. B. Cabrera, personal communication.

56. S. Chandrasekhar, *Rev. Mod. Phys.* **15**, 1 (1943).

57. J. L. Hartke, *J. Appl. Phys.* **39**, 4871 (1968).

58. M.J. Penn, B.L. Dougherty, B. Cabrera, R.M. Clarke, in preparation.

59. R.P. Welty and J.M. Martinis, *IEEE Trans. Apll. Superc.* **3**, 2605 (1993), proceedings of the 1992 Applied Superconductivity conference.